

How to Constrain your M dwarf II:
the mass-luminosity-metallicity relation from $0.70M_{\odot}$ to $0.075M_{\odot}$

ANDREW W. MANN,^{1, 2,*} TRENT DUPUY,³ ADAM KRAUS,⁴ ERIC GAIDOS,⁵ MICHAEL IRELAND,⁶ MEGAN ANSDELL,^{7, 8}
AARON RIZZUTO,^{4, †} CHAO-LING HUNG,⁹ JASON DITTMANN,^{10, †} SAMUEL FACTOR,⁴ GREGORY FEIDEN,¹¹
RAQUEL A. MARTINEZ,⁴ AND DARY RUÍZ-RODRÍGUEZ^{12, 13}

¹Department of Physics and Astronomy, University of North Carolina at Chapel Hill, Chapel Hill, NC 27599-3255, USA

²Columbia University, Department of Astronomy, 550 West 120th Street, New York, NY 10027

³Gemini Observatory, Northern Operations Center, 670 N. Aohoku Place, Hilo, HI 96720, USA

⁴Department of Astronomy, The University of Texas at Austin, Austin, TX 78712, USA

⁵Department of Geology & Geophysics, University of Hawaii at Mānoa, Honolulu, Hawaii 96822 USA

⁶Research School of Astronomy & Astrophysics, Australian National University, Canberra ACT 2611, Australia

⁷Center for Integrative Planetary Science, Berkeley, CA 94720, USA

⁸Department of Astronomy, University of California at Berkeley, Berkeley, CA 94720, USA

⁹Department of Physics, Manhattan College, 4513 Manhattan College Parkway, Riverdale, NY 10471, USA

¹⁰Massachusetts Institute of Technology, 77 Massachusetts Avenue, Cambridge, Massachusetts 02138, USA

¹¹Department of Physics, University of North Georgia, Dahlonega, GA 30597, USA

¹²Chester F. Carlson Center for Imaging Science, School of Physics & Astronomy, and Laboratory for Multiwavelength Astrophysics, Rochester Institute of Technology, 54 Lomb Memorial Drive, Rochester NY 14623 USA

¹³Research School of Astronomy and Astrophysics, Australian National University, Canberra, ACT 2611, Australia

Submitted to The Astrophysical Journal

ABSTRACT

The mass-luminosity relation for late-type stars has long been a critical tool for estimating stellar masses. However, there is growing need for both a higher-precision relation and a better understanding of systematics effects (e.g., metallicity). Here we present an empirical relationship between M_{K_S} – M_* and M_* spanning $0.70M_{\odot}$ to $0.075M_{\odot}$. The relation is derived from 59 nearby binaries, whose orbits we determine using a combination of Keck/NIRC2 imaging, archival adaptive optics data, and literature astrometry. From their orbital parameters, we determine the total mass of each system, with precision better than 1% in the best cases (median precision on M_{tot} of 5.6%). We use these binaries and resolved Ks magnitudes to calibrate the M_{K_S} – M_* within a Monte Carlo Markov Chain framework. The resulting posteriors can be used to determine masses of single stars to 2–3%. The limit to this precision is scatter around the best-fit relation beyond measured M_* uncertainties. This may be due to intrinsic variation in the M_{K_S} – M_* relation or underestimated uncertainties in the input parallaxes and/or orbital parameters. The effect of [Fe/H] on the M_{K_S} – M_* relation is likely negligible for metallicities in the Solar neighborhood ($3.8 \pm 2.1\%$ change in mass per dex change in [Fe/H]). The weak effect of [Fe/H] is consistent with predictions from the Dartmouth Stellar Evolution Database, but inconsistent with those from MESA Isochrones and Stellar Tracks (at $> 4\sigma$). A sample of binaries with a wider range of abundances will be required to see if metallicity becomes important for more extreme populations (e.g., in the Galactic Halo or thick disk).

Keywords: stars: fundamental parameters; stars: low-mass; stars: luminosity function, mass function

Corresponding author: Andrew W. Mann
mann.andrew.w@gmail.com

* Hubble Fellow

† 51 Peg b Fellow

1. INTRODUCTION

Over the past decade, M dwarfs have become critical for a wide range of astrophysics. On the small scale, M dwarfs are attractive targets for the identification and characterization of exoplanets. The small size, low mass, and low luminosity facilitates the discovery of small planets (e.g. Muirhead et al. 2012b; Martinez et al. 2017; Mann et al. 2018) and those in their circumstellar habitable zone (e.g., Tarter et al. 2007; Shields et al. 2016; Dittmann et al. 2017). Close-in, rocky planets are also significantly more common around M dwarfs than their Sun-like counterparts (Dressing & Charbonneau 2013; Petigura et al. 2013; Mulders et al. 2015; Gaidos et al. 2016)

The properties of both the Milky Way and more distant galaxies are inexorably linked to parameters of their most numerous constituents (>70% of stars in the Solar neighborhood are M dwarfs, Henry et al. 1994; Reid et al. 2004). Late-type dwarfs weigh heavily on the Galactic mass function (e.g., Covey et al. 2008), and are useful probes of the Milky Way’s structure (e.g., Jurić et al. 2008; Ferguson et al. 2017), kinematics (e.g., Bochanski et al. 2007; Yi et al. 2015), and chemical evolution (Woolf & West 2012; Hejazi et al. 2015). Although K and M dwarfs are much fainter than their higher-mass counterparts, they measurably contribute to the integrated spectra of massive galaxies; thus M dwarf fundamental properties have become an essential component to studies of extragalactic initial mass functions (e.g., Conroy & van Dokkum 2012; McConnell et al. 2016) and mass-to-light ratios (Spinelli et al. 2015). M dwarf - white dwarf pairs are a plausible progenitor for Type Ia supernovae (Wheeler 2012), and hence late-type stars are important to understand even for cosmological problems.

For all these areas, it is essential that we have a method to estimate the fundamental parameters of late-type dwarfs. For exoplanet research, this means stellar radii for planet radii in transit surveys, stellar masses for planet masses in radial velocity surveys, and both (stellar densities) for determining planet occurrence rates, internal structure, and habitability. Spectra, photometry, and distances of stars provide a relatively direct means to measure T_{eff} (e.g., Rojas-Ayala et al. 2012; Mann et al. 2013b), luminosity (e.g., Reid et al. 2002), metallicity (e.g., Bonfils et al. 2005; Rojas-Ayala et al. 2010), and radius (e.g., via Stefan-Boltzmann, Newton et al. 2015; Kesseli et al. 2018). Masses are much more difficult to infer from observations alone, yet they are one of the most important and fundamental properties of a star.

In the case of a binary, it is possible to directly determine the mass of a star from its orbital parameters and Kepler’s laws. For systems with reasonably short orbital

periods, this can be done by monitoring the motion of the stars over time. Radial velocity variation can yield individual stellar masses but only modulo the sine of the orbital inclination (e.g., Torres & Ribas 2002; Kraus et al. 2011; Stevens et al. 2017). In systems where binary components are spatially resolved, monitoring of their position angle and separation can yield a measurement of the total system mass, assuming the parallax is known (e.g., Söderhjelm 1999; Woitas et al. 2003; Dupuy et al. 2009b). Absolute orbital astrometry (measured with respect to background stars) can even yield both individual masses and a direct measurement of the system’s parallax (e.g., Köhler et al. 2012; Benedict et al. 2016).

Microlensing can provide mass measurements for single stars (e.g., Zhu et al. 2016; Chung et al. 2017; Shin et al. 2017). Unfortunately, this method cannot be used to target specific M dwarfs of interest (such as exoplanet hosts), and detected microlensing events are both rare and primarily limited to distant (\sim Kpc) targets in crowded fields (e.g., the bulge), where follow-up is difficult.

Instead, mass estimates of targeted and nearby single stars derived from evolutionary models (e.g., Muirhead et al. 2012a; Conroy & van Dokkum 2012). However, differences between empirical and model-predicted mass-radius and radius-luminosity relations for late-type stars (e.g., Boyajian et al. 2012; Feiden & Chaboyer 2012) raise concerns about the reliability of model-based masses. Further, the masses derived depend on both the model grid used (Spada et al. 2013; Choi et al. 2016), and the observed parameter over which the interpolation is done (e.g., color versus luminosity, Mann et al. 2012, 2015). Ultimately, these models need to be tested empirically; differences between the models and empirical determinations can reveal important missing physics or erroneous assumptions in the model grids.

An empirical approach to estimating single-star masses is through a relation between mass and luminosity (e.g., Henry & McCarthy 1993; Delfosse et al. 2000), calibrated with dynamical mass measurements from binary stars. Absolute magnitude can be used as a proxy for luminosity, and is generally easy to measure for visual binaries from the same data used to establish the orbit (resolved images/astrometry and a parallax). Because late-type stars evolve slowly on the main sequence, the stellar locus in mass-luminosity space is tight for a fixed metallicity. Using near-infrared instead of optical magnitudes mitigates the effect of metallicity, as detailed abundances have a weaker effect on the absolute flux levels of M dwarfs past $1.2\mu\text{m}$ when compared to optical regions (Bonfils et al. 2005; Delfosse et al. 2000). Combined with the favorable Strehl ratios in adaptive optics imaging at

K-band, this has made the $M_K - M_*$ relation the most precise and commonly used technique.

Empirical $M_K - M_*$ relations from Henry & McCarthy (1993) and Delfosse et al. (2000) provide mass determinations to $\simeq 10\%$ precision, with more recent improvements by Benedict et al. (2016). However, as fields that rely on M dwarf parameters have pushed to higher precision, there has been increasing need for proportionate improvements in stellar mass precision. Further, since the advent of Gaia parallaxes, even late-type dwarfs beyond the Solar neighborhood now have $< 1\%$ parallaxes, making scatter in the $M_{K_S} - M_*$ relation the primary source of uncertainty. Existing relations have gaps in their calibration sample, particularly below $0.1M_\odot$, where there is need for stellar masses to match new exoplanet surveys (e.g., Gillon et al. 2017). Lastly, methods to measure metallicities of M dwarfs have become increasingly precise (e.g., Rojas-Ayala et al. 2010; Neves et al. 2014), and now extend to the end of the M-dwarf sequence (Mann et al. 2014), making it possible to explore the impact of metallicity on the $M_{K_S} - M_*$ relation.

Here we present a revised empirical relation between M_* , M_{K_S} , and [Fe/H], spanning almost an order of magnitude in mass, from $0.075M_\odot$ to $0.70M_\odot$ and typical metallicities in the Solar neighborhood ($-0.6 < [\text{Fe}/\text{H}] < +0.4$). The relation is built on orbital fits to visual binaries from a combination of adaptive optics imaging and astrometric measurements in the literature with metallicities estimated from the stars' near-infrared spectra. In Section 2 we detail our selection of nearby late-type binaries with orbits amenable to mass determinations. We overview our astrometric and spectroscopic observations in Section 3, including those from telescope archives and the literature. Our orbit-fitting procedure is explained in Section 5. We describe our method to determine other parameters of each system ([Fe/H], distance, and M_{K_S}) in Section 6. Our technique to fit the $M_{K_S} - M_*$ relation from these binaries is described in Section 7, including an analysis of the errors as a function of M_{K_S} , a detailed look at the effects of [Fe/H], and a comparison to earlier relations. We conclude in Section 8 with a brief summary, and a discussion of the important caveats and complications to consider when using our relation, as well as future directions we are taking to expand on the work given here.

If you want to use the relations in this manuscript, we advise at least reading Section 8.2 to understand the potential limitations of the program and posteriors we provide.

2. SAMPLE SELECTION

Our selection of binaries was designed to sample the region of mass space over which the mass-luminosity relation should not evolve significantly between the zero-age main sequence and the age of the Galactic disk (~ 10 Gyr). We quantified this using the Baraffe et al. (2015) models, which we show in Figure 1. Above $0.70M_\odot$, a fixed luminosity (the observable) could correspond to a $\simeq 5\%$ range in masses over 1-10 Gyr. Stars below $\simeq 0.1M_\odot$ take a long time (100-1000 Myr) to arrive on the main sequence, but obey a tight relation beyond this point. Those objects below $\simeq 0.08M_\odot$ are predicted to never reach the main sequence and hence obey no mass-luminosity relation. However, this transition likely depends on metallicity, and empirical efforts studies have found a limit closer to $0.075M_\odot$ (e.g., Dieterich et al. 2014; Dupuy & Liu 2017). We therefore attempted to select systems spanning $0.075M_\odot \lesssim M_* \lesssim 0.70M_\odot$.

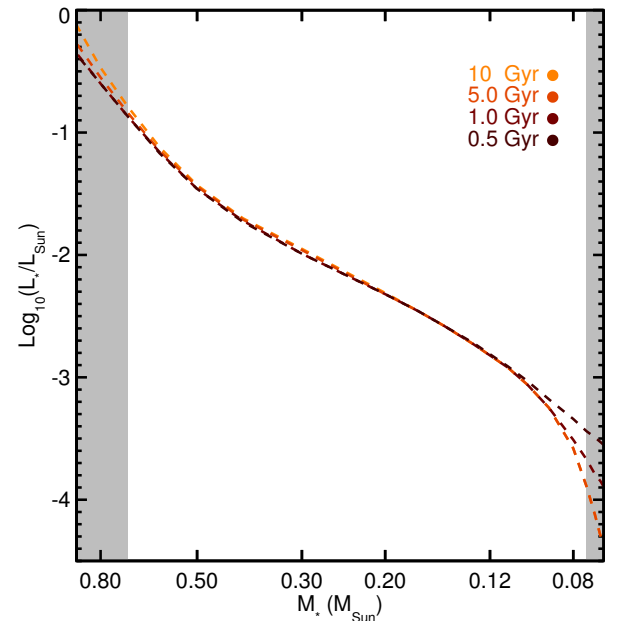


Figure 1. Stellar luminosity as a function of mass predicted by the Baraffe et al. (2015) models, color-coded by age (metallicity fixed at Solar). The grey regions denote masses excluded by this study due to a significant age dependence on the mass-luminosity relation.

We first selected systems by cross-matching catalogs of nearby M dwarfs (Lépine et al. 2013; Gaidos et al. 2014; Dittmann et al. 2014; Winters et al. 2015), with the fourth catalog of interferometric measurements of binary stars (INT4, Hartkopf et al. 2001), and adaptive optics (AO) images from the Keck Observatory Archive (KOA). As part of this cross-match, we also included targets matching the M dwarf selection criteria of Gaidos

et al. (2014), but with a bluer color cut ($V - J > 1.8$) to incorporate additional late-K dwarfs. We kept any binaries with separations less than $5''$. We then added in other known late-type binaries from Law et al. (2008), Janson et al. (2012), Janson et al. (2014), and Ward-Duong et al. (2015). This provided a list of more than 300 multi-star systems.

From here we selected binaries for which we expect to be able to obtain a precise orbit on a reasonable (few year) timescale. We assumed that the average of available (literature) separation measurements approximate the semi-major axis of the system. This biased our selection towards wider binaries than expected, but served to keep the sample more inclusive. Next we identified systems for which the time between the first available observation and our final observation would span at least 30% of the orbit (based on our rough semi-major axis estimate), including the two years of our orbital monitoring program with Keck. This cut accounted for existing data. As a result, long-period binaries with extensive previous observations were included, depending on the baseline available, while those with only recent epochs would generally need to have orbits of $\ll 10$ years to be targeted. After this cut we were left with 129 systems. Excluding 36 systems at $\delta < -30 \text{ deg}$ that are difficult to observe from Maunakea, 93 systems were included in our observing program.

We removed 16 systems from our analysis because of an unresolved tertiary (or quaternary) component noted in the literature (e.g., Law et al. 2010; Tokovinin & Smekhov 2002; Tokovinin 2018). In their current form, such systems were not useful for our analysis, as we had no ΔK magnitudes or mass ratios for the unresolved components. Since many of these are double- or triple-lined systems, it is possible to recover their parameters with multi-epoch radial velocities, and some systems have the necessary data in the literature (e.g., Ségransan et al. 2000). We continued to monitor these systems with high-resolution near-infrared spectrographs (Yuk et al. 2010; Rayner et al. 2012; Park et al. 2014), but they were excluded from the analysis done here. High-order systems where all components are resolved (e.g., GJ 2005 ABC) were retained, although we only focus on the tighter pairs in this work.

A total of 17 systems were flagged as young, i.e., affiliated with nearby young moving groups or clusters or with obvious signs of low gravity, high luminosity, or similar spectroscopic youth indicators (Shkolnik et al. 2012; Kraus et al. 2014; Gagné et al. 2014; Malo et al. 2014; Gagné et al. 2015; Riedel et al. 2017; Shkolnik et al. 2017; Rizzuto et al. 2017; Lee & Song 2018). We monitored these targets even after flagging them as young, but they were not included in the analysis for this paper.

Many of these are likely pre-main-sequence stars and hence will not follow the same mass-luminosity relation. Even for those that are on the main-sequence, young M dwarfs may have higher luminosities for a given mass due to effects of activity and spots (e.g., Kraus et al. 2015; Stassun et al. 2012; Somers & Stassun 2017). These young systems will be the subject of a future study into the effects of age and activity on the parameters of M dwarfs.

After the completion of our observing program, we removed targets with fewer than six independent astrometric measurements and those lacking a precise parallax ($\sigma_\pi > 7\%$). We attempted to fit orbits of the remaining 57 systems (Section 5). Five of the resulting orbital parameters yielded system masses for the system too imprecise (>20% errors on M_{tot}) to be useful for our analysis. This left us with 52 binaries (104 stars).

We added in seven targets with orbits from Dupuy & Liu (2017), primarily to fill in the sample around the end of the M dwarf sequence. These seven were selected because they are theoretically massive enough to sustain hydrogen fusion and satisfy all our other selection criteria. Systems from Dupuy & Liu (2017) also had their orbits fit using a nearly identical method to our own, often using similar or identical sources of data and analysis methods (primarily Keck/NIRC2). Two additional systems in Dupuy & Liu (2017) matched our initial cut, but were still omitted from this analysis. These were LP415-20, which Dupuy & Liu (2017) suggest is an anomalous system and possibly an unresolved triple, and 2M1847+55, which has a relatively imprecise orbit compared to the rest of the sample.

Parameters of the final 59 systems included in our analysis are given in Table 3.

3. OBSERVATIONS AND DATA REDUCTION

3.1. Near-infrared Spectra with IRTF/SpeX

To estimate the metallicities of our targets we obtained near-infrared spectra for 56 of 59 targets using the SpeX spectrograph (Rayner et al. 2003) on the NASA Infrared Telescope Facility (IRTF) atop Maunakea. Observations were taken between May 2011 and November 2017. Most data were taken as part of programs to characterize the fundamental properties of nearby M dwarfs (e.g., Mann et al. 2013b; Gaidos et al. 2014; Terrien et al. 2015). All spectra were taken in SXD mode, providing simultaneous wavelength coverage from 0.9 to $2.5\mu\text{m}$. For 56 of the targets, observations were taken using the $0.3 \times 15''$ slit, which yielded a resolution of $R \simeq 2000$. Spectra for two targets (2M2206-20 and 2M2140+16) were taken from Dupuy et al. (2009a) and Dupuy & Liu (2012),

which used the $0.5 \times 15''$ and $0.8 \times 15''$ slits (respectively), yielding spectral resolutions of $\simeq 750\text{-}1500$.

For Gl 65 and HD 239960 the SpeX slit was aligned to get spectra of both targets simultaneously. For all other targets the binary was unresolved or too poorly resolved to separate in the reduction procedure, and instead the slit was aligned with the parallactic angle. Each target was nodded between two positions along the slit to remove sky background. Depending on the target brightness and conditions, between 6 and 30 individual exposures were taken following this nodding pattern, with exposure times varying from 8s to 180s. An A0V-type star was observed immediately before or after each target to measure (and remove) telluric lines and flux calibrate the spectrum. The final stacked spectra had S/N of > 100 per resolving element in the K -band for all but the four faintest targets (which had S/N > 50).

Basic data reduction was performed with `SpeXTool` package (Cushing et al. 2004). This included flat fielding, sky subtraction, extraction of the one-dimensional spectrum, wavelength calibration, stacking of individual exposures, and merging of individual orders. Telluric lines were removed and the spectrum was flux calibrated using the A0V star observations and the `xtellcor` software package (Vacca et al. 2003). When possible, the same A0V star was used for multiple targets taken near each other in time.

Two of the three targets lacking SpeX spectra are too warm (earlier than K5) to derive a metallicity from NIR spectra (Gl 792.1 and Gl 765.2), and the third (Gl 54) is too far south to be observed with IRTF.

3.2. Adaptive Optics Imaging and Masking

We analyzed a mix of AO data from our own program with Keck/NIRC2 and archival imaging from the Keck II Telescope, the Canada France Hawaii Telescope (CFHT), the Very Large Telescope (VLT), and the Gemini North Telescope. In general we analyzed all usable images (e.g., non saturated, components resolved) regardless of observing mode and filter.

For our analysis, we considered a single dataset a collection of observations with a unique combination of filter, target, and epoch. Each combined dataset consisted of a Δm (for a given filter), separation, and position angle.

We separate the observations and reduction by instrument/telescope below. The full list of astrometry and contrast measurements is given in Table 5, sorted by target and date.

3.2.1. Keck II/NIRC2 Imaging and Masking

As part of a long-term monitoring program with Keck II atop Maunakea, between June 2015 and November

2017 we observed 49 of the 52 multiple-star systems fit in this paper. All observations were taken using the facility AO imager NIRC2 in the vertical angle mode (fixed angle relative to elevation axis) and the narrow camera (≈ 10 mas pixel $^{-1}$). Depending on target brightness and observing conditions, images were usually obtained through either the K' ($\lambda_c = 2.124\mu\text{m}$) or narrow K_{cont} ($\lambda_c = 2.2706\mu\text{m}$) filters, and non-redundant aperture masking (NRM) was always taken using the 9-hole mask and K' filter. After acquiring the target and allowing the AO loops to close, we took four to 10 images or 6-8 interferograms, adjusting coadds and integration time based on the brightness of the target. As most of our targets are bright, observations were usually taken using the Natural Guide Star (NGS) system (Wizinowich et al. 2000; van Dam et al. 2004), only utilizing the Laser Guide Star (LGS) mode for the faintest ($R \gtrsim 13$) targets or in poor conditions. In total, our observations provided 154 datasets.

In addition to our own data, we downloaded images from the Keck Observatory Archive (KOA), spanning March 2002 to November 2015, all of which were taken with the NIRC2 imager. Archival data comprised a wide range of observing modes, filters, and cameras, although the majority was taken with the narrow camera and either the H - or K -band filter. We included nearly all data with clear detections of both binary components independent of the observing setup. We discarded saturated images, those taken with the coronagraph for either of the component stars, and where the target is completely unresolved. A total of 36 datasets were used from the archive.

The same data reduction was applied to observations both from our own program and from the archive, following our custom procedure described in Kraus et al. (2016). To briefly summarize, we corrected for pixel value nonlinearity in each frame then dark- and flat-corrected it using calibrations taken the same night. In cases where no appropriate darks or flats were taken in the same night, we use a set from the nearest available night. We interpolated over “dead” and “hot” pixels, which were identified from superflats and superdarks built from data spanning 2006 to 2016. Because flats are rarely taken in narrowband filters, we used superflats built from the nearest (in wavelength) broadband filter where appropriate (e.g., for K_{cont} we used K' flats). Pixels with flux levels $> 10\sigma$ above the median of the eight adjacent pixels (primarily cosmic rays) were replaced with the median (average of the 4th and 5th ranked). Images were visually inspected as part of identifying the binary location, and a handful (<1%) of images were negatively impacted by our cosmic ray removal (e.g., removal of

part of the source). For these, we used the data prior to rejecting cosmic-ray.

3.2.2. CFHT/PUEO Imaging

We obtained data for 31 of our targets from the Canadian Astronomy Data Centre archive, taken with the 3.6m Canada-France-Hawaii Telescope (CFHT) using the Adaptive Optics Bonnette (AOB, often referred to as PUEO after the Hawaiian owl, Arsenault et al. 1994) and the KIR infrared camera (Doyon et al. 1998). After removing bad observations (e.g., saturated, unresolved, or poor AO correction), a total of 226 datasets were included. Observations spanned December 1997 to January 2007, covering most of the time PUEO was in use at CFHT (1996 to 2011). Most observations were taken in a few-year period from 2000 to 2003. Observations spanned a range of filters across *JHK* bands, but the majority used either the narrowband Br γ or [FeII] filters. All observations used a 3-5 point dither pattern and took at least two images at each dither location.

Data reduction for PUEO observations followed the same basic steps as our NIRC2 data. We first applied flat-fielding and dark correction using a set of superflats and superdarks built by splitting the datasets into 6 month blocks and combining calibration data within the same time period. We identified bad pixels by median filtering stacks of science images taken of dozens of objects, which were then replaced with the median of the eight surrounding pixels. To identify cosmic rays, we median-filtered consecutive images of each target (at a fixed location), then compared the stack to individual images. Pixels $> 10\sigma$ above the robust mean of the stacks are replaced with the median of the eight surrounding points. Because PUEO/KIR data were taken in sets of >5 images before the object was dithered, this median-filtering was effective for removing nearly all cosmic rays.

3.2.3. VLT/NaCo Imaging

We downloaded AO-corrected images from the ESO archive taken with the Nasmyth Adaptive Optics System Near-Infrared Imager and Spectrograph (NAOS-CONICA, or NaCo) instrument on VLT. Data spanned November 2001 to October 2016, with about half of these 70 datasets taken from 2001 to 2005. Based on the program abstracts, $\lesssim 1/2$ of the observations were meant to use these binaries as astrometric or photometric calibration (e.g., science case is unrelated to M dwarfs or binaries). Data covered 20 of our targets, excluding saturated or otherwise unusable data. Observations were taken with a wide range of filters, cameras, and observing patterns, but the majority were taken using the S13 camera ($\approx 13 \text{ mas pixel}^{-1}$) with either broadband K_s and

L , or narrowband [FeII] and [Br γ] filters, and always following a 2-4 point dither pattern.

Basic data reduction was applied to NaCo images following a similar procedure with the PUEO and NIRC2 data. We applied flat-fielding and dark corrections to each observation using the standard set of calibrations taken each night as part of the VLT queue. In the case where calibration (dark or flat) images were missing or unusable, we used the nearest (in time) set of calibration images matching the filter (for flats) and exposure setup (for darks). Flats taken in broadband filters were used for flat-fielding narrow-band images at similar wavelengths. We built bad pixel masks using median stacks of all images taken within a night after applying flat and dark corrections. To identify and remove cosmic rays we used the L.A. Cosmic software (van Dokkum 2001).

3.2.4. Gemini/NIRI Imaging

We retrieved 39 datasets for 8 of our targets from the Gemini archive, all taken with the AO imager NIRI (Hodapp et al. 2003) on the Frederick C. Gillett Gemini Telescope (Gemini North). All observations were taken between August 2008 and February 2011 and were taken with the assistance of the ALTtitude conjugate Adaptive optics for the InfraRed (ALTAIR). Most observations were taken with the f32 camera ($\approx 21 \text{ mas pixel}^{-1}$) using broadband J -, H -, or K -band filters. All observations followed a 2-4 point dither pattern and took at least two images at each dither location.

Data from NIRI were reduced using the same basic methods as for all other adaptive optics data. First, we applied flat and dark corrections to each set of images using the standard calibration images taken as part of the Gemini queue, usually within 24h of the target observations. In most cases, flats taken in broadband filters were used for narrowband flat-fielding. We then identified bad pixels from median filtering of all images within a given night. Observations with a target near or on top of a heavily impacted pixel (identified with the mask) were discarded. We used the L.A. Cosmic software for the identification and removal of cosmic rays.

4. ASTROMETRY AND PHOTOMETRY

Extracting separations and position angle measurements followed a similar multi-step procedure across all instruments, excluding the NRM data (which is described below). Our method is based largely on that described in Dupuy et al. (2016) and Dupuy & Liu (2017), which is built on the techniques from Liu et al. (2008) and Dupuy et al. (2010) and we briefly describe here.

We first cross-correlated each image with a model Gaussian PSF to identify the most significant peaks.

The cross-correlation peak occasionally centers on instrumental artifacts, often struggles to separate out partially overlapping binaries, and can easily identify the wrong source for triple systems. So this step was checked by eye and updated as needed. The eye-check phase also allowed us to manually remove data of poor quality: e.g., no or poor AO correction, saturated data, or an unresolved system. We used these centers as the initial guess for the x, y pixel position used in the next phase.

We then fit the PSF centers by either: 1) running **StarFinder**, a routine designed to measure astrometry and photometry from adaptive optics data by deriving a PSF template from the image and iteratively fitting this model to the components (for more details, see Diolaiti et al. 2000), or 2) fitting the binary image with a PSF modeled by three-component elliptical 2D Gaussians using the least-squares minimization routine MPFIT (Markwardt 2009). Although the results of these two methods generally agreed, **StarFinder** was preferred, as it used a non-parametric and more realistic model of the PSF and worked even with mediocre AO correction, provided the component PSFs were well separated. **StarFinder**, however, failed on the tightest binaries, where it was unable to distinguish two stars and thus incorrectly built a pathological, extended PSF that fit the blended image. The Gaussian fit was used for these cases where **StarFinder** failed.

As part of the PSF fit, both methods provide a flux ratio of the PSF normalization factors, which we used to determine the contrast Δm in the relevant band. Data from all filters are used for astrometry, although only ΔK measurements were used in the estimate of M_{K_S} (see Section 6.3).

PSF fitting provides pixel-position (x, y) measurements of each component, but converting these to separation (ρ) and position angle (PA) on the sky requires an astrometric calibration of the instrument. For the NIRC2 narrow camera, we used the Yelda et al. (2010) distortion solution for data taken before 2015 Apr 13 UT, and Service et al. (2016) for data taken after this. These calibrations include a pixel scale and orientation determination of 9.952 ± 0.002 mas pixel $^{-1}$ and 0.252 ± 0.009 deg for the former, and 9.971 ± 0.004 mas pixel $^{-1}$ and 0.262 ± 0.020 deg for the latter. For the NIRC2 wide camera we used the solution from Fu et al. (2012, priv. comm.)¹, with a pixel scale of 39.686 ± 0.008 mas pixel $^{-1}$ and the same orientation as the narrow camera. For the f/32 camera

¹ <http://homepage.physics.uiowa.edu/~haifu/idl/nirc2wide/>

on NIRI, we used the distortion solution from the Gemini webpage².

For other instruments and cameras, data were always taken following a dither pattern to sample different regions of the CCD distortion pattern. So the RMS between dithered images should reflect errors due to uncorrected distortion (which is included in our errors; see below). For KIR, we adopted a pixel scale of 34.8 ± 0.1 mas pixel $^{-1}$ (Stapelfeldt et al. 2003) and an orientation of 0 ± 2 deg³. For NaCo, we assumed a pixel scale of 13.24 ± 0.05 mas pixel $^{-1}$ for the S13 camera (Masciadri et al. 2003; Neuhauser et al. 2005) and the values given in the ESO documentation for all others⁴ (with the same error). The rotation taken from the NaCo headers was assumed to be correct to 0.4 deg. (Seifahrt et al. 2008). For NIRI observations, we used a pixel scale provided in the Gemini documentation⁵ for each camera (117.1, 49.9, and 21.9 mas pixel $^{-1}$ for f/6, f/14, and f/32, respectively), with a global uncertainty of 0.05 mas pixel $^{-1}$ on the pixel scale and 0.5 deg. on the orientation (Beck et al. 2004).

Calculation of separations and position angles from non-redundant masking (NRM) observations followed the procedures in the appendix of Kraus et al. (2008) with the aid of the latest version of the “Sydney” aperture-masking interferometry code⁶. To remove systematics, each NRM observation of a science star was paired with that of a single calibrator star taken in the same night with a similar magnitude and airmass. Binary system profiles were then fit to the closure phases to produce estimates of the separation, position angle, and contrast of the binary components. More details on the analysis of masking data can be found in Lloyd et al. (2006), Kraus et al. (2008), and Evans et al. (2012).

All data in a single set (same target, filter, and night) were combined into a single measurement (after applying all corrections above), with errors estimated using the RMS in the individual images within a night. This scatter across images was combined with the uncertainty in the orientation and pixel scale in quadrature. We assumed that the pixel scale and orientation uncertainties were completely correlated within a night and filter so they do not decrease with \sqrt{N} .

We also corrected separation and position angle for differential atmospheric refraction (Lu et al. 2010) using filter wavelength information and weather data from the

² <http://www.gemini.edu/sciops/instruments/niri/undistort.pro>

³ KIR specifications, filters, and performance.

⁴ NaCo Documentation, user manual, calibration, and reduction.

⁵ NIRI pixel scales, field of view, and field orientation.

⁶ <https://github.com/mikeireland/idlnrm>

header (for VLT) or from the CFHT weather archive⁷ (for Keck, CFHT, and Gemini). We neglected the chromatic component of this effect as the correction is already small compared to measurement errors.

4.1. Literature Astrometry

We included measurements from the literature for 50 of the 52 binaries in our sample for which we analyzed astrometry. To help identify sources of astrometry, we used the fourth catalog of interferometric observations of binary stars (INT4, Hartkopf et al. 2001). We only used measurements that included both a separation and position angle. In cases where the literature data was also available in one of the archives above (i.e., the same dataset used in the reference), we adopted our own measurements over the literature data to ensure more homogeneous measurements and errors. We did not utilize Δm measurements from the literature, although in some cases this information was used to verify the astrometry was for the correct binary system or component.

In total, we used 558 measurements (each including a separation and position angle) from 60 references. The literature astrometry was very non-uniform; roughly half of the points were for just 11 targets, predominately taken with the goal of measuring their orbits. Approximately 180 measurements came from speckle observations on the Special Astrophysical Observatory (SAO) 6m (e.g., Balega et al. 2002), WIYN (e.g., Horch et al. 2017), or SOAR (Tokovinin 2017) telescopes. About 160 points came from *HST*, primarily Fine Guidance Sensors measurements of ~ 10 binaries (e.g., Benedict et al. 2016). The rest of the measurements are from a mix of surveys focusing on taking many epochs of specific systems to determine orbits (e.g., Köhler et al. 2012) and broader surveys (e.g., for multiplicity) that obtain 1-2 epochs on each of dozens of binaries (e.g., Janson et al. 2012).

One complication using older literature astrometry is inhomogeneous reporting of separation and position angle errors. Many references provided measurements without errors, and many more reported errors without accounting for field distortion or errors in the pixel scale and orientation. We mitigated this problem by generating an error common to a given reference. For each literature source, we identified a set of binaries where an orbit can be fit (with $< 5\%$ errors on the angular separation) without astrometry from that particular reference. Some literature sources were merged for this comparison, provided they used the same instrument and basic analysis. We included binaries outside the sample considered here. We fit the orbit following the method outlined in

Section 5, using only the least-squares method for efficiency. We then compared the expected position angle and separation to the measurements from the reference in question. From this difference we computed the required missing error term, which, when added in quadrature with the reported errors (zero for those without errors) would yield a reduced χ^2 (χ_ν^2) of 1. References where we could not test the reported errors (e.g., due to insufficient data) and those with extremely large added error terms (> 50 mas) were not used. No reference gave a negative term (over-reported errors).

All literature astrometry used in this paper is listed alongside our own measurements in Table 5.

4.2. Summary of input astrometry

In total we measured or gathered 1083 unique datasets (unique filter/night/target combinations), approximately half of which we measured from adaptive optics images (525) and the other half were drawn from the literature (558). Most of the astrometry measurements derived from our analysis came from either NIRC2 (190) or PUEO (226), with a smaller contribution from NaCo (70) and NIRI (39).

Although they represent only $\simeq 20\%$ of the total astrometric measurements, the NIRC2 measurements are the most critical in constraining orbital parameters. NIRC2 astrometry was 1-2 orders of magnitude more precise than those from the literature, and a factor of 3-8× more precise than those from PUEO, NIRI, and NaCo. We characterized the relative importance of each data source using the total number of unique separation measurements weighted by their uncertainties ($1/\sigma$). Under this metric, the NIRC2 points contributed $\gtrsim 10\times$ more orbital information than the literature data. Measurements from CFHT/PUEO had a comparable total contribution to the literature data, each of which had $\simeq 2\times$ the impact of NaCo measurements, and $\simeq 3\times$ that of data from NIRI. This comparison likely underestimated the importance of the NIRC2 data; literature and archive images tended to be concentrated on the best-characterized systems, while our NIRC2 observations were specifically coordinated to complete orbits and cover under- or un-sampled regions of binary orbits. However, the combination of NIRC2 and literature and/or PUEO points is the most useful, since this provides both the precision and long baseline (PUEO and NIRC2 data is typically separated by > 10 years) needed to fully constrain the orbital parameters.

5. ORBIT FITTING

We fit the astrometry with the Monte Carlo Markov Chain (MCMC) software `emcee` (Foreman-Mackey et al. 2013), a Python implementation of the affine-invariant

⁷ CFHT weather archive.

ensemble sampler (Goodman & Weare 2010). For each system, we explored seven orbital elements: the orbital period (P), combined angular semi-major axis (α), eccentricity (e), inclination (i), epoch of periastron passage (T_0), argument of periastron (ω), and position angle of the line of nodes (Ω). Parameters were limited by physical or definitional constraints, e.g., $P > 0$, $0 \leq e < 1$, and $0 \leq i \leq \pi$, but were given no additional boundaries.

We applied non-uniform priors of $1/P$, $1/\alpha$, and $\sin(i)$ to P , α , and i , respectively. All other parameters evolved under uniform priors. Walkers were initialized with the best-fit orbit determined using *MPFIT* (Markwardt 2009) and a spread in starting values based on the *MPFIT* estimated errors. Each MCMC chain was initially run for 10^5 steps with 100 walkers.

We considered a chain converged if the total length was at least 50 times as long as the autocorrelation time (Goodman & Weare 2010). Every chain was also examined by eye for convergence. In about 1/4 of the systems the fit did not converge after the initial 10^5 steps, so we ran these for 10^6 total steps, which was sufficient for convergence for all included systems. We saved every 100 steps in the chain, and the first 5% of each chain was removed for burn-in. Longer burn-in time did not change the final posterior in any significant way, in part because the initial (least-squares) guesses were always near the final answer from the MCMC.

Systems of near-equal mass may have the primary and companion confused, both in our own measurements and also those taken from the literature. We identified such measurements by eye during the *MPFIT* stage and manually adjusted the position angles before starting the MCMC run. In total $\simeq 16$ measurements were corrected this way, almost all of which were for three systems with contrast ratios close to unity. A more robust solution to this problem would be to feed a double-peaked prior at the reported value and ± 180 deg. into the likelihood function. However, in all cases the problematic points were obvious by eye, had reported Δm consistent with zero, and a simple 180 deg correction completely fixed the orbit.

Overall the quality of the fits was extremely good, with χ^2_ν values ranging from 0.1 to 2, and a mean cumulative probability (the probability of getting the χ^2 or smaller given the degrees of freedom) of 47% across all targets. We show some example orbital fits in Figure 2 (with the full set in Appendix B) and provide the median orbital parameters in Table 4. Orbits span a wide range in period; the tightest binaries have $P < 1$ yr, while the widest have $P > 50$ yr. The two systems with $P > 50$ yr (Gl 301 and Gl 277) were also some of the least-well characterized. No systems show evidence of period-

doubling due to limited sampling, an advantage of using data with non-uniform temporal sampling.

Our orbital fits made heavy use of literature astrometry, many of which had no reported errors. Our method for assigning or correcting errors assumed that all measurements have a common missing error term per source (Section 4.1). It is more likely that errors depend on the separation and contrast ratio, as well as quantities that were not consistently reported, like weather, setup, and observational strategy. Further, this technique assumed an uncorrelated error term. In the case of an erroneous pixel scale or imperfectly aligned instrument, all measurements from a common instrument err in the same sense. In practice, it is difficult to correct for these effects without access to the actual images. The data suggest this does not impact our results; the final χ^2_ν values for the best-fit orbits shows no correlation with the fraction of astrometry from the literature versus our own measurements, and astrometry from our own measurements agrees well with the literature data.

As an additional test, we tried refitting six binaries with the most literature data twice, first doubling the error term added to the literature points, then halving it. In all cases, overall parameters and errors did not change significantly (although the final χ^2_ν values changed). The main reason for this is that our new measurements (particularly those from NIRC2) are far more precise (with the exception of literature measurements from *HST*) and hence dictate the final solution, even in cases where most of the individual measurements are from the literature. In the case of halving errors, the MCMC landed on a similar solution, but with smaller parameter uncertainties and increased χ^2 values. We conclude this treatment of errors does not significantly impact our final orbital fits and that our assigned errors are reasonable overall.

6. STELLAR PARAMETERS

6.1. Parallaxes

Parallaxes for 56 of the 59 systems were drawn from the literature. In general we adopted the most precise parallax available, although preference was given to those accounting for centroid motion of the binary and those with a baseline significantly different from the binary's orbital period. A few systems are in hierarchical triples with a wider companion that has a separate (mostly independent) parallax measurement, which we used where possible. For $\simeq 1/3$ of the sample, we drew parallaxes from the new reduction of the Hipparcos data (van Leeuwen 2007). We used parallaxes from Dupuy & Liu (2017) for the seven overlapping binaries, and from Benedict et al. (2016) for 13. For nine systems we pulled

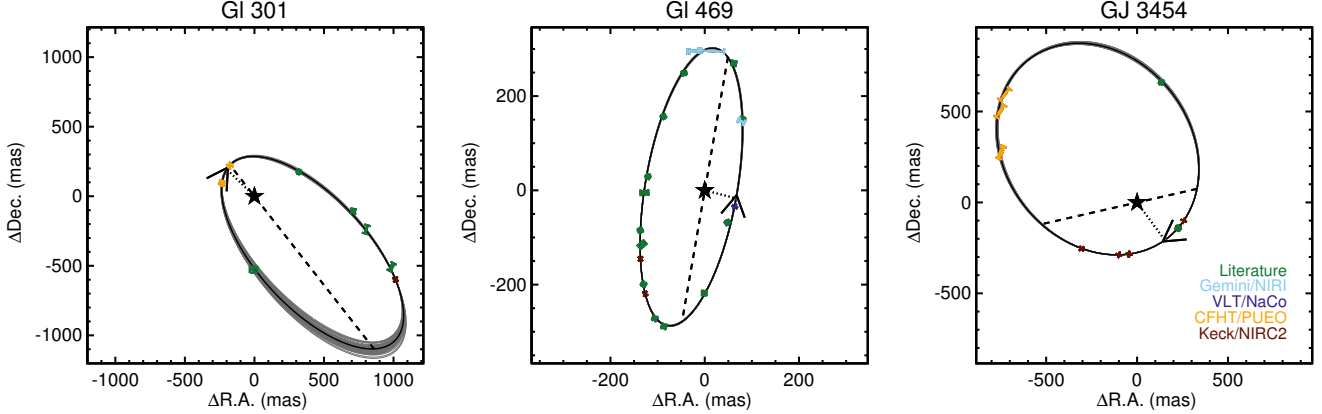


Figure 2. Example results of our orbit fitting procedure for Gl 301AB (left), Gl 469AB (middle), and GJ 3454AB (right). Points are individual measurements of the separation and position angle, color-coded by the astrometry source. Black solid line shows the best-fit (highest likelihood). Dark grey lines are drawn by randomly sampling 50 orbit fits from the MCMC chain to display an estimate of the errors. The dotted line connects periastron passage, with an arrow pointing in the orbital direction, and the dashed-line showing the line of nodes. For Gl469AB, high-quality astrometry is available for the full orbit, and the resulting errors on orbital parameters are so small that the grey lines cannot be seen. All orbits are shown in Appendix A.

parallaxes from the general catalogue of trigonometric parallaxes (van Altena et al. 1995).

About half (28) of our targets do not have entries in the second data release of Gaia (DR2, Lindegren et al. 2018; Gaia Collaboration et al. 2018). They were likely excluded because centroid shifts from orbital motion prevented a five-parameter (single-star) solution (a requirement to be included in DR2). We also found significant differences between the Gaia DR2 values and earlier measurements (including from TGAS, Michalik et al. 2015; Gaia Collaboration et al. 2016) even when measurements were available. Many wide triples in Gaia DR2 (where the third star is several arc seconds away, and hence easily resolved) have significantly different parallaxes reported for the unresolved pair than for the wider companion. For example, GJ 2069A has a Gaia parallax of 60.237 ± 0.080 mas, while GJ 2069C has a Gaia parallax of 62.02 ± 0.21 mas, a difference of 1.8 mas (7.9σ). Orbital motion is likely impacting the parallax values or uncertainties, an issue that should be resolved in future Gaia data releases that will include fits for orbital motion. We found no such issues with our other parallax sources. So we decided to not use Gaia DR2 parallaxes in most cases.

We ultimately adopted Gaia DR2 parallaxes for three systems, GJ1245AC, GJ277AC, and GJ4287AB, where we used the parallax of their wider common proper motion companion. In all cases the wider associated stars are not known to harbor another unresolved star, and hence they should not be impacted by the same binarity issue. GJ 570BC, Gl 695BC, GJ 2005BC, Gl 22AC, and 2M1047+40 also have nearby associated stars. However,

Gl 570A is extremely bright ($G \simeq 5$) and hence may have an unreliable parallax due to saturation in DR2, GJ 2005A has no entries in Gaia DR2, the available parallaxes (from *HST* and Hipparcos) for Gl 695BC and Gl 22AC are similar or more precise than the those reported for Gl 695A and Gl 22B from Gaia DR2, and the wide pair to 2M1047+40 is itself a tight binary (LP 213-67AB, Dupuy & Liu 2017) with a large reported excess astrometric noise in Gaia (a sign of binarity, Evans 2018).

For three systems we derived new parallaxes using MEarth astrometry (Nutzman & Charbonneau 2008). Updated parallaxes were measured following the procedure from Dittmann et al. (2014). The only difference was we used a dataset with a baseline \simeq two years longer, which helps average out systematic errors arising from centroid motion due to the binary orbit, and significantly reduces the overall uncertainties.

The remaining eight systems had parallaxes from a range of other literature sources, each containing just one or two systems in our sample. All adopted parallaxes and references are listed in Table 3.

6.2. Metallicity

We estimated [Fe/H] using our SpeX spectra and the empirical relations from Mann et al. (2013a) for K5-M6 dwarfs, and Mann et al. (2014) for M6-M9 dwarfs. These relations use a series of atomic lines (primarily Na, Ca, and K features) in the optical or NIR (e.g., Rojas-Ayala et al. 2010; Terrien et al. 2012), empirically calibrated using wide binaries containing a solar-type primary and an M-dwarf companion (e.g., Bonfils et al. 2005; John-

son & Apps 2009; Neves et al. 2012). The calibrations were based on the assumption that components of such binaries have similar or identical metallicities (e.g., Teske et al. 2015). Similar methods have been used extensively to assign metallicities across the M dwarf sequence (e.g., Terrien et al. 2015; Muirhead et al. 2015; Dressing et al. 2017; Van Grootel et al. 2018; Mace et al. 2018). Final adopted [Fe/H] values are given in Table 3. Errors account for Poisson noise in the spectrum, but because of the relatively high SNR of the spectra, final errors on [Fe/H] are generally dominated by the uncertainties in the calibration itself, conservatively estimated to be 0.08 dex (Mann et al. 2013a, 2014). However, we estimate that we can measure relative [Fe/H] values (one M dwarf compared to another) to 0.04 dex.

For all but two systems (Gl 65 and HD 239960), our NIR spectra are for the combined flux of the binary components. Mann et al. (2014) explored the issue of measuring metallicities of binaries with unresolved data by combining spectra of single-stars with equal metallicities and re-applying the same calibration. The bias introduced is negligible ($\lesssim 0.02$ dex) when compared to overall uncertainties. The added scatter is smaller than the measurement uncertainties, and can be almost entirely explained by the Poisson noise introduced in the addition of component spectra. This may be more complicated for nearly or marginally resolved systems, where the narrow slit (0.3'') is preferentially including light from one star. However, repeating the tests of Mann et al. (2014) and adding a random flux weighting to the fainter star produced a small change to the increased uncertainties (0.01-0.03 dex).

Two systems (2M2140+16, and 2M2206-20) have SpeX spectra taken with a wider slit, yielding lower spectral resolution. The bands in Mann et al. (2014) are defined using a homogeneous dataset taken with the narrow (0.3'') slit, so this difference may impact the derived [Fe/H]. We tested this by convolving a set of single-star SpeX spectra taken with the 0.3'' slit with a Gaussian to put them at the appropriate lower resolution. The median of the derived [Fe/H] values changed by < 0.01 dex, but the change varies between targets. Based on the resulting scatter, we estimate the errors on [Fe/H] from the lower-resolution spectra to be 0.12 dex on a Solar scale and 0.08 dex on a relative scale. These systems are marked separately in Table 3.

Two of the systems in our sample are L dwarfs (2M0746+20 and 2M1017+13). These are most likely above the hydrogen burning limit, and hence are included in our analysis. However, the Mann et al. (2014) method contains no L dwarf calibrators. Our derived [Fe/H] were extrapolations of the Mann et al. (2014)

calibration. The Mann et al. (2014) calibration has only a weak dependence on spectral type, but we still advise treating the assigned values with skepticism until an L dwarf calibration becomes available.

Two targets (Gl 792.1 and Gl 765.2) are too warm (earlier than K5) for the calibration of Mann et al. (2013a). For these we take [Fe/H] values from Casagrande et al. (2011) and Torres et al. (2010), respectively. These [Fe/H] measurements are not necessarily on the same scale as those from Mann et al. (2013a), which are calibrated against abundances of Sun-like stars from Brewer et al. (2015, 2016). Given reported variations in [Fe/H] for these stars, as well as [Fe/H] determination differences (Hinkel et al. 2014, 2016) we adopt conservative 0.08 dex uncertainties on both systems. For the other target lacking a SpeX spectrum (Gl 54), we derive [Fe/H] using the optical calibration of Mann et al. (2013a) and a moderate-resolution optical spectrum taken from Gaidos et al. (2014).

6.3. K_S -magnitudes

To determine K_S magnitudes for each component we required both unresolved (total) K_S for each system and the contrast (ΔK_S) for each component. We adopted unresolved K_S magnitudes from the Two Micron All Sky Survey (2MASS, Skrutskie et al. 2006). Some of the brightest stars in our sample are near or beyond saturation in 2MASS. For these targets we recalculated K_S magnitudes using available optical and NIR spectra, following the method of Mann & von Braun (2015) and Mann et al. (2015), using available optical spectra from Gaidos et al. (2014). Synthetic magnitudes were broadly consistent (mean difference of 0.003 ± 0.002 mag) with 2MASS K_S magnitudes (and at similar precision) for fainter targets ($K_S > 7$). We only updated K_S magnitudes for bright systems where our synthetic photometry differed from the 2MASS value by more than 2σ (five systems). We mark these systems in Table 3.

Reddening and extinction are expected to be $\simeq 0$ for all targets, as the most distant system is at 35 pc, while the Local Bubble (a region of near-zero extinction) extends to $\simeq 70$ pc (Aumer & Binney 2009). So we did not apply any extinction correction to the adopted K_S values.

To compute ΔK_S , we used component contrast measurements from our adaptive optics data (Section 4). While all targets considered here had at least one measurement in a filter centered with the K band, none of the response functions used was a close match to 2MASS K_S . Many of the observations were taken with narrow-band K_{cont} ($\lambda_c \simeq 2.27\mu\text{m}$) or $\text{Br}\gamma$ ($\lambda_c \simeq 2.17\mu\text{m}$) filters (to avoid saturation), for example. We transformed these into 2MASS magnitudes before computing the final ΔK_S .

These corrections were usually small ($\lesssim 0.1$ magnitudes), and details on their derivation are given in Appendix A.

After converting all contrast measurements to ΔK_S , we combed multiple measurements using the robust weighted mean. Errors on contrasts for each dataset were taken to be the RMS in flux measurements among consecutive images. These errors may be underestimated because of imperfect PSF modeling, flat-fielding, uncorrected nonlinearities in the detector, as well as intrinsic variability of the star. To test for this, we compared ΔK_X measurements of the same star using the same filter and instrument but on different nights (Figure 3). The comparison suggested a missing error term of 0.016 magnitudes for NIRC2, 0.02 for PUEO and NaCo, and 0.03 for NIRI. We only tested this for K -band filters, but we found consistent values for different K -band filters from the same instrument. We included this term as an additional error term common to all measurements in our computation of ΔK_S .

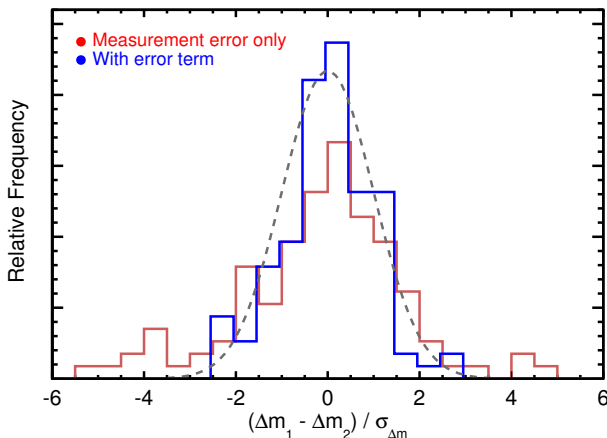


Figure 3. Distribution of contrast ratio differences (in units of standard deviations) for data taken on the same target, and with the same filter and instrument, but in different nights. The red line is before adding the missing error term, while the blue line shows the distribution after adding this. The grey dashed line shows the expected Normal distribution. The histograms are offset slightly for clarity, although identical bins are used as input.

For GJ 2005BC and Gl 900BC, the 2MASS PSF includes flux from the A component. In both cases we use our AO data to measure ΔK between all three components. The total K_S magnitude given in Table 3 already have the A component removed.

7. THE MASS-LUMINOSITY RELATION

7.1. Methodology

For main-sequence stars, the mass-luminosity relation traditionally takes the form:

$$\frac{L_*}{L_\odot} = C \left(\frac{M_*}{M_\odot} \right)^\alpha, \quad (1)$$

where α depends on the dominant energy transport mechanism (e.g., radiative versus convective) and internal structure of the star (Hansen et al. 2004).

We rewrite Equation 1 in terms of M_{K_S} (and $\log(M_*/M_\odot)$) instead of L_* . Absolute magnitudes are more easily measured than overall luminosity, and avoid introducing errors from uncertain bolometric corrections or the need to take flux-calibrated spectra in order to measure the bolometric flux directly. Switching to M_{K_S} also mitigates effects of abundances. The K -band is heavily dominated by metal-insensitive CO and H₂O molecular absorption bands. Optical bands are dominated by much stronger molecular bands (e.g. TiO, CO, CaH, MgH, and VO) that are sensitive to both [Fe/H] and $[\alpha/\text{Fe}]$ (Figure 4, also see Woolf & Wallerstein 2006; Lépine et al. 2007; Mann et al. 2013a).

Our sample encompassed almost an order of magnitude in mass and hence a range of underlying stellar physics. No single power law is expected to fit over the full sequence. Instead, we assumed that α depends on M_{K_S} , which we approximated as a polynomial. This yields a $M_{K_S} - M_*$ relation of the form:

$$\log \left(\frac{M_*}{M_\odot} \right) = \sum_{i=0}^n a_i (M_{K_S} - zp)^i, \quad (2)$$

where a_i are the fit coefficients. The order of the fit (n) was determined using the Akaike Information Criterion (AIC, Akaike 1974). The constant zp is a zero-point (or anchor) magnitude, which we fixed at 7.5. This approximately corresponded to the logarithmic average mass of stars in our sample.

For the left hand side, we computed the total system mass (M_{tot}) for each binary by combining the orbital period (P) and total angular semi-major axis (α) from our fits to the orbital parameters (Section 5) with the parallaxes (π , Section 6.1), following a rewritten form of Kepler's laws:

$$M_{\text{tot}} = M_1 + M_2 = \frac{(\alpha/\pi)^3}{P^2}, \quad (3)$$

where P is in years, α and π are in arcseconds, and M_{tot} is in Solar masses.

Because Equation 3 does not provide component masses, when fitting for the a_i coefficients we performed the comparison between the predicted and dynamical *total* mass for each system. For this, we rewrote Equation 2

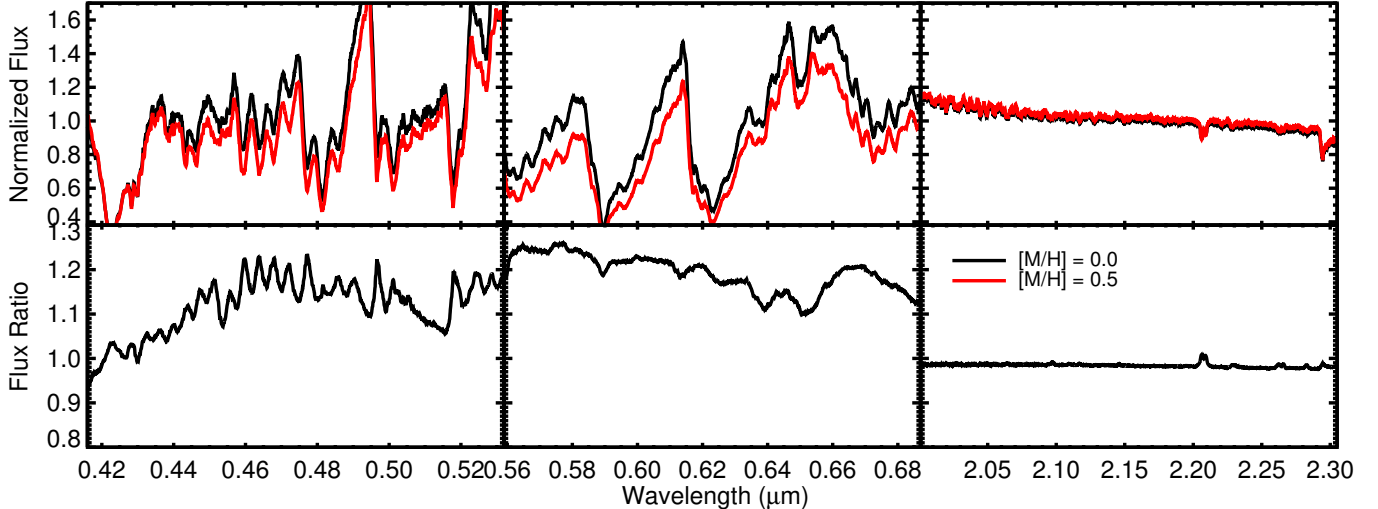


Figure 4. Effect of changes in $[M/H]$ on a model spectrum at $T_{\text{eff}}=3200$ K, $\log(g)=5$ in g - (left), r (middle), and K -band (right). The top panel shows $[M/H]=0$ (black) and $[M/H]=+0.5$ (red) spectra from the CFIST BT-SETTL models (Allard et al. 2012). The bottom panel shows the ratio of the two, highlighting how small an effect $[M/H]$ has in the K -band compared to optical regions. The one feature that stands out in the K -band is the Na doublet, which is a commonly used as a metallicity diagnostic for dwarfs (Rojas-Ayala et al. 2010; Terrien et al. 2012; Newton et al. 2014), and a gravity diagnostic for pre-main-sequence stars (e.g., Schlieder et al. 2012).

in terms of total mass:

$$M_{\text{tot}} = 10^{b_1} + 10^{b_2}, \quad (4)$$

$$b_j = \sum_{i=0}^n a_i (M_{K_S,j} - zp)^i, \quad (5)$$

where $M_{K_S,1}$ and $M_{K_S,2}$ are the primary and companion absolute K -band magnitudes, which were calculated from our measured ΔK_S and unresolved K_S magnitudes (Section 6.3). Equation 4 could easily be modified for higher-order star systems, providing individual M_{K_S} magnitudes and the total mass of the system are known.

We fit for the a_i terms in Equation 4 using the MCMC code `emcee`, which accounts for the strong covariance between coefficients. Each coefficient was allowed to evolve under uniform priors without limits, and was initialized with the best-fit value derived from `MPFIT`. We ran the MCMC chain with 600 walkers for 10^6 steps after a burn-in of 50,000 steps. We ran separate MCMC chains testing values of n (fit order) from three to seven.

Errors on our dynamical masses are correlated to the errors on M_{K_S} . The system mass scales with the cube of the semi-major axis, which depends linearly with the parallax. As a result, the parallax was a major, if not the largest, source of uncertainty on the mass for most systems. Similarly, our K_S magnitudes had relatively small errors (0.01–0.03 mag), so M_{K_S} errors tended to be dominated by the parallax. Because this correlation is usually along (parallel to) the direction of the $M_{K_S}-M_*$ relation,

it can tighten the fit if properly taken into account (when compared to assuming uncorrelated errors).

We wanted the MCMC to explore the full ellipse representing the correlation between M_{K_S} and M_* for each binary. To this end, we treated the distance of each system as a free parameter, letting each evolve under a prior from the observed parallaxes. The MCMC was provided α^3/P^2 and K_S (with uncertainties) for each system, from which total mass and M_{K_S} were recomputed from the parallax at each step in the MCMC. Then we compared the resulting dynamical and $M_{K_S}-M_*$ -predicted masses (the model) within the likelihood function. Thus the MCMC could explore the range of possible parallaxes, allowing both the dynamical (empirical) and model (from Equation 4) to shift in a correlated way due to changes in the (shared) parallax. Since the orbital information provides no direct constraint on the distances, this method effectively forced the MCMC to explore a distribution along the input prior. It was possible for the parallax posterior to move away from the prior if it provided better agreement with the relation as determined by the rest of the sample. However, in practice this did not happen; for all systems the parallax posteriors matched the input values.

For computational efficiency, we assumed Gaussian errors on α^3/P^2 . Although α and P were often correlated and non-Gaussian, posteriors of α^3/P^2 were all well-described by a Gaussian (Figure 5).

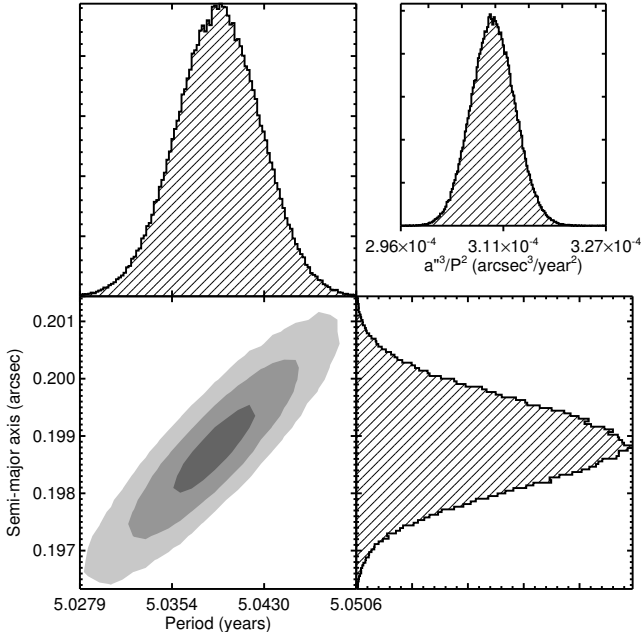


Figure 5. Example joint posterior on semi-major axis and orbital period (bottom left) for the system LHS 6167. Grey regions show 1, 2, and 3σ (from darkest to lightest) of the points. The histograms above and to the right show the one-dimensional distributions of each parameter. The parameter fed into the $M_{K_S} - M_*$ fit is a^3/P^2 (in arcsec 3 per year 2), which we show in the top right inset.

For main-sequence dwarfs at fixed metallicity, more massive stars should always be brighter. Thus we required that the resulting fit have a negative derivative (higher M_{K_S} always gives lower mass) over the full range of input objects considered. We tested running without this constraint, and found similar results over most of the parameter range considered. The major difference was near the edges of the input sample. Without the negative derivative constraint, the fit would often become double valued where there were few points to constrain it.

To handle any variation not included in our formalism, we fit for an additional dimensionless parameter σ_e . σ_e can be interpreted as missing physics (e.g., age, detailed abundances, and/or activity/rotation) driving an intrinsic scatter in the $M_{K_S} - M_*$, or as underestimated uncertainties in our input parallaxes or orbital parameters (and hence the final assigned mass). We implemented σ_e as a fractional uncertainty in the total mass, added to the measurement uncertainty (from the orbit and parallax errors) in quadrature. We also tested including σ_e as an additional uncertainty in the parallax (broadening the priors), or in the assigned K -band

magnitudes. We discuss the differences between these implementations in Section 7.2.

7.2. Results and Uncertainties

We show the resulting posteriors for the polynomial coefficients (a_i) in Figure 6. The spread in the posteriors for individual coefficients is large, suggesting significant errors on each coefficient. However, the coefficients are also highly correlated; for a given value assigned to four of the five fit coefficients, there is a relatively narrow set of solutions for the final constant. The final fit was tightly constrained over the full sequence, which we show in Figure 7 for individual masses, and combined masses in Figure 8 (a more realistic representation of how the fit was done).

Coefficients for powers of the same parity (even or odd) were strongly correlated to each other. This was expected, as a decrease in the slope (from linear) is best explained using an odd power, and increases with an even power. Coefficients for powers with even parity (with the exception of the a_0 term) were also generally centered around zero. This also was expected in the context of the shape of the relation seen in Figure 7, and our requirement that the mass always decrease with decreasing luminosity (increasing M_{K_S}). A power with even parity will prefer to turn upwards at low masses. We explored this further by redoing the fit with no even powers (except a_0 was retained), but exploring higher-order odd powers. The resulting fit was significantly worse, with a σ_e value twice as large compared fits with the same number of free parameters, but including even powers. The resulting fits also showed significant systematic deviations from the empirical data for $0.3M_\odot < M_* < 0.5M_\odot$. We opted to include the even orders for all analyses despite their near-zero values.

We adopted $n = 5$ as the preferred solution based both on the AIC values and visual inspection of the residuals. Lower-order fits did a reasonable job fitting most of the sequence, but poorly reproduced the masses of objects with $M_* < 0.085M_\odot$. In this regime, the relation becomes increasingly non-linear. The result is that lower-order fits systematically overestimate the masses of the coolest objects in our sample (Figure 9) and tend to overestimate σ_e to compensate. Higher-order fits explain the data reasonably well, but were not justified statistically (e.g., marginal decrease in σ_e) and showed slope changes outside the calibration sample that are not expected by theoretical considerations.

The three different implementations of σ_e were broadly consistent with each other. For example, applying it as broadening on the parallax prior yielded an extra error $\gtrsim 1/3$ that of implementing it on the final mass. Since

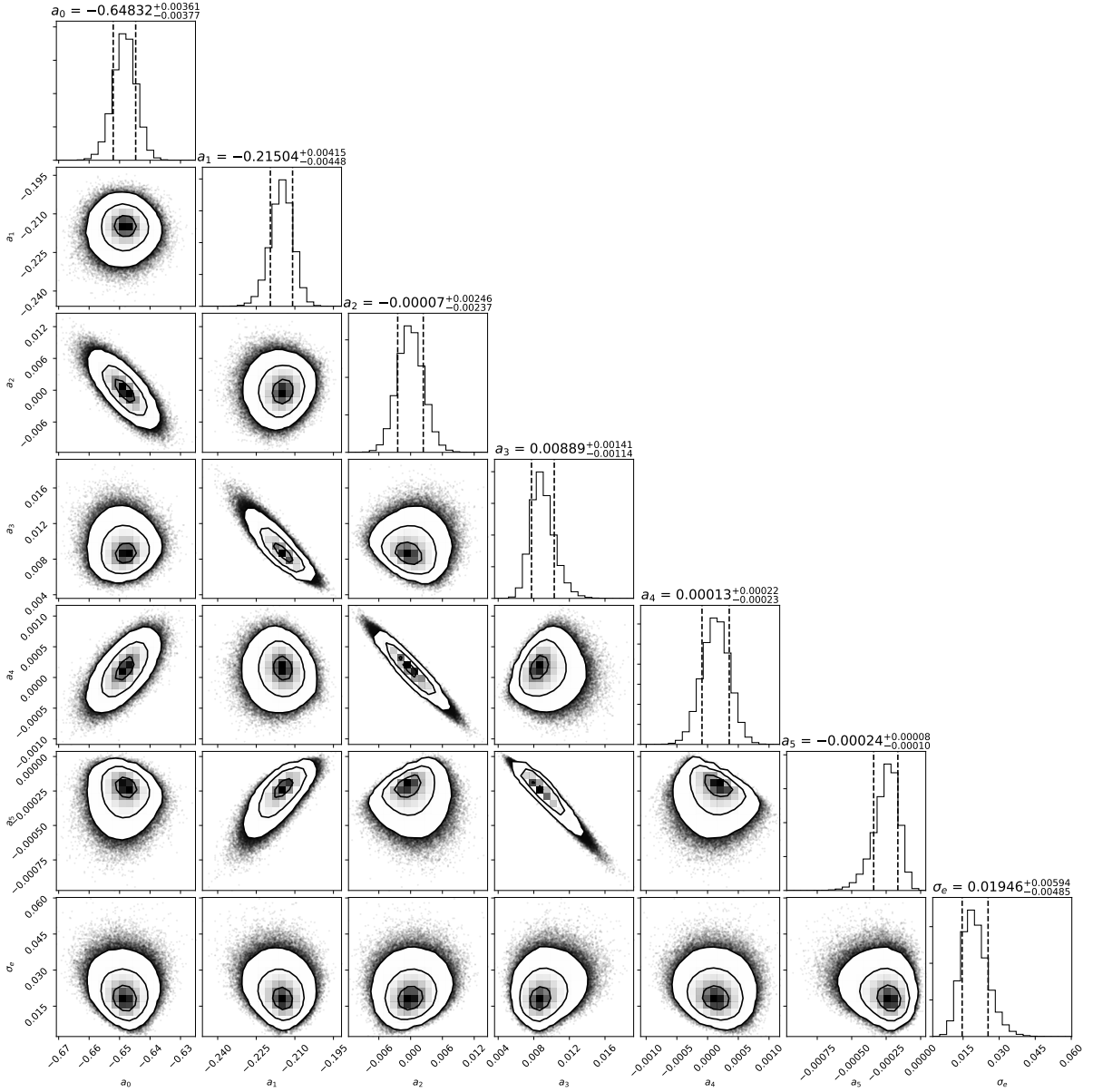


Figure 6. Posterior projections for the a_i values derived from our MCMC fit to Equation 4 as well as the additional error term σ_e . Contours denote the 1, 2, and 3 σ confidence intervals, and the dashed lines in the histogram mark 1 σ . The σ_e parameter represents the fractional error in the total mass, added to account for intrinsic variation in the relation or underestimated uncertainties in the input masses. Figure was generated using `corner.py` (Foreman-Mackey 2016).

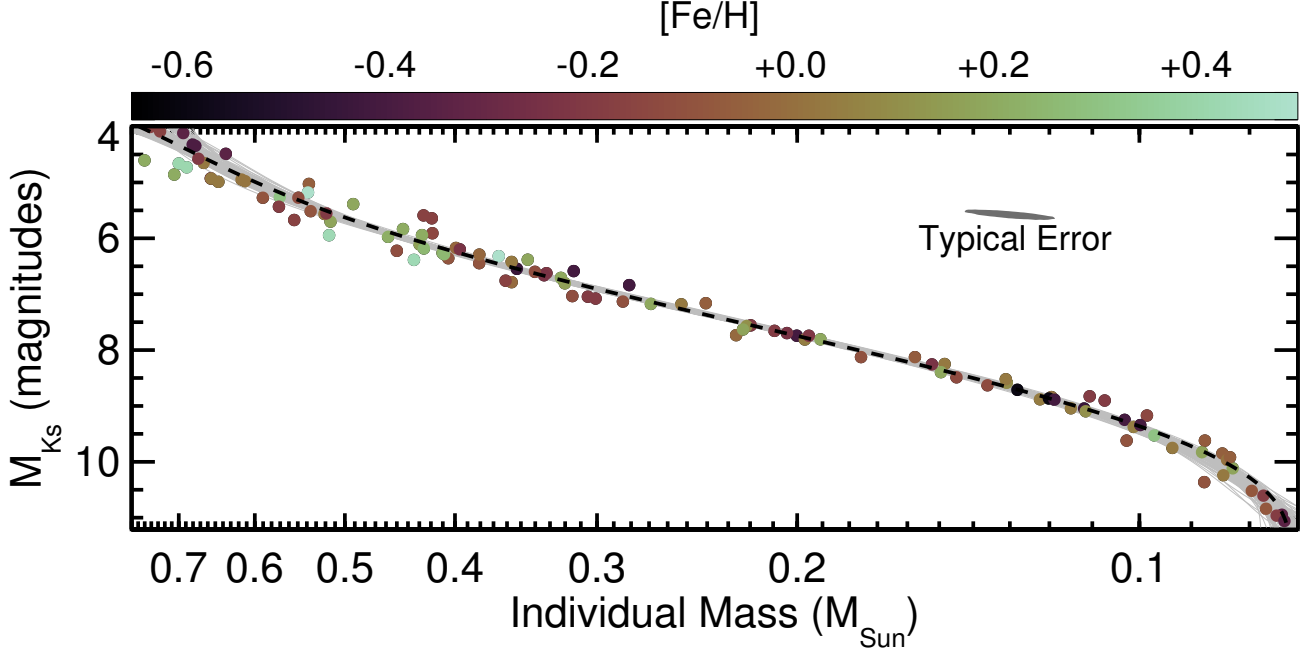


Figure 7. Absolute K_S -band magnitude as a function of mass for targets in our sample (circles). Points are color-coded by their estimated metallicity. We show a typical error ellipse in grey to highlight that errors on mass and M_{K_S} measurements are correlated, and usually parallel to the $M_*-M_{K_S}$ relation (both depend on the common parallax). The black dashed line indicates the best-fit (highest likelihood) from our MCMC analysis. To provide an estimate of the scatter in the relation as a function of mass, we show 100 randomly selected fits from the MCMC chain in grey. Note that our orbit fits only provide *total* mass; we used the mass ratios derived from the best-fit $M_{K_S}-M_*$ relation for the purposes of this figure. Figure 8 shows the total mass comparison, which is more reflective of how the comparison is done.

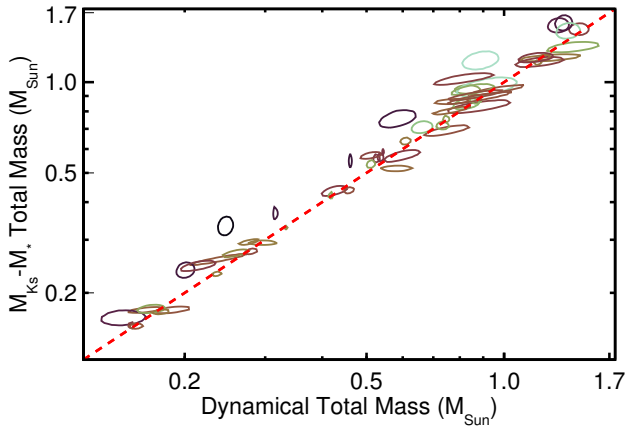


Figure 8. Predicted total (system) M_* from the $M_{K_S}-M_*$ relation as a function of the total mass determined from the orbit fit. Ellipses represent $\approx 1\sigma$ distribution of values for each point, accounting for parallax errors common to both the predicted and dynamical mass, but not accounting for scatter in the final $M_{K_S}-M_*$ relation (σ_e). Color-coding by $[\text{Fe}/\text{H}]$ matches that of Figure 7.

the parallax term is cubed in the total mass calculation

(Equation 3) these are functionally equivalent (although parameter correlation forces a slightly larger error in the parallax). However, we found that implementing σ_e as an error on the total mass best explained the data. Taking σ_e as an error on the K -band magnitude led to a χ^2_ν value too low when just considering stars below $0.25M_\odot$, and too high for stars above $0.5M_\odot$, while applying χ^2_ν as an error on the total mass yielded χ^2_ν closer to one over the whole mass range. Taking σ_e as an error on M_* is also easily implemented when applying the relation.

We list the best-fit (highest likelihood) coefficient values in Table 1, as well as the median value of σ_e . We also provide trimmed posteriors for each coefficient in the [github repository](#). Fits using $n = 4$ and $n = 6$ are included in Table 1 for reference, although we suggest using only the $n = 5$ relation.

To estimate the uncertainty in the relation we computed the standard deviation in the derived masses for a fixed M_{K_S} across all MCMC steps, which we report in Table 2. In the best-constrained regions ($5 \lesssim M_{K_S} \lesssim 7$, $0.3 \lesssim M_* \lesssim 0.6$) the scatter in the relation is $\lesssim 1\%$, reaching $\approx 3\%$ near the edges. These values in Table 2 could potentially be used as a reference for estimating errors on the output mass for a given M_{K_S} if combined

Table 1. Best-fit Coefficients for Equations 4 and 6

n	a_0	a_1	a_2	a_3	a_4	a_5	a_6	f	σ_e
4	-0.65074	-0.20234	3.6638×10^{-3}	5.0407×10^{-3}	-2.6018×10^{-4}	0.024
5	-0.64661	-0.21246	-2.6534×10^{-3}	7.9485×10^{-3}	3.6899×10^{-4}	-1.9226×10^{-4}	0.019
6	-0.63910	-0.20981	-1.2332×10^{-2}	6.8080×10^{-3}	2.5023×10^{-3}	-1.0325×10^{-4}	-1.2146×10^{-4}	...	0.018
4	-0.65123	-0.20169	4.7567×10^{-3}	4.9324×10^{-3}	-2.9132×10^{-4}	0.0360	0.024
5	-0.64177	-0.21493	-5.5294×10^{-3}	8.9387×10^{-3}	6.3228×10^{-4}	-2.7022×10^{-4}	...	0.0380	0.018
6	-0.64145	-0.21410	-8.4574×10^{-3}	7.7961×10^{-3}	1.5020×10^{-3}	-1.5918×10^{-4}	-5.3935×10^{-5}	0.0307	0.018

NOTE—The $n = 5$ fit is preferred independent of including [Fe/H]. Note that values presented here are the highest likelihood for the a_i values, with the median value for f and σ_e . Figures 6 and 12 note the median coefficient values.

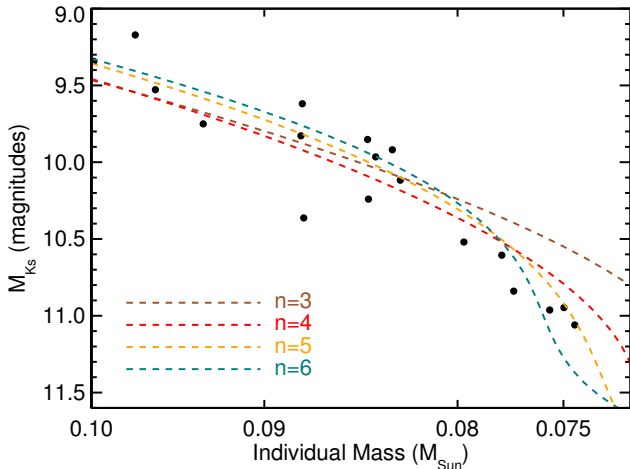


Figure 9. Fits of varying order (n) to Equation 4 compared to the empirical values for the lowest-mass stars in our sample. The fits are similar above $0.085 M_{\odot}$, but a high-order ($n = 5$) is required to reproduce objects below this as the relation becomes increasing non-linear. The systematic offset seen between the low-mass sample and the best-fit relation can be seen in the coefficient posteriors as well as the best-fit relation (i.e., the distribution of fits are systematically high).

with errors from the distance and K_S magnitude. However, this does not account for intrinsic scatter in the $M_{K_S}-M_*$ relation.

For all fits, σ_e was inconsistent with zero, suggesting a fundamental limit to our M_* determinations. To this end, we performed the same uncertainty calculation using the fit posteriors, but also included σ_e as a proxy of any intrinsic scatter in the relation. It is possible that σ_e is purely a representation of missing uncertainties in the input parameters (K_S , π , or α^3/P^2 values). However, even in this case, we cannot rule out the presence of intrinsic variation at the level of σ_e without removing (or at least characterizing) the missing errors captured

within σ_e . We advise using the errors that include σ_e for all mass uncertainty estimates.

A more robust account of errors than using Table 2 would be to use the full coefficient posteriors to account for asymmetry around the best-fit relation (i.e., by sampling a range of possible a_i values). To aid with this, we included the fit posteriors and a simple code that provides output M_* posteriors given a K_S , distance, and associated uncertainties. The program combines the scatter in the coefficients with the median value of σ_e to produce a realistic M_* posterior (including asymmetry).

Over most of the relation, particularly $0.1 M_{\odot} < M_* < 0.5 M_{\odot}$, σ_e is the dominant source of uncertainty in estimating masses, and hence future studies aiming to improve on our relation will need to understand the origin of this extra uncertainty.

7.3. The role of metallicity

We explored the effects of [Fe/H] on the $M_{K_S}-M_*$ relation using the Mesa Isochrones and Stellar Tracks (MIST, Dotter 2016; Choi et al. 2016) and an updated version of the Dartmouth Stellar Evolution Database (DSEP, Dotter et al. 2008). The updates to DSEP have been previously detailed in Feiden & Chaboyer (2013, 2014a), and Muirhead et al. (2014), with additional information on the updates for low-mass stars in Mann et al. (2015). MIST models use ATLAS/SYNTHE model atmospheres (Castelli & Kurucz 2004) with updated TiO opacities for late-type stars that should improve performance. DSEP uses PHOENIX Hauschildt et al. (1999a,b) models, and have been used widely for studies of late-type dwarfs (e.g., Boyajian et al. 2012; Bell et al. 2015; Kesseli et al. 2018). While other model grids (e.g., YaPSI, PARSEC, Lyon Spada et al. 2013; Chen et al. 2014; Baraffe et al. 2015) show similar agreement with empirical studies of low-mass stars, we leave a more detailed comparison between the full range of model grids and our empirical

Table 2. Error in M_{K_S} – M_* Relation

M_{K_S} (mag)	M_* M_\odot	SpT ^a	$\sigma_{M_*}^b$	$\sigma_{M_*}^b$ %	$\sigma_{M_*}^c$	$\sigma_{M_*}^c$ %
No [Fe/H] term ($f = 0$), 5th order						
4.0	0.742	K4.5	0.028	0.038	0.031	0.042
4.5	0.669	K7.0	0.011	0.017	0.017	0.026
5.0	0.6004	M0.0	0.0091	0.015	0.015	0.025
5.5	0.5248	M1.5	0.0067	0.013	0.012	0.023
6.0	0.4430	M2.5	0.0046	0.010	0.0098	0.022
6.5	0.3615	M3.0	0.0034	0.010	0.0078	0.022
7.0	0.2871	M3.5	0.0026	0.009	0.0062	0.021
8.0	0.1759	M4.5	0.0016	0.009	0.0038	0.021
8.5	0.1398	M5.0	0.0014	0.010	0.0031	0.022
9.0	0.1143	M6.0	0.0013	0.011	0.0026	0.022
9.5	0.0971	M6.5	0.0012	0.013	0.0023	0.023
10.0	0.0860	M7.5	0.0013	0.015	0.0021	0.025
10.5	0.0791	M9.0	0.0013	0.016	0.0020	0.025
11.0	0.0745	L1.0	0.0019	0.025	0.0024	0.032
[Fe/H] term (f), 5th order						
4.0	0.753	K4.5	0.029	0.039	0.032	0.043
4.5	0.671	K7.0	0.011	0.016	0.017	0.025
5.0	0.5990	M0.0	0.0091	0.015	0.014	0.024
5.5	0.5231	M1.5	0.0067	0.013	0.012	0.022
6.0	0.4423	M2.5	0.0045	0.010	0.0093	0.021
6.5	0.3618	M3.0	0.0035	0.010	0.0075	0.021
7.0	0.2880	M3.5	0.0027	0.009	0.0059	0.021
8.0	0.1769	M4.5	0.0016	0.009	0.0036	0.021
8.5	0.1405	M5.0	0.0015	0.010	0.0030	0.021
9.0	0.1147	M6.0	0.0013	0.011	0.0025	0.022
9.5	0.0974	M6.5	0.0013	0.013	0.0022	0.022
10.0	0.0862	M7.5	0.0013	0.015	0.0020	0.024
10.5	0.0794	M9.0	0.0013	0.016	0.0020	0.025
11.0	0.0750	L1.0	0.0018	0.024	0.0023	0.030

NOTE—This table assumes M_{K_S} (and [Fe/H]) are known perfectly. Total errors on M_* should take into account errors in the measured parameters and the relation.

^aSpectral types are given for reference, but are extremely rough because of a significant dependence on metallicity and how the spectral typing is done (e.g., which indices are used, NIR versus optical). It is not recommended to use this table as a means to compute M_{K_S} or M_* from a spectral type or vice versa.

^bThe uncertainty in the resulting M_* at a given M_{K_S} ignoring σ_e

^cThe uncertainty in the resulting M_* at a given M_{K_S} accounting for σ_e

masses for future analysis, and we restrict our model comparison here to just effects from metallicity.

We show the expected M_{K_S} tracks from MIST and DSEP for $-0.5 < \text{[Fe/H]} < +0.3$ in Figure 10 alongside our empirical determinations. MIST models do not extend below $0.1M_\odot$, while DSEP goes down to $0.085M_\odot$, so we comparisons are restricted to that mass range. For this comparison we assumed a fixed age of 5 Gyr, although the choice of age from 1–10 Gyr makes a negligible difference for the mass range shown (Figure 1).

Note that metal-rich stars are expected to be *less luminous* for a fixed M_* , whereas the opposite trend is seen for a fixed T_{eff} and most color selections. Higher metal abundance increases the opacity, causing the stellar radius to increase at a fixed M_* and surface temperature to decrease. Decreasing surface temperature also decreases the core temperature because it shifts the star to a different adiabat, which reduces nuclear reaction rates and overall luminosity. The trend is weaker (or even reversed) in K -band, because although the overall luminosity is lower at higher [Fe/H], most of the increases in opacity are the optical, causing a larger fraction of the total luminosity to escape at NIR wavelengths. This difference as a function of wavelength can be seen in Figure 4, where the metal-rich spectrum sits below the solar-metallicity one at optical wavelengths, but above it in the NIR. The MIST and DSEP models likely have some difference in their treatment of one or both of these competing effects, as the DSEP models show a reduced impact of [Fe/H] on the M_{K_S} – M_* relation as with decreasing stellar mass (likely because of increasing opacity in the optical with decreasing surface temperature), while MIST models show a similarly large impact over the full mass range considered here.

Based on our dynamical masses, there is a slight trend for metal-rich stars above $0.4M_\odot$ to land below the median sequence, as expected from both model grids. However, many metal-poor stars also land below the sequence, and there is no obvious trend below $0.4M_\odot$. Further, the largest metal-rich outlier in the high-mass region (G1 99) had a relatively poor mass determination (13%), and is consistent with the solar-metallicity sequence.

The residuals from our best-fit indicate a weak (or no) effect on the derived M_* due to changes in [Fe/H], as we show in Figure 11. A Spearman’s rank test yielded no significant correlation between the residuals and [Fe/H]. We tried resampling the measurements using their uncertainties, and $< 1\%$ of samples showed a significant correlation. We also repeated this test, but restricted to just the best-characterized systems (< 5% precision on mass) and still found no significant trend with [Fe/H].

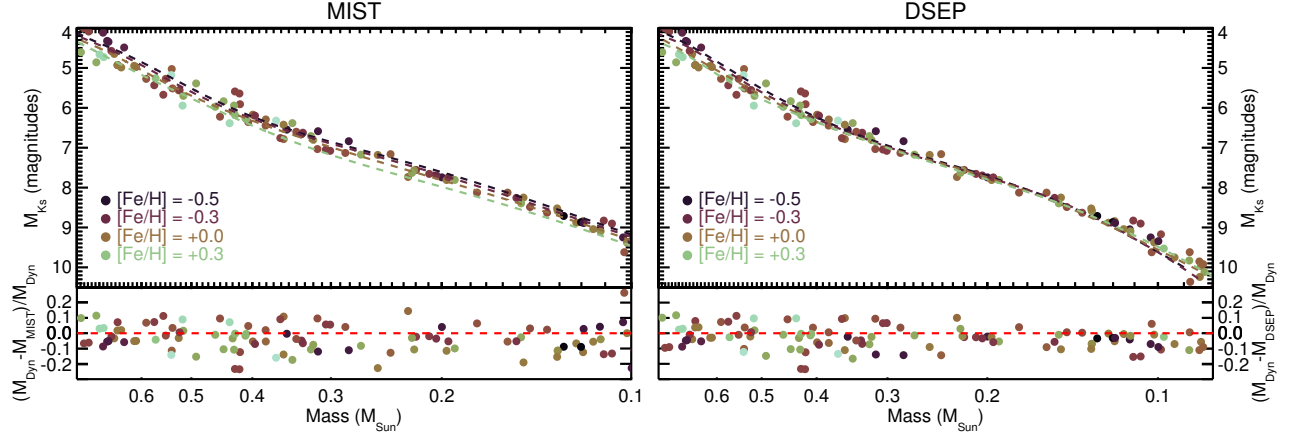


Figure 10. M_{K_S} as a function of M_* using MIST (left) and DSEP (right) tracks of different metallicities (dashed lines) compared to empirical mass determinations (points). Color-coding by metallicity is the same for the points and lines, and matches the color scale of Figure 7. Due to the limits of the model grids, the plots cut at $0.1 M_\odot$ and 0.085 for MIST and DSEP, respectively. The bottom panel shows the fractional residual between the model and empirical determinations. This model masses for the residuals were estimated by interpolating over the model grid using the $[Fe/H]$ and M_{K_S} for a given target.

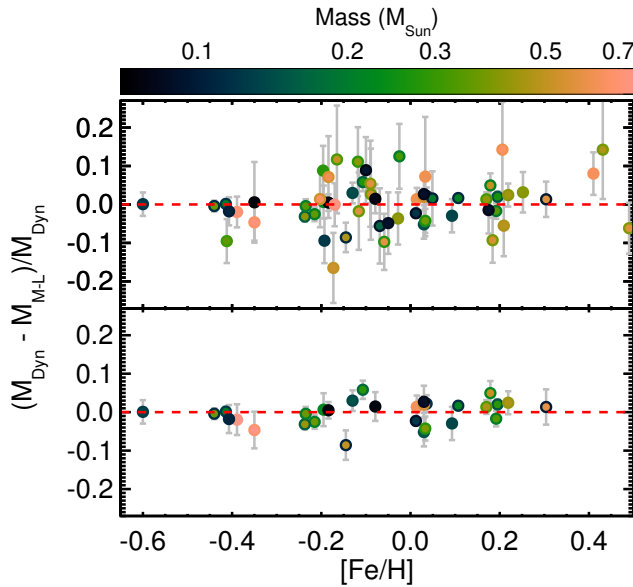


Figure 11. Fractional difference between the orbital and predicted system mass as a function of metallicity of the system. The top panel contains all systems, while the bottom shows just those with $<5\%$ uncertainties on M_* . Points are color-coded by the masses of components, with the inner dot corresponding to the primary star's estimated mass, and the outer circle the companion's estimated mass. Errors consider only input errors on total M_* .

Our sample is limited in its $[Fe/H]$ range; 64% of the targets are $-0.2 < [Fe/H] < +0.2$ and only one target has $[Fe/H] < -0.5$. It is possible that our best-fit relation

masked any $[Fe/H]$ term by shifting the fit to match the typical metallicity of stars at a given M_{K_S} . We explored $[Fe/H]$ effects in a more robust way by fitting for a term of the form:

$$M_{tot} = (1 + f[Fe/H]) \times (10^{b_1} + 10^{b_2}), \quad (6)$$

where b_j is defined in Equation 5. This form assumes that a linear change in $[Fe/H]$ corresponds to a fractional change in M_* (e.g., $f=0.1$ would correspond to a 10% change in derived M_* per dex change in $[Fe/H]$ at a fixed M_{K_S}). This is generally consistent with the models over the metallicity range considered here (although it is predicted to become increasing non-linear for $[FeH] < -0.5$). Equation 6 also assumes a single f over the whole mass range considered. While this is consistent with the predictions of MIST models, DSEP models show a tightening with decreasing mass (increasing M_{K_S}). However, our sample is too small and errors on $[Fe/H]$ too large to justify adding a term that depends on both $[Fe/H]$ and M_{K_S} . We leave higher-order tests for a future investigation with a broader range of metallicities.

For the metallicity analysis, we excluded the two L dwarfs from the sample because their metallicities are less reliable (extrapolated from an M dwarf calibration). As with our fit to Equation 4, we tested a range of values for n (number of a_i coefficients). Both targets also have masses below the limits of the model grids. Our MCMC fitting method was otherwise identical to that outlined in Section 7.

We show the output coefficient posteriors including f in Figure 12. We list the corresponding best-fit coefficients in Table 1 along with the median values of σ_e and f . As

with our fits neglecting any [Fe/H] terms, we found significantly better agreement with the lowest-mass objects in the sample using $n = 5$, although $n = 4$ and $n = 6$ are listed in Table 1 for reference.

In agreement with our previous analyses, our derived f value is consistent with zero (no impact of [Fe/H] on the M_{K_S} – M_* relation) at 1.7σ . This suggests our relation will work reasonably well even on more extreme metallicity samples. However, it is also possible that [Fe/H] is less important than abundances of elements that specifically impact the strength of molecular features in M dwarf spectra. Higher C/O, for example, suppresses available Oxygen for TiO formation, weakling a major source of opacity in the optical (e.g., C, O, Ti, Fortney 2012; Gaidos 2015; Veyette et al. 2016). This also might explain some of the extra scatter in the relation (σ_e) if there is sufficient variance of these abundances in the given sample. Testing this will require a means to determine more detailed abundances of M dwarfs (e.g., Veyette et al. 2017), and/or to add in subdwarf binaries or other systems with more extreme abundances to provide increased leverage on any metallicity effects.

To compare to the models, we fit the MIST and DSEP grid points in the same manner as the empirical dataset following Equation 6. Our binary sample is not uniformly spaced in [Fe/H] and M_{K_S} , so to ensure a fair comparison, we resample the model grid to match the binary sample. For every target we generate a model-predicted mass at fixed age (5 Gyr), and alpha abundance (Solar) by linearly interpolating over M_{K_S} and [Fe/H] (using the assigned values for that target). We use the resulting (model-based) masses with the input M_{K_S} and [Fe/H] values to fit for a model f value that can be compared to our empirical determination.

In Figure 13 we show the posterior on f from the model grids compared to that from the dynamical masses. MIST models predict a larger [Fe/H] effect than suggested by our binary sample, while DSEP predictions are quite consistent with our own. The difference between the two posteriors ($f_{\text{model}} - f_{\text{dynamical}}$) is inconsistent with zero at 4.1σ for MIST, while for DSEP the difference is $\lesssim 1\sigma$.

The discrepancy between MIST model masses and dynamical masses cannot be explained by σ_e . Whatever interpretation we apply to σ_e , it only amounts to a $\lesssim 2\%$ variation in M_* for a given M_{K_S} . The MIST models predict a metallicity effect of $\simeq 0.17$ per dex, and since our sample covers about 1 dex in [Fe/H], this translates to an expected $\simeq 17\%$ variation in mass over the full sample, or 8% if we just consider the majority of the targets. It is possible that σ_e is being driven in part by erroneous assigned [Fe/H] (or underestimated errors on

[Fe/H]) which could decrease our derived f value, but the effect is too small to reconcile with the MIST models.

The discrepancy between MIST and empirical estimates of the impact of [Fe/H] could be due to missing opacity/molecular lines in the atmospheric models. Recent comparison suggest atmospheric models reproduce optical and NIR spectra of M dwarfs to $\simeq 5\%$ (e.g., Lépine et al. 2013; Mann et al. 2013b), with the exception of a few molecular features like CaOH, AlH, and NaH (Rajpurohit et al. 2013). However, these tests have not been performed on the atmospheric models used for MIST isochrones. Missing opacity at optical wavelengths would strengthen the effect of [Fe/H] by underestimating the number of saturated features; if a line is saturated adding [Fe/H] cannot make it stronger, which serves to reduce the impact of [Fe/H]. The effect at NIR wavelengths would be weaker, since there are fewer molecular bands, but underestimated opacity in the optical shifts continuum levels in the NIR (and how those levels change with [Fe/H]). A problem with the input opacities is also consistent with the trend of growing discrepancy at the lowest masses, where molecular bands become increasingly important, and might explain the difference between MIST and DSEP predictions (as they use different atmosphere boundary conditions).

7.4. Comparison to previous relations

7.4.1. Delfosse et al. (2000)

Delfosse et al. (2000) provided one of the most commonly used M_{K_S} – M_* relations, covering $0.1M_\odot < M_* < 0.6M_\odot$. Like our work, the calibration was built primarily on astrometric binaries. Delfosse et al. (2000) used a mix of individual (targets with radial velocities and/or absolute astrometry) and total masses, with the latter case converted to individual masses using models available at the time. Nearly all the targets in Delfosse et al. (2000) were included in our sample, with the exception of triple systems and eclipsing binaries, both of which we avoided because of the complexity of computing total masses in the first scenario and estimating M_{K_S} in the latter. Because of the sample overlap, consistency is expected. However, a comparison can be useful to see how past use of Delfosse et al. (2000) may change with our more precise results.

We show the comparison in Figure 14, including the points used in the Delfosse et al. (2000) calibration as well as the two fit lines. Given errors often quoted for the Delfosse et al. (2000) relation (5–10%), the two fits are in remarkable ($< 5\%$) agreement over most of the mass range ($0.15M_\odot \lesssim M_* \lesssim 0.5M_\odot$). Only at the high-mass end do the two relations diverge by as much as 10%, but Delfosse et al. (2000) had few calibrators in this regime.

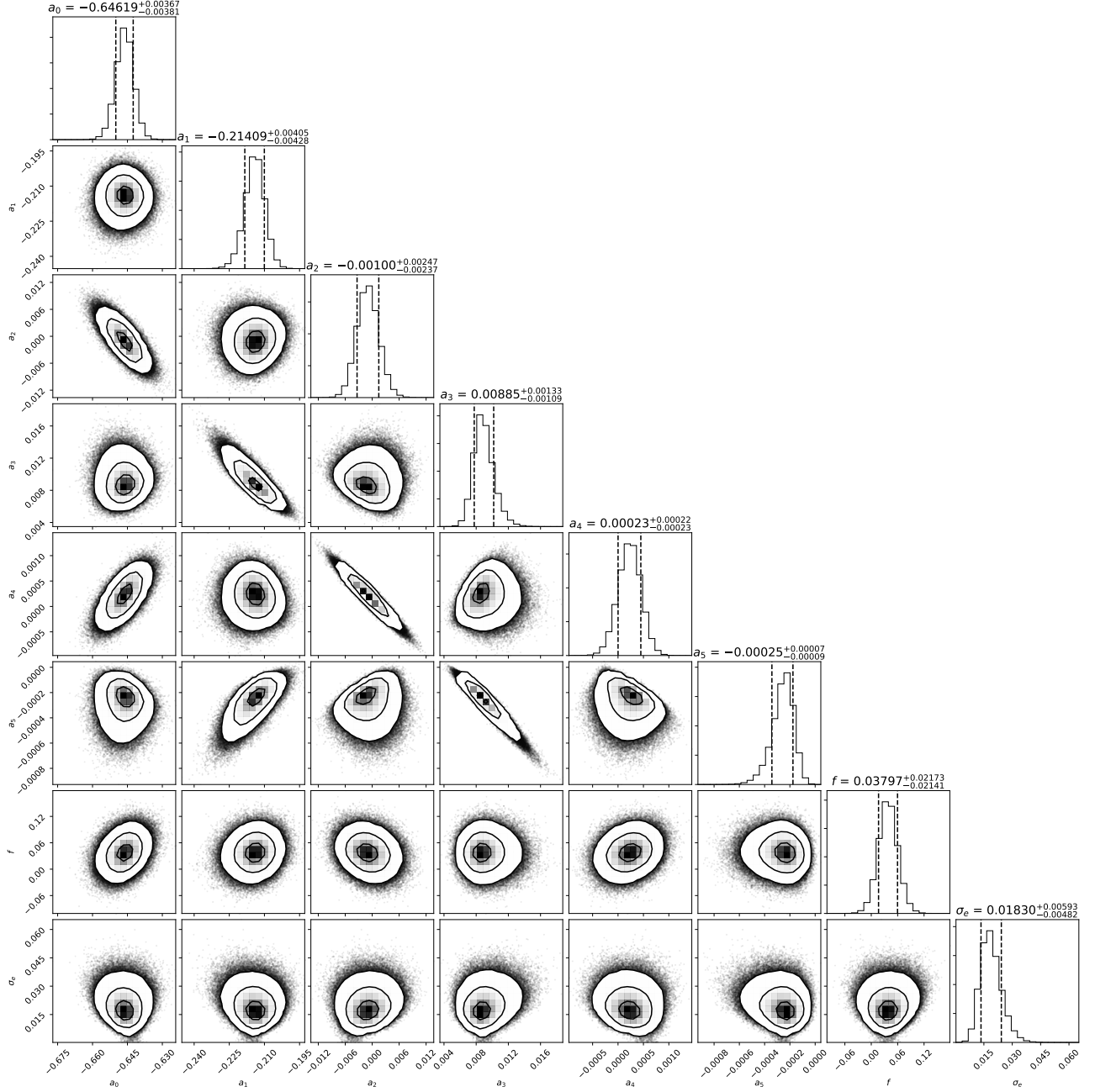


Figure 12. Same as Figure 6, but for the fit following Equation 6, i.e., including the [Fe/H] term, f .

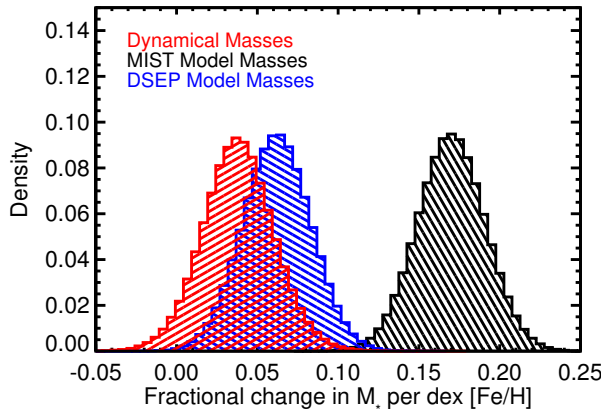


Figure 13. Comparison of the posterior on f (fractional change in M_* per dex in metallicity for a fixed M_{K_S} ; Equation 6) predicted by the MIST models (black) compared to that using our dynamical masses (red). There are an identical number of points in each posterior and the bin sizes are the same.

While the two relations are in excellent agreement, the relation presented here is a factor of 3-5 \times more precise over the whole mass regime.

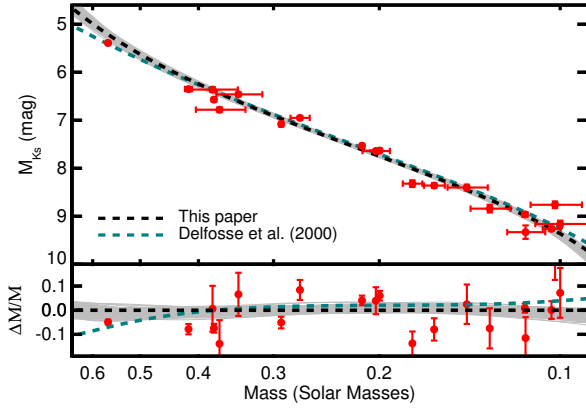


Figure 14. Absolute K_S -band magnitude as a function of mass for astrometric binaries analyzed by Delfosse et al. (2000) (red circles). The resulting $M_*-M_{K_S}$ relation from Delfosse et al. (2000) is shown as a teal dashed line, while the best-fit relation from this paper is shown as a blacked dashed line (with error in grey as in Figure 7). The bottom panel shows the residual of the Delfosse et al. (2000) points compared to our relation.

7.4.2. Mann et al. (2015)

Mann et al. (2015) built a catalog of 183 M dwarfs with precise T_{eff} and R_* , calibrated against radii measure-

ments from long-baseline optical interferometry (Boyajian et al. 2012) and precision bolometric fluxes (e.g., Mann & von Braun 2015; Boyajian et al. 2015). Masses were computed for these stars by interpolating the parameters onto an updated version of the DSEP models as described in Feiden & Chaboyer (2013, 2014b) and Muirhead et al. (2014). Although these masses were model-dependent, they accurately reproduced the mass-radius relation from low-mass eclipsing binaries. This suggested that the model-based masses were accurate to $\simeq 3\%$ or better, and motivated the development of a $M_{K_S}-M_*$ relation from the Mann et al. (2015) sample. A comparison to our relation can be seen in part as a test on the updated DSEP models, in addition to the results given in Mann et al. (2015).

We show our fit with uncertainties alongside Mann et al. (2015)'s in Figure 15. The two fits track each other extremely well, with a maximum divergence of $\simeq 5\%$. Given the quoted 2-3% uncertainties from Mann et al. (2015) and similar errors in our relation, this difference is not significant. There is a hint of tension at above $0.6M_\odot$ and around 0.2 - $0.3M_\odot$ where the difference is the largest, but the difference is never statistically significant.

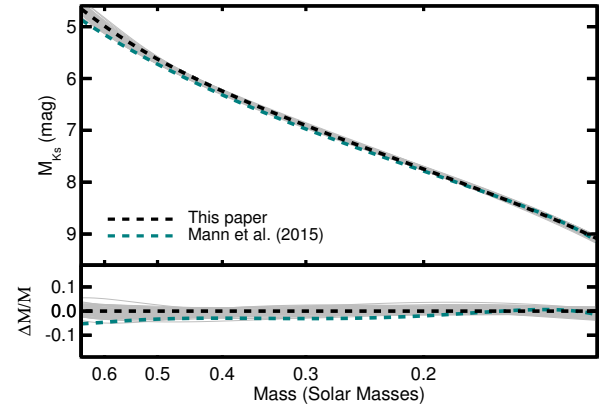


Figure 15. Comparison of $M_*-M_{K_S}$ from Mann et al. (2015), shown as a teal dashed line, to that from this paper, which is shown in black, with 100 randomly selected realizations of the MCMC (as with Figures 7 and 14). Residual is shown in the bottom panel. Individual points from Mann et al. (2015) on which the calibration is based are not shown (for clarity), but they follow a tight sequence around the teal line. Only the range of masses covered by Mann et al. (2015) are shown.

7.4.3. Benedict et al. (2016)

Like our work, the Benedict et al. (2016) relation was also based primarily on masses derived from M dwarf astrometric binaries. The Benedict et al. (2016) sam-

ple uses absolute astrometry from *HST* fine guidance sensors and radial velocities for a subset of systems. In addition to the precision provided by *HST*, this combination yields individual (component) masses, and, in many cases, independent constraints on parallaxes. So although our sample is larger and contains most of the targets in Benedict et al. (2016), their analysis is not subject to some of the complications of our own.

We compare our M_{K_S} – M_* relation Benedict et al. (2016)’s in Figure 16. The two relations are in excellent agreement for $0.09M_\odot \lesssim M_* \lesssim 0.25M_\odot$. Below this regime, the Benedict et al. (2016) fit is effectively anchored by one star, GJ1245C, because the two other stars in this low-mass regime (GJ 2005B and C) have relatively large errors. GJ1245AC is in our sample, but we use a parallax from Lindegren et al. (2018) on GJ 1245B for this system, which places it 10σ (2.5%) more distant than the parallax adopted by Benedict et al. (2016). Our orbital parameters for this system are in excellent agreement with Benedict et al. (2016) if we adopt their distance, but the Lindegren et al. (2018) parallax makes the final parameters more consistent with our M_{K_S} – M_* relation than when adopting the Benedict et al. (2016) parallax. Since the Benedict et al. (2016) distance accounted for the binarity of this system, the origin of the difference between these two parallaxes is unclear. If GJ 1245B is itself an unresolved binary, this could explain the discrepant parallax (although there is no evidence of this). If the Benedict et al. (2016) parallax is correct, this reduces the total mass to $0.189 \pm 0.001M_\odot$, while the predicted mass is $0.207M_\odot$ for the adjusted M_K values (8.90 and 10.02 for the primary and companion, respectively). To reconcile the dynamical and predicted mass using the Benedict et al. (2016) parallax, we would need to explain why GJ 1245AC is $\simeq 0.3$ mag more luminous than predicted by other similar-mass objects, such as youth (Lurie et al. 2015; Newton et al. 2017).

Above $0.3M_\odot$, Benedict et al. (2016) predicts masses as much as 10% higher than our own for a fixed M_{K_S} . Our fit agrees reasonably well with the astrometric binaries fit by Benedict et al. (2016) in this mass regime. The divergence is driven instead by literature mass determinations that Benedict et al. (2016) included in their M_{K_S} – M_* fit. Inspection of these literature points makes the origin of the discrepancy more clear: many are eclipsing binaries and have ΔK -band magnitudes of mixed quality and/or lack parallaxes needed for a precise M_{K_S} . GU Boo, for example, has absolute magnitudes estimated from an optical eclipse depth combined with bolometric corrections (López-Morales & Ribas 2005), which are drawn from models that perform poorly on M dwarfs (Lejeune et al. 1998; Hauschildt et al. 1999a). Similarly, for GJ

2069 AC (CU Cnc) Benedict et al. (2016) adopted M_{K_S} from Ribas (2003) that disagrees with the 2MASS K_S and Gaia DR2 parallax (for either AC or B) using any ΔK_S . We conclude that the M_{K_S} determinations for these eclipsing systems need to be revised before including them in future analyses of the M_{K_S} – M_* relation.

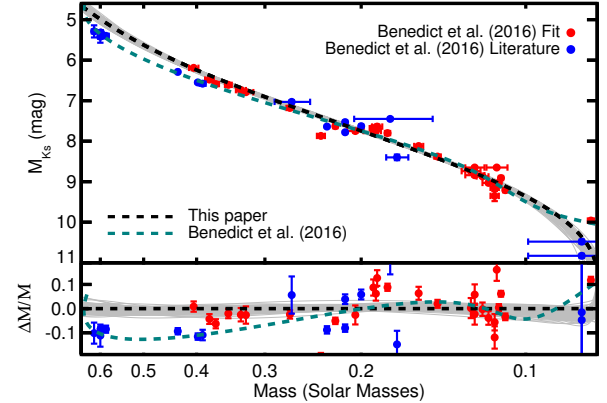


Figure 16. Absolute K_S -band magnitude as a function of M_* for astrometric binaries analyzed by Benedict et al. (2016) (red circles) and those used in the Benedict et al. (2016) relation, but pulled from the literature (blue circles). The resulting M_* – M_{K_S} relation from Benedict et al. (2016) is shown as a teal dashed line, while the best-fit relation from this paper is as a black dashed line (with random samplings in grey as in earlier figures). The bottom panel shows the residual of the Benedict et al. (2016) points compared to our relation, with the Benedict et al. (2016) relation in teal for reference. Errors in the residuals only reflect errors in M_* and M_{K_S} , and do not account for errors in our M_* – M_{K_S} relation.

8. CONCLUSIONS & DISCUSSION

8.1. Summary

The mass-luminosity relation has proven to be a critical tool for estimating masses of cool stars for decades, and has broad applications ranging from characterizing extrasolar planets to measuring the initial mass function in massive galaxies. The M_{K_S} – M_* relation has been particularly useful because K -band magnitudes are widely available through 2MASS and other sources, extinction is usually negligible for nearby stars at these wavelengths, many adaptive optics systems perform well (better Strehl) at K -band, and the impact of metallicity on the mass-luminosity relation is smaller in K than at optical wavelengths. With the arrival of Gaia parallaxes combined with existing 2MASS photometry, nearly all early M-dwarfs out to $\simeq 100$ pc and late M-dwarfs out to

$\simeq 50$ pc have precise ($\lesssim 1\%$) parallaxes and M_{K_S} magnitudes, making scatter in existing M_{K_S} – M_* relations the dominant source of uncertainty.

We endeavored to improve on existing M_{K_S} – M_* relations and evaluate the role of [Fe/H] on the relation by expanding the sample of calibrators and using new techniques to measure the metallicity of binary M dwarfs. As part of this effort, we have been monitoring a set of nearby late K and M dwarf visual binaries using adaptive optics imaging with the goal of mapping their orbits and estimating their masses. We combined these data with similar data from Keck, CFHT, Gemini, and VLT archives, as well as astrometric measurements from the literature. The combination of literature astrometry and the recent Keck measurements were particularly important to provide the required baseline to fit long-period ($P > 10$ years) orbits.

We used these astrometric data to fit the orbits for 52 binaries, which we joined with parallaxes from the literature or derived from MEarth astrometry to determine the total masses of each system. We combined this with seven ultracool binaries from (Dupuy & Liu 2017), which were analyzed in a nearly identical way to the procedure used in this paper and provided additional coverage near the hydrogen burning limit. Seven binaries in our final sample had total mass determinations better than 1%, with a median precision of 5.6%.

We used our dynamical masses and resolved M_{K_S} magnitudes to fit for an empirical relation between M_* and M_{K_S} . Our methodology uses the observed quantity, which is the *total* mass of a given binary. While this halves the number points constraining the fit compared to using individual masses, using M_{tot} is far more robust than using model-based mass ratios, reduces the need for observationally expensive radial velocity and/or absolute astrometry (difficult without *HST* for many systems), and helps increase the range of binaries amenable to characterization (e.g., wider systems with small radial velocity amplitudes).

The resulting M_{K_S} – M_* relation covers almost an order of magnitude in M_* , from $\simeq 0.70 M_\odot$ down to the hydrogen burning limit ($\simeq 0.075 M_\odot$) and includes stars spanning the range of [Fe/H] expected for the Solar neighborhood ($-0.6 < [\text{Fe}/\text{H}] < +0.4$). Output masses from our M_{K_S} – M_* relation are precise to $\simeq 2\%$ over most of the M dwarf sequence, rising to $\simeq 3\%$ near the edges of the relation.

The $\simeq 2\%$ uncertainty is limited primarily by scatter in the input masses around the best-fit above what is expected given their assigned mass uncertainties. We characterize this scatter with a free parameter (σ_e), which we found to be $\lesssim 2\%$ for all fits. It is unclear

if σ_e arose from intrinsic variation in the M_{K_S} – M_* relation due to a missing astrophysical parameter, such as age/activity/rotation (e.g., Kraus et al. 2011; Feiden 2016; Somers & Stassun 2017) or detailed abundances (e.g., Lindgren & Heiter 2017; Veyette et al. 2017), or if σ_e represents underestimated errors in the input orbital parameters, parallaxes, or K_S magnitudes. Our adopted parallaxes are a likely contributor, as some may have their uncertainties underestimated due to uncorrected orbital motion in the input astrometry. This does not impact many targets, which had parallaxes drawn from a wide proper motion companion or measured accounting for orbital motion simultaneously. However, it is possible that the missing error is larger in magnitude, but only applies to a subset of the targets, or originates from a mix of intrinsic variation and underestimated errors.

Using empirically calibrated spectroscopic abundances, we explored the role of [Fe/H] on the M_{K_S} – M_* relation, comparing our results to expectations from evolutionary models as a guide. MIST models significantly overestimate the importance of [Fe/H] in the M_{K_S} – M_* relation ($> 4.0\sigma$), however predictions from updated DSEP models are consistent with our own. DSEP also predicts the impact of [Fe/H] will tighten (and even reverse) with decreasing M_* (increasing M_{K_S}), which is consistent with the trend seen in our own sample. Future studies with a wider range of metallicities will be useful to confirm this tightening predicted by DSEP models. Interestingly, the effect of [Fe/H] is consistent with zero at 1.7σ , suggesting a metallicity effect so weak that we will need to include targets with more extreme metallicities to characterize it.

Separate from the relative effects of [Fe/H] on the M_{K_S} – M_* relation, both model grids tested systematically underestimate M_* (at fixed M_{K_S}) for stars below $0.5 M_\odot$. For stars with $0.1 M_\odot < M_* < 0.5 M_\odot$, the difference is significant for both model grids, but the offset is larger when using MIST models ($4.1 \pm 0.6\%$) than for DSEP ($2.7 \pm 0.6\%$).

We compared our relation to recent similar relations in the literature. Given quoted uncertainties, both the Delfosse et al. (2000) and Mann et al. (2015) relations agreed with our own over the full sequence. Our results were consistent with the sample of astrometric binaries analyzed in Benedict et al. (2016), but our relation diverges from Benedict et al. (2016) above $\simeq 0.35 M_\odot$. We attribute this difference to literature points included in the Benedict et al. (2016) fit from earlier analyses (mostly eclipsing binaries) with uncertain distances and ΔK_S magnitudes. Increasing availability of Gaia parallaxes for these systems as well as ongoing efforts to measure their eclipses in range of wavelengths (e.g., Han et al. 2017)

should significantly improve their utility for studying the mass-luminosity relation of M dwarfs.

Earlier work on the mass-luminosity relation did not explore missing errors or intrinsic scatter (i.e., σ_e) in the relation, although it does appear to be present. Benedict et al. (2016), for example, achieved a χ^2 on their adopted M_{K_S} – M_* relation of 384 for 40 degrees of freedom. This may explain some of the differences between our results and that of Benedict et al. (2016) on the high-mass end, where a few mass determinations with small assigned errors may be dominating the fit.

8.2. Suggestions when using our M_{K_S} – M_* relation

To help users interested in using M_{K_S} to compute a realistic M_* and σ_{M_*} of single stars with parallaxes and K_S magnitudes, we provide a simple code to sample the fit posterior. **Before using that code or the provided MCMC posteriors, take note of the following suggestions:**

- The fit behaves poorly near the edges of the calibration sample. The scatter in the MCMC posterior accounts for this, but restrict use to $4.0 < M_{K_S} < 11.0$ ($0.075M_\odot < M_* < 0.74M_\odot$), and a ‘safe’ range would be $4.5 < M_{K_S} < 10.5$ ($0.08M_\odot < M_* < 0.67M_\odot$).
- Our relation is only valid for main-sequence stars, and the roles of youth and activity were not accounted for in our analysis. Based on the Lyon models (Baraffe et al. 2015), we advise restricting use to >100 Myr above $0.4M_\odot$, >300 Myr to $0.2M_\odot$, >500 Myr to $0.1M_\odot$, and > 1 Gyr below $0.1M_\odot$. A safer cut would be to only use this on stars >1 Gyr, similar to the calibration sample.
- The sample metallicity spans $-0.60 < [\text{Fe}/\text{H}] < +0.45$, but 85% of the binaries have $-0.40 < [\text{Fe}/\text{H}] < +0.30$. We provide a fit that attempts to take into account changes due to $[\text{Fe}/\text{H}]$, but find a weak effect (3.8% change in M_* per dex change in $[\text{Fe}/\text{H}]$). This suggests the $[\text{Fe}/\text{H}]$ -free relation is safe to use over the range of metallicities expected in the Solar neighborhood (similar to the calibration sample). We also strongly advise using the $[\text{Fe}/\text{H}]$ -free relation for stars with $M_{K_S} > 6.5$, given both the behavior of our fit and the predictions from DSEP (Figure 10b). However, given the paucity of extreme metallicity systems in our calibration sample, we advise caution when targeting more metal-poor populations. The effects of more detailed abundances (e.g., $[\alpha/\text{Fe}]$) are completely untested.

- The relation is only tested above the hydrogen burning limit. Since the boundary likely depends on metallicity (Burrows et al. 2001), it is also not possible to use a simple M_{K_S} cut even if the target is known to be old. Objects just below the hydrogen burning limit age slowly (Baraffe et al. 2015), so the relation given here may give reasonable results for many of these, but we urge caution when interpreting M_* values for $M_{K_S} > 10.5$.
- Since the origin of the σ_e value is unclear, we suggest always including this as an irreducible source of error when estimating the mass of a target.

8.3. Future directions

We intentionally selected targets that had ΔK measurements, as M_{K_S} was known to give the tightest relation with M_* for M dwarfs. Unfortunately, there is no other band with contrast ratios for all systems considered here. Most of our monitoring was done with NIRC2 on Keck, so many systems have a ΔH , but only about 1/3 of the sample have measurements in an optical band. This limits the utility of the sample, as Gaia G , BP , and RP are now widely available for early and mid-M dwarfs, and are generally measured with better precision than 2MASS K_S . The growing capabilities of speckle cameras (e.g., Horch et al. 2009) offer the opportunity to add optical contrasts. These can be converted to Gaia bandpasses, given reasonable assumptions about the component spectra, and used to derive a $M_G - M_*$ (or $M_G - M_* - [\text{Fe}/\text{H}]$) relation that can be easily applied to millions of K and M dwarfs. Complementary optical data also provide colors for individual components, from which we can measure component T_{eff} and luminosity (e.g., Kraus et al. 2017).

We would like to explore changes in the impact of $[\text{Fe}/\text{H}]$ as a function of M_{K_S} or M_* , especially given predictions from the DSEP models (Figure 10b). However, our sample was limited mostly to stars in the Solar neighborhood, and hence was heavily biased towards the narrow $[\text{Fe}/\text{H}]$ distribution of nearby stars. This limited both our ability to explore more complex impacts of $[\text{Fe}/\text{H}]$ and tighten constraints on f . We identified five additional $[\text{Fe}/\text{H}] < -0.5$ systems not included in our analysis, including two subdwarf binaries. However all of these systems had short baselines in the literature compared to their expected orbital periods. It may take $\gtrsim 2$ additional years to complete their orbits at the required precision for this kind of analysis. The availability of Gaia parallaxes will also help improve the precision of the known metal-poor systems and aid in the identification of new ones. Lastly, as new methods arrive to measure detailed abundances of M dwarfs (Veyette et al. 2016,

2017) we can explore effects beyond just [Fe/H]. This is especially useful for systems with large enough radial velocity differences between component stars to separate out individual spectra at high resolution.

Mass ratios were available for some systems (e.g., Söderhjelm 1999; Malogolovets et al. 2007; Dupuy & Liu 2017). However, these determinations were heterogeneous (e.g., some use models, some radial velocities), and some mass ratios reported in the literature are derived from orbits that disagree with our own determinations (e.g., Köhler et al. 2012). A more robust method would be to include radial velocity or absolute astrometry as part of our larger analysis. Fortunately, later Gaia data releases will include full absolute astrometry. When combined with a measure of the flux ratio in the Gaia G bandpass (a few systems are resolved in Gaia) and our existing astrometry, we will be able to fit for both individual masses and each system’s parallax. The resulting dataset will effectively double our sample size, and will help reveal the origin of σ_e .

The presence of unresolved tight companions (triples or quadruples) could bias the overall relation. A close-in third star orbiting one of the two binary components might be stable, and would not have been detected in our AO data. An unresolved, less massive companion would drive the total mass of the system higher, but has a much smaller effect on the total luminosity. So unresolved triples will sit *low* in Figure 7 (higher mass for a fixed M_{K_S}). A few stars do sit well below the fit, but not more so than expected given their mass uncertainties. Many of our targets have some radial velocity data in the literature (e.g., Delfosse et al. 1999; Raghavan et al. 2010; Benedict et al. 2016), which rule out the presence of any unresolved stellar companion. However, a more detailed analysis will require re-analysis of the radial velocity data to determine the maximum mass of an undetected companion for each individual system and convert that into a bias on the relation.

Ages of our binary sample are not known, preventing any study into the effects of age on the M_{K_S} – M_* relation. However, our larger sample of binaries with orbit measurements still in progress contains known members of nearby young moving groups and the Hyades cluster. Many of these have complete or nearly complete orbital solutions, and will soon provide a powerful set of mass benchmarks with known ages. These systems span ages from 10–650 Myr, offering the chance to both test pre-main-sequence models of M dwarfs (Montet et al. 2015; Rizzuto et al. 2016; Czekala et al. 2016; Nielsen et al. 2016) and explore the role of activity on M dwarf parameters (e.g., Spada et al. 2013; Kesseli et al. 2018). The current sample can be included in such work when

combined with age indicators like kinematics (Wojno et al. 2018), ultraviolet flux (Ansdel et al. 2015), and rotation periods expected from the Transiting Exoplanet Survey Satellite (*TESS*, Ricker et al. 2014).

The authors thank Meg Schwamb for her help with analysis of the NIRI data.

AWM was supported through Hubble Fellowship grant 51364 awarded by the Space Telescope Science Institute, which is operated by the Association of Universities for Research in Astronomy, Inc., for NASA, under contract NAS 5-26555. T.J.D. acknowledges research support from Gemini Observatory. This work was supported by a NASA Keck PI Data Award (award numbers 1554237, 1544189, 1535910, and 1521162), administered by the NASA Exoplanet Science Institute.

Data presented herein were obtained at the W. M. Keck Observatory from telescope time allocated to the National Aeronautics and Space Administration through the agency’s scientific partnership with the California Institute of Technology and the University of California. The Observatory was made possible by the generous financial support of the W. M. Keck Foundation.

The authors wish to recognize and acknowledge the very significant cultural role and reverence that the summit of Mauna Kea has always had within the indigenous Hawaiian community. We are most fortunate to have the opportunity to conduct observations from this mountain.

The authors acknowledge the Texas Advanced Computing Center (TACC) at The University of Texas at Austin for providing grid resources that have contributed to the research results reported within this paper. URL: <http://www.tacc.utexas.edu>.

Based on observations obtained at the Gemini Observatory (acquired through the Gemini Observatory Archive), which is operated by the Association of Universities for Research in Astronomy, Inc., under a cooperative agreement with the NSF on behalf of the Gemini partnership: the National Science Foundation (United States), the National Research Council (Canada), CONICYT (Chile), Ministerio de Ciencia, Tecnología e Innovación Productiva (Argentina), and Ministério da Ciência, Tecnologia e Inovação (Brazil). Observations taken from programs GN-2008B-Q-57, GN-2009B-Q-10, GN-2010B-Q-9, and GN-2011A-Q-26.

Based on observations collected at the European Organisation for Astronomical Research in the Southern Hemisphere under ESO programmes 071.C-0388(A), 072.C-0570(A), 073.C-0155(A), 075.C-0521(A), 075.C-0733(A), 077.C-0783(A), 078.C-0441(A), 079.C-0216(A), 080.C-0424(A), 081.C-0430(A), 082.C-0518(A), 082.C-0518(B), 085.C-0867(B), 086.C-0515(A), 086.C-0515(B), 090.C-

0448(A), 091.D-0804(A), 098.C-0597(A), 382.C-0324(A), and 382.D-0754(A).

This research has made use of the Keck Observatory Archive (KOA), which is operated by the W. M. Keck Observatory and the NASA Exoplanet Science Institute (NExSci), under contract with the National Aeronautics and Space Administration.

Based on observations obtained at the Canada-France-Hawaii Telescope (CFHT) which is operated by the National Research Council of Canada, the Institut National des Sciences de l'Univers of the Centre National de la Recherche Scientifique of France, and the University of Hawaii.

This work presents results from the European Space Agency (ESA) space mission Gaia. Gaia data are

being processed by the Gaia Data Processing and Analysis Consortium (DPAC). Funding for the DPAC is provided by national institutions, in particular the institutions participating in the Gaia MultiLateral Agreement (MLA). The Gaia mission website is <https://www.cosmos.esa.int/gaia>. The Gaia archive website is <https://archives.esac.esa.int/gaia>.

Software: emcee, corner.py, mpfit, scipy, pyfits, astropy, python, spextools, IDL

Facilities: Keck:II (NIRC2), IRTF (SpeX), CFHT (PUEO, aobir), VLT:Antu (NaCo); Gemini:North (NIRI)

REFERENCES

- Akaike, H. 1974, IEEE Transactions on Automatic Control, 19, 716
- Al-Shukri, A. M., McAlister, H. A., Hartkopf, W. I., Hutter, D. J., & Franz, O. G. 1996, AJ, 111, 393
- Allard, F., Homeier, D., & Freytag, B. 2012, Royal Society of London Philosophical Transactions Series A, 370, 2765
- Ansdell, M., Gaidos, E., Mann, A. W., et al. 2015, ApJ, 798, 41
- Arsenault, R., Salmon, D. A., Kerr, J. M., et al. 1994, in Proc. SPIE, Vol. 2201, Adaptive Optics in Astronomy, ed. M. A. Ealey & F. Merkle, 833–842
- Aumer, M., & Binney, J. J. 2009, MNRAS, 397, 1286
- Balega, I., Balega, Y. Y., Maksimov, A. F., et al. 2004, A&A, 422, 627
- Balega, I. I., Balega, A. F., Maksimov, E. V., et al. 2006, Bulletin of the Special Astrophysics Observatory, 59, 20
- Balega, I. I., Balega, Y. Y., Belkin, I. N., et al. 1994, Astronomy and Astrophysics Supplement Series, 105, 503
- Balega, I. I., Balega, Y. Y., Gasanova, L. T., et al. 2013, Astrophysical Bulletin, 68, 53
- Balega, I. I., Balega, Y. Y., Hofmann, K. H., et al. 2002, A&A, 385, 87
- . 2005, A&A, 433, 591
- Balega, I. I., Balega, Y. Y., Maksimov, A. F., et al. 2007, Astrophysical Bulletin, 62, 339
- . 1999, Astronomy and Astrophysics Supplement Series, 140, 287
- Balega, I. I., Balega, Y. Y., & Vasyuk, V. A. 1989, Astrofizicheskie Issledovaniya Izvestiya Spetsial'nnoj Astrofizicheskoy Observatorii, 28, 107
- Baraffe, I., Homeier, D., Allard, F., & Chabrier, G. 2015, A&A, 577, A42
- Bartlett, J. L., Lurie, J. C., Riedel, A., et al. 2017, AJ, 154, doi:10.3847/1538-3881/aa8457
- Beck, T. L., Schaefer, G. H., Simon, M., et al. 2004, ApJ, 614, 235
- Bell, C. P. M., Mamajek, E. E., & Naylor, T. 2015, MNRAS, 454, 593
- Benedict, G. F., Henry, T. J., Franz, O. G., et al. 2016, AJ, 152, 141
- Beuzit, J.-L., Ségransan, D., Forveille, T., et al. 2004, A&A, 425, 997
- Blazit, A., Bonneau, D., & Foy, R. 1987, Astronomy and Astrophysics Supplement Series, 71, 57
- Bochanski, J. J., Munn, J. A., Hawley, S. L., et al. 2007, AJ, 134, 2418
- Bonfils, X., Delfosse, X., Udry, S., et al. 2005, A&A, 442, 635
- Boyajian, T., von Braun, K., Feiden, G. A., et al. 2015, MNRAS, 447, 846
- Boyajian, T. S., von Braun, K., van Belle, G., et al. 2012, ApJ, 757, 112
- Brewer, J. M., Fischer, D. A., Basu, S., Valenti, J. A., & Piskunov, N. 2015, ApJ, 805, 126
- Brewer, J. M., Fischer, D. A., Valenti, J. A., & Piskunov, N. 2016, ApJS, 225, 32
- Burrows, A., Hubbard, W. B., Lunine, J. I., & Liebert, J. 2001, Reviews of Modern Physics, 73, 719
- Casagrande, L., Schönrich, R., Asplund, M., et al. 2011, A&A, 530, A138
- Castelli, F., & Kurucz, R. L. 2004, ArXiv e-prints, astro
- Chen, Y., Girardi, L., Bressan, A., et al. 2014, MNRAS, 444, 2525
- Choi, J., Dotter, A., Conroy, C., et al. 2016, ApJ, 823, 102
- Chung, S. J., Zhu, W., Udalski, A., et al. 2017, ApJ, 838, 154

- Cohen, M., Wheaton, W. A., & Megeath, S. T. 2003, AJ, 126, 1090
- Conroy, C., & van Dokkum, P. 2012, ApJ, 747, 69
- Covey, K. R., Hawley, S. L., Bochanski, J. J., et al. 2008, AJ, 136, 1778
- Cushing, M. C., Vacca, W. D., & Rayner, J. T. 2004, PASP, 116, 362
- Czekala, I., Andrews, S. M., Torres, G., et al. 2016, ApJ, 818, doi:10.3847/0004-637X/818/2/156
- Delfosse, X., Forveille, T., Beuzit, J.-L., et al. 1999, A&A, 344, 897
- Delfosse, X., Forveille, T., Ségransan, D., et al. 2000, A&A, 364, 217
- Dieterich, S. B., Henry, T. J., Golimowski, D. A., Krist, J. E., & Tanner, A. M. 2012, AJ, 144, doi:10.1088/0004-6256/144/2/64
- Dieterich, S. B., Henry, T. J., Jao, W.-C., et al. 2014, AJ, 147, 94
- Diolaiti, E., Bendinelli, O., Bonaccini, D., et al. 2000, A&AS, 147, 335
- Dittmann, J. A., Irwin, J. M., Charbonneau, D., & Berta-Thompson, Z. K. 2014, ApJ, 784, 156
- Dittmann, J. A., Irwin, J. M., Charbonneau, D., et al. 2017, Nature, 544, 333
- Docobo, J. A., Tamazian, V. S., Balega, Y. Y., & Melikian, N. D. 2006, AJ, 132, 994
- Dotter, A. 2016, ApJS, 222, 8
- Dotter, A., Chaboyer, B., Jevremović, D., et al. 2008, ApJS, 178, 89
- Douglass, G. G., Mason, B. D., Rafferty, T. J., Holdenried, E. R., & Germain, M. E. 2000, AJ, 119, 3071
- Doyon, R., Nadeau, D., Vallee, P., et al. 1998, in Proc. SPIE, Vol. 3354, Infrared Astronomical Instrumentation, ed. A. M. Fowler, 760–768
- Dressing, C. D., & Charbonneau, D. 2013, ApJ, 767, 95
- Dressing, C. D., Newton, E. R., Schlieder, J. E., et al. 2017, ApJ, 836, 167
- Dupuy, T. J., Kratter, K. M., Kraus, A. L., et al. 2016, ApJ, 817, 80
- Dupuy, T. J., & Liu, M. C. 2012, ApJS, 201, 19
- . 2017, ApJS, 231, 15
- Dupuy, T. J., Liu, M. C., & Bowler, B. P. 2009a, ApJ, 706, 328
- Dupuy, T. J., Liu, M. C., Bowler, B. P., et al. 2010, ApJ, 721, 1725
- Dupuy, T. J., Liu, M. C., & Ireland, M. J. 2009b, ApJ, 699, 168
- Evans, D. F. 2018, Research Notes of the American Astronomical Society, 2, 20
- Evans, T. M., Ireland, M. J., Kraus, A. L., et al. 2012, ApJ, 744, 120
- Farrington, C. D., ten Brummelaar, T. A., Mason, B. D., et al. 2010, AJ, 139, 2308
- Feiden, G. A. 2016, A&A, 593, A99
- Feiden, G. A., & Chaboyer, B. 2012, ApJ, 757, 42
- . 2013, ApJ, 779, 183
- . 2014a, ApJ, 789, 53
- . 2014b, A&A, 571, A70
- Ferguson, D., Gardner, S., & Yanny, B. 2017, ApJ, 843, 141
- Finch, C. T., & Zacharias, N. 2016, AJ, 151, doi:10.3847/0004-6256/151/6/160
- Foreman-Mackey, D. 2016, The Journal of Open Source Software, 24, doi:10.21105/joss.00024
- Foreman-Mackey, D., Hogg, D. W., Lang, D., & Goodman, J. 2013, PASP, 125, 306
- Fortney, J. J. 2012, ApJL, 747, L27
- Forveille, T., Beuzit, J.-L., Delfosse, X., et al. 1999, A&A, 351, 619
- Fu, H.-H., Hartkopf, W. I., Mason, B. D., et al. 1997, AJ, 114, 1623
- Gagné, J., Lafrenière, D., Doyon, R., Malo, L., & Artigau, É. 2014, ApJ, 783, 121
- . 2015, ApJ, 798, 73
- Gaia Collaboration, Brown, A. G. A., Vallenari, A., et al. 2018, ArXiv e-prints, arXiv:1804.09365
- . 2016, A&A, 595, A2
- Gaidos, E. 2015, ApJ, 804, 40
- Gaidos, E., Mann, A. W., Kraus, A. L., & Ireland, M. 2016, MNRAS, 457, 2877
- Gaidos, E., Mann, A. W., Lépine, S., et al. 2014, MNRAS, 443, 2561
- Geyer, D. W., Harrington, R. S., & Worley, C. E. 1988, AJ, 95, 1841
- Gillon, M., Triaud, A. H. M. J., Demory, B.-O., et al. 2017, Nature, 542, 456
- Goldin, A., & Makarov, V. V. 2006, The Astrophysical Journal Supplement Series, 166, 341
- Goodman, J., & Weare, J. 2010, Commun. Appl. Math. Comput. Sci., 5, 65
- Goodman, J., & Weare, J. 2010, Communications in Applied Mathematics and Computational Science, Vol. 5, No. 1, p. 65-80, 2010, 5, 65
- Han, E., Muirhead, P. S., Swift, J. J., et al. 2017, AJ, 154, doi:10.3847/1538-3881/aa803c
- Hansen, C. J., Kawaler, S. D., & Trimble, V. 2004, Stellar interiors : physical principles, structure, and evolution (Springer)
- Hartkopf, W. I., & Mason, B. D. 2009, AJ, 138, 813

- Hartkopf, W. I., Mason, B. D., & McAlister, H. A. 1996, AJ, 111, 370
- Hartkopf, W. I., Mason, B. D., & Rafferty, T. J. 2008, AJ, 135, 1334
- Hartkopf, W. I., Mc Alister, H. A., & Franz, O. G. 1992, AJ, 104, 810
- Hartkopf, W. I., McAlister, H. A., & Mason, B. D. 2001, AJ, 122, 3480
- Hartkopf, W. I., McAlister, H. A., Mason, B. D., et al. 1994, AJ, 108, 2299
- . 1997, AJ, 114, 1639
- Hartkopf, W. I., Mason, B. D., McAlister, H. A., et al. 2000, AJ, 119, 3084
- Hauschildt, P. H., Allard, F., & Baron, E. 1999a, ApJ, 512, 377
- Hauschildt, P. H., Allard, F., Ferguson, J., Baron, E., & Alexander, D. R. 1999b, ApJ, 525, 871
- Hejazi, N., De Robertis, M. M., & Dawson, P. C. 2015, AJ, 149, 140
- Hełminiak, K. G., Konacki, M., Kulkarni, S. R., & Eisner, J. 2009, MNRAS, 400, 406
- Henry, T. J., Kirkpatrick, J. D., & Simons, D. A. 1994, AJ, 108, 1437
- Henry, T. J., & McCarthy, Jr., D. W. 1993, AJ, 106, 773
- Hinkel, N. R., Timmes, F. X., Young, P. A., Pagano, M. D., & Turnbull, M. C. 2014, AJ, 148, 54
- Hinkel, N. R., Young, P. A., Pagano, M. D., et al. 2016, ApJS, 226, 4
- Hodapp, K. W., Jensen, J. B., Irwin, E. M., et al. 2003, PASP, 115, 1388
- Horch, E. P., Bahi, L. A. P., Gaulin, J. R., et al. 2012, AJ, 143, doi:10.1088/0004-6256/143/1/10
- Horch, E. P., Falta, D., Anderson, L. M., et al. 2010, AJ, 139, 205
- Horch, E. P., Gomez, S. C., Sherry, W. H., et al. 2011, AJ, 141, doi:10.1088/0004-6256/141/2/45
- Horch, E. P., Robinson, S. E., Meyer, R. D., et al. 2002, AJ, 123, 3442
- Horch, E. P., van Altena, W. F., Cyr, William M., J., et al. 2008, AJ, 136, doi:10.1088/0004-6256/136/1/312
- Horch, E. P., Veillette, D. R., Baena Gallé, R., et al. 2009, AJ, 137, 5057
- Horch, E. P., van Altena, W. F., Demarque, P., et al. 2015, AJ, 149, doi:10.1088/0004-6256/149/5/151
- Horch, E. P., Caselli-Dinescu, D. I., Camarata, M. A., et al. 2017, AJ, 153, doi:10.3847/1538-3881/aa6749
- Janson, M., Bergfors, C., Brandner, W., et al. 2014, ApJ, 789, 102
- Janson, M., Hormuth, F., Bergfors, C., et al. 2012, ApJ, 754, 44
- Jódar, E., Pérez-Garrido, A., Díaz-Sánchez, A., et al. 2013, MNRAS, 429, 859
- Johnson, J. A., & Apps, K. 2009, ApJ, 699, 933
- Jurić, M., Ivezić, Ž., Brooks, A., et al. 2008, ApJ, 673, 864
- Kervella, P., Mérand, A., Ledoux, C., Demory, B. O., & Le Bouquin, J. B. 2016, A&A, 593, doi:10.1051/0004-6361/201628631
- Kesseli, A. Y., Muirhead, P. S., Mann, A. W., & Mace, G. 2018, ArXiv e-prints, arXiv:1804.04133
- Köhler, R., Ratzka, T., & Leinert, C. 2012, A&A, 541, doi:10.1051/0004-6361/201118707
- Kraus, A. L., Cody, A. M., Covey, K. R., et al. 2015, ApJ, 807, 3
- Kraus, A. L., Ireland, M. J., Huber, D., Mann, A. W., & Dupuy, T. J. 2016, AJ, 152, 8
- Kraus, A. L., Ireland, M. J., Martinache, F., & Lloyd, J. P. 2008, ApJ, 679, 762
- Kraus, A. L., Shkolnik, E. L., Allers, K. N., & Liu, M. C. 2014, AJ, 147, 146
- Kraus, A. L., Tucker, R. A., Thompson, M. I., Craine, E. R., & Hillenbrand, L. A. 2011, ApJ, 728, 48
- Kraus, A. L., Douglas, S. T., Mann, A. W., et al. 2017, ApJ, 845, 72
- Law, N. M., Dhital, S., Kraus, A., Stassun, K. G., & West, A. A. 2010, ApJ, 720, 1727
- Law, N. M., Hodgkin, S. T., & Mackay, C. D. 2008, MNRAS, 384, 150
- Lee, J., & Song, I. 2018, MNRAS, 475, 2955
- Lejeune, T., Cuisinier, F., & Buser, R. 1998, Astronomy and Astrophysics Supplement Series, 130, 65
- Lépine, S., Hilton, E. J., Mann, A. W., et al. 2013, AJ, 145, 102
- Lépine, S., Rich, R. M., & Shara, M. M. 2007, ApJ, 669, 1235
- Lindgren, L., Hernandez, J., Bombrun, A., et al. 2018, ArXiv e-prints, arXiv:1804.09366
- Lindgren, S., & Heiter, U. 2017, A&A, 604, A97
- Liu, M. C., Dupuy, T. J., & Ireland, M. J. 2008, ApJ, 689, 436
- Lloyd, J. P., Martinache, F., Ireland, M. J., et al. 2006, ApJL, 650, L131
- López-Morales, M., & Ribas, I. 2005, ApJ, 631, 1120
- Losse, F. 2010, Observations et Travaux, 75, 17
- Lu, J. R., Ghez, A. M., Yelda, S., et al. 2010, in Proceedings of the SPIE, Volume 7736, id. 77361I (2010)., Vol. 7736
- Lurie, J. C., Davenport, J. R. A., Hawley, S. L., et al. 2015, ApJ, 800, 95
- Mace, G. N., Mann, A. W., Skiff, B. A., et al. 2018, ApJ, 854, doi:10.3847/1538-4357/aaa8dd
- Malo, L., Artigau, É., Doyon, R., et al. 2014, ApJ, 788, 81

- Malogolovets, E. V., Balega, Y. Y., Rastegaev, D. A., Hofmann, K. H., & Weigelt, G. 2007, *Astrophysical Bulletin*, 62, 117
- Mann, A. W., Brewer, J. M., Gaidos, E., Lépine, S., & Hilton, E. J. 2013a, *AJ*, 145, 52
- Mann, A. W., Deacon, N. R., Gaidos, E., et al. 2014, *AJ*, 147, 160
- Mann, A. W., Feiden, G. A., Gaidos, E., Boyajian, T., & von Braun, K. 2015, *ApJ*, 804, 64
- Mann, A. W., Gaidos, E., & Ansdell, M. 2013b, *ApJ*, 779, 188
- Mann, A. W., Gaidos, E., Lépine, S., & Hilton, E. J. 2012, *ApJ*, 753, 90
- Mann, A. W., & von Braun, K. 2015, *PASP*, 127, 102
- Mann, A. W., Vanderburg, A., Rizzuto, A. C., et al. 2018, *AJ*, 155, 4
- Markwardt, C. B. 2009, in *Astronomical Society of the Pacific Conference Series*, Vol. 411, *Astronomical Data Analysis Software and Systems XVIII*, ed. D. A. Bohlender, D. Durand, & P. Dowler, 251
- Martinache, F., Lloyd, J. P., Ireland, M. J., Yamada, R. S., & Tuthill, P. G. 2007, *ApJ*, 661, 496
- Martinez, A. O., Crossfield, I. J. M., Schlieder, J. E., et al. 2017, *ApJ*, 837, 72
- Masciadri, E., Brandner, W., Bouy, H., et al. 2003, *A&A*, 411, 157
- Mason, B. D., Hartkopf, W. I., & Wycoff, G. L. 2011, *AJ*, 141, doi:10.1088/0004-6256/141/5/157
- Mason, B. D., Hartkopf, W. I., Wycoff, G. L., et al. 2004a, *AJ*, 128, 3012
- . 2004b, *AJ*, 127, 539
- McAlister, H. A., Hartkopf, W. I., & Franz, O. G. 1990, *AJ*, 99, 965
- McAlister, H. A., Hartkopf, W. I., Hutter, D. J., & Franz, O. G. 1987, *AJ*, 93, 688
- McAlister, H. A., Hartkopf, W. I., Sowell, J. R., Dombrowski, E. G., & Franz, O. G. 1989, *AJ*, 97, 510
- McAlister, H. A., Hendry, E. M., Hartkopf, W. I., Campbell, B. G., & Fekel, F. C. 1983, *The Astrophysical Journal Supplement Series*, 51, 309
- McConnell, N. J., Lu, J. R., & Mann, A. W. 2016, *ApJ*, 821, 39
- Michalik, D., Lindegren, L., & Hobbs, D. 2015, *A&A*, 574, A115
- Montet, B. T., Bowler, B. P., Shkolnik, E. L., et al. 2015, *ApJL*, 813, L11
- Muirhead, P. S., Hamren, K., Schlawin, E., et al. 2012a, *ApJL*, 750, L37
- Muirhead, P. S., Johnson, J. A., Apps, K., et al. 2012b, *ApJ*, 747, 144
- Muirhead, P. S., Becker, J., Feiden, G. A., et al. 2014, *ApJS*, 213, 5
- Muirhead, P. S., Mann, A. W., Vanderburg, A., et al. 2015, *ApJ*, 801, 18
- Mulders, G. D., Pascucci, I., & Apai, D. 2015, *ApJ*, 798, 112
- Neuhäuser, R., Guenther, E. W., Wuchterl, G., et al. 2005, *A&A*, 435, L13
- Neves, V., Bonfils, X., Santos, N. C., et al. 2014, *A&A*, 568, A121
- . 2012, *A&A*, 538, A25
- Newton, E. R., Charbonneau, D., Irwin, J., et al. 2014, *AJ*, 147, 20
- Newton, E. R., Charbonneau, D., Irwin, J., & Mann, A. W. 2015, *ApJ*, 800, 85
- Newton, E. R., Irwin, J., Charbonneau, D., et al. 2017, *ApJ*, 834, 85
- Nielsen, E. L., De Rosa, R. J., Wang, J., et al. 2016, *AJ*, 152, 175
- Nutzman, P., & Charbonneau, D. 2008, *PASP*, 120, 317
- Park, C., Jaffe, D. T., Yuk, I.-S., et al. 2014, in *Society of Photo-Optical Instrumentation Engineers (SPIE) Conference Series*, Vol. 9147, *Society of Photo-Optical Instrumentation Engineers (SPIE) Conference Series*, 1
- Petigura, E. A., Howard, A. W., & Marcy, G. W. 2013, *Proceedings of the National Academy of Science*, 110, 19273
- Raghavan, D., McAlister, H. A., Henry, T. J., et al. 2010, *ApJS*, 190, 1
- Rajpurohit, A. S., Reylé, C., Allard, F., et al. 2013, *A&A*, 556, A15
- Rayner, J., Bond, T., Bonnet, M., et al. 2012, in *Proc. SPIE*, Vol. 8446, *Ground-based and Airborne Instrumentation for Astronomy IV*, 84462C
- Rayner, J. T., Toomey, D. W., Onaka, P. M., et al. 2003, *PASP*, 115, 362
- Reid, I. N., Gizis, J. E., & Hawley, S. L. 2002, *AJ*, 124, 2721
- Reid, I. N., Cruz, K. L., Allen, P., et al. 2004, *AJ*, 128, 463
- Ribas, I. 2003, *A&A*, 398, 239
- Rica, F. M., Barrena, R., Vázquez, G., Henríquez, J. A., & Hernández, F. 2012, *MNRAS*, 419, 197
- Ricker, G. R., Winn, J. N., Vanderspek, R., et al. 2014, in *Society of Photo-Optical Instrumentation Engineers (SPIE) Conference Series*, Vol. 9143, 20
- Riddle, R. L., Tokovinin, A., Mason, B. D., et al. 2015, *ApJ*, 799, doi:10.1088/0004-637X/799/1/4
- Riedel, A. R., Blunt, S. C., Lambrides, E. L., et al. 2017, *AJ*, 153, 95
- Rizzuto, A. C., Ireland, M. J., Dupuy, T. J., & Kraus, A. L. 2016, *ApJ*, 817, 164

- Rizzuto, A. C., Mann, A. W., Vanderburg, A., Kraus, A. L., & Covey, K. R. 2017, AJ, 154, 224
- Rodriguez, D. R., Duchêne, G., Tom, H., et al. 2015, MNRAS, 449, 3160
- Rojas-Ayala, B., Covey, K. R., Muirhead, P. S., & Lloyd, J. P. 2010, ApJL, 720, L113
- . 2012, ApJ, 748, 93
- Schlieder, J. E., Lépine, S., Rice, E., et al. 2012, AJ, 143, 114
- Schroeder, D. J., Goliowski, D. A., Brukardt, R. A., et al. 2000, AJ, 119, 906
- Ségransan, D., Delfosse, X., Forveille, T., et al. 2000, A&A, 364, 665
- Seifahrt, A., Röll, T., Neuhäuser, R., et al. 2008, A&A, 484, 429
- Service, M., Lu, J. R., Campbell, R., et al. 2016, PASP, 128, 095004
- Shields, A. L., Ballard, S., & Johnson, J. A. 2016, PhR, 663, 1
- Shin, I. G., Udalski, A., Yee, J. C., et al. 2017, AJ, 154, 176
- Shkolnik, E. L., Allers, K. N., Kraus, A. L., Liu, M. C., & Flagg, L. 2017, AJ, 154, doi:10.3847/1538-3881/aa77fa
- Shkolnik, E. L., Anglada-Escudé, G., Liu, M. C., et al. 2012, ApJ, 758, 56
- Skrutskie, M. F., Cutri, R. M., Stiening, R., et al. 2006, AJ, 131, 1163
- Söderhjelm, S. 1999, A&A, 341, 121
- Somers, G., & Stassun, K. G. 2017, AJ, 153, 101
- Spada, F., Demarque, P., Kim, Y.-C., & Sills, A. 2013, ApJ, 776, 87
- Spinelli, C., Barnabè, M., Koopmans, L. V. E., & Trager, S. C. 2015, MNRAS, 452, L21
- Stapelfeldt, K. R., Ménard, F., Watson, A. M., et al. 2003, ApJ, 589, 410
- Stassun, K. G., Kratter, K. M., Scholz, A., & Dupuy, T. J. 2012, ApJ, 756, 47
- Stevens, D. J., Gaudi, B. S., & Stassun, K. G. 2017, ArXiv e-prints, arXiv:1712.05046
- Tarter, J. C., Backus, P. R., Mancinelli, R. L., et al. 2007, Astrobiology, 7, 30
- Terrien, R. C., Mahadevan, S., Bender, C. F., et al. 2012, ApJL, 747, L38
- Terrien, R. C., Mahadevan, S., Deshpande, R., & Bender, C. F. 2015, ApJS, 220, 16
- Teske, J. K., Ghezzi, L., Cunha, K., et al. 2015, ApJL, 801, L10
- Tokovinin, A. 2017, AJ, 154, doi:10.3847/1538-3881/aa8459
- . 2018, ApJS, 235, 6
- Tokovinin, A., Mason, B. D., & Hartkopf, W. I. 2010, AJ, 139, 743
- . 2014, AJ, 147, doi:10.1088/0004-6256/147/5/123
- Tokovinin, A. A., & Smekhov, M. G. 2002, A&A, 382, 118
- Torres, G., Andersen, J., & Giménez, A. 2010, A&A Rv, 18, 67
- Torres, G., & Ribas, I. 2002, ApJ, 567, 1140
- Vacca, W. D., Cushing, M. C., & Rayner, J. T. 2003, PASP, 115, 389
- van Altena, W. F., Lee, J. T., & Hoffleit, E. D. 1995, The general catalogue of trigonometric [stellar] parallaxes (Yale University Observatory)
- van Dam, M. A., Le Mignant, D., & Macintosh, B. A. 2004, ApOpt, 43, 5458
- van Dokkum, P. G. 2001, PASP, 113, 1420
- Van Grootel, V., Fernandes, C. S., Gillon, M., et al. 2018, ApJ, 853, doi:10.3847/1538-4357/aaa023
- van Leeuwen, F. 2007, A&A, 474, 653
- Veyette, M. J., Muirhead, P. S., Mann, A. W., & Allard, F. 2016, ApJ, 828, 95
- Veyette, M. J., Muirhead, P. S., Mann, A. W., et al. 2017, ApJ, 851, 26
- Ward-Duong, K., Patience, J., De Rosa, R. J., et al. 2015, MNRAS, 449, 2618
- Wheeler, J. C. 2012, ApJ, 758, 123
- Winters, J. G., Hambly, N. C., Jao, W.-C., et al. 2015, AJ, 149, 5
- Wizinowich, P., Acton, D. S., Shelton, C., et al. 2000, PASP, 112, 315
- Woitas, J., Tamazian, V. S., Docobo, J. A., & Leinert, C. 2003, A&A, 406, 293
- Wojno, J., Kordopatis, G., Steinmetz, M., et al. 2018, MNRAS, arXiv:1804.06379
- Woolf, V. M., & Wallerstein, G. 2006, PASP, 118, 218
- Woolf, V. M., & West, A. A. 2012, MNRAS, 422, 1489
- Yelda, S., Lu, J. R., Ghez, A. M., et al. 2010, ApJ, 725, 331
- Yi, Z.-P., Luo, A.-L., Zhao, J.-K., et al. 2015, Research in Astronomy and Astrophysics, 15, 860
- Yuk, I.-S., Jaffe, D. T., Barnes, S., et al. 2010, in Society of Photo-Optical Instrumentation Engineers (SPIE) Conference Series, Vol. 7735, Society of Photo-Optical Instrumentation Engineers (SPIE) Conference Series
- Zhu, W., Calchi Novati, S., Gould, A., et al. 2016, ApJ, 825, 60

Table 3. Binary Sample

Name	Comp	R.A. J2000	Dec J2000	System K_S (mag)	ΔK_S (mag)	M_{tot} (M_{\odot})	[Fe/H] ^a (dex)	Plx (mas)	Plx Ref
Systems analyzed in this paper									
GJ 1005	AB	00:15:28.0	-16:08:01	6.310±0.018 ^b	1.145±0.016	0.3189 ± 0.0023	-0.41	166.60 ±0.30	3
GJ 2005	BC	00:24:44.1	-27:08:24	9.371±0.050 ^e	0.320±0.016	0.1570 ± 0.0055	-0.08	128.5 ±1.5	3
Gl 22	AC	00:32:29.2	+67:14:08	6.037±0.023	2.060±0.035	0.5484 ± 0.0033	-0.24	100.405±0.070	3
Gl 54	AB	01:10:22.8	-67:26:42	5.132±0.024	0.697±0.036	0.7499 ± 0.0099	+0.17	126.90 ±0.40	3
GJ 1038	AB	01:25:01.8	-32:51:04	6.207±0.021	0.058±0.016	1.30 ± 0.20	+0.03	39.8 ±1.6	2
Gl 65	AB	01:39:01.2	-17:57:02	5.343±0.021	0.161±0.019	0.2372 ± 0.0053	+0.04	373.7 ±2.7	5
Gl 84	AB	02:05:04.8	-17:36:52	5.662±0.020	3.262±0.016	0.517 ± 0.028	-0.14	109.4 ±1.9	2,5
2M0213+36	AB	02:13:20.6	+36:48:50	8.518±0.018	1.493±0.018	0.245 ± 0.035	-0.07	74.6 ±3.5	6
Gl 98	AB	02:27:45.9	+04:25:55	5.113±0.018	0.068±0.015	1.389 ± 0.079	+0.41	58.3 ±1.1	2
Gl 99	AB	02:28:46.5	+32:15:34	6.062±0.018	0.254±0.016	1.46 ± 0.18	+0.21	38.2 ±1.6	2
Gl 125	AB	03:09:30.8	+45:43:58	5.840±0.016	1.140±0.016	0.905 ± 0.081	+0.49	63.5 ±1.9	2
Gl 190	AB	05:08:35.0	-18:10:18	5.314±0.018	0.103±0.017	0.835 ± 0.053	+0.25	107.9 ±2.1	2
GJ 1081	AB	05:33:19.1	+44:48:58	7.335±0.027	0.949±0.018	0.583 ± 0.043	-0.03	65.20 ±0.40	3
Gl 234	AB	06:29:23.3	-02:48:49	5.421±0.018 ^b	1.526±0.016	0.3331 ± 0.0017	+0.11	241.00 ±0.40	3
GJ 3412	AB	06:54:04.2	+60:52:18	6.391±0.025 ^b	1.120±0.016	0.5277 ± 0.0074	-0.21	95.60 ±0.30	3
GJ 3421	AB	07:03:55.7	+52:42:06	7.776±0.021	0.155±0.017	0.2481 ± 0.0093	-0.60	112.6 ±1.4	3
Gl 263	AB	07:04:17.7	-10:30:31	6.427±0.017	0.441±0.020	0.95 ± 0.14	+0.43	62.0 ±2.9	2,5
Gl 277	AC	07:31:57.7	+36:13:09	5.927±0.017	1.931±0.016	0.738 ± 0.020	+0.18	83.330±0.070	12
GJ 3454	AB	07:36:25.1	+07:04:43	7.282±0.020	0.272±0.016	0.279 ± 0.015	+0.03	117.1 ±2.1	1
Gl 301	AB	08:13:08.5	-13:55:01	5.815±0.026	0.506±0.018	1.23 ± 0.14	-0.18	52.1 ±2.0	5,8
Gl 310	AB	08:36:25.5	+67:17:42	5.580±0.015	2.134±0.017	0.778 ± 0.067	-0.06	72.6 ±1.3	2
Gl 330	AB	08:57:04.6	+11:38:49	6.486±0.023	1.086±0.016	0.92 ± 0.14	-0.17	58.8 ±2.7	2
LHS 6167	AB	09:15:36.4	-10:35:47	7.733±0.017	0.143±0.016	0.2809 ± 0.0087	-0.13	103.3 ±1.0	10
Gl 340	AB	09:17:53.4	+28:33:38	4.767±0.017	0.024±0.020	1.357 ± 0.055	-0.39	57.92 ±0.76	2
Gl 352	AB	09:31:19.4	-13:29:19	5.511±0.020	0.119±0.018	0.780 ± 0.075	-0.03	98.5 ±3.1	5,9
Gl 381	AB	10:12:04.6	-02:41:04	6.193±0.026	0.811±0.016	0.765 ± 0.082	-0.12	83.5 ±2.8	2,5
Gl 416	AB	11:11:33.1	-14:59:28	5.874±0.017	0.980±0.017	1.19 ± 0.10	-0.20	46.4 ±1.3	2
Gl 469	AB	12:28:57.6	+08:25:31	6.956±0.026	1.100±0.016	0.514 ± 0.011	+0.19	76.40 ±0.50	3
Gl 473	AB	12:33:17.4	+09:01:15	6.042±0.020	0.001±0.018	0.262 ± 0.016	+0.09	227.9 ±4.6	5
Gl 494	AB	13:00:46.6	+12:22:32	5.578±0.016	4.269±0.017	0.667 ± 0.035	+0.30	85.5 ±1.5	2
Gl 570	BC	14:57:26.5	-21:24:40	3.855±0.045 ^b	0.995±0.046	0.837 ± 0.052	+0.18	171.22 ±0.94	2
Gl 600	AB	15:52:08.1	+10:52:28	5.819±0.023	0.029±0.018	1.228 ± 0.032	+0.01	47.65 ±0.30	11
Gl 623	AB	16:24:09.2	+48:21:10	5.915±0.023	2.501±0.040	0.4647 ± 0.0041	-0.44	127.50 ±0.30	3
GJ 1210	AB	17:07:40.8	+07:22:06	8.419±0.025	0.075±0.017	0.218 ± 0.019	-0.19	86.8 ±2.5	1
Gl 660	AB	17:11:52.2	-01:51:06	6.656±0.021	0.033±0.017	0.606 ± 0.053	-0.20	85.2 ±2.5	5,9
Gl 661	AB	17:12:07.8	+45:39:58	4.834±0.023	0.251±0.020	0.596 ± 0.054	-0.41	167.3 ±5.0	2
GJ 4024	AB	17:43:00.7	+05:47:21	6.631±0.018	0.931±0.016	0.92 ± 0.14	-0.09	50.1 ±2.5	2

Table 3 continued

Table 3 (*continued*)

Name	Comp	R.A.	Dec	System K_S	ΔK_S	M_{tot}	[Fe/H] ^a	Plx	Plx
		J2000	J2000	(mag)	(mag)	(M_{\odot})	(dex)	(mas)	Ref
Gl 695	BC	17:46:25.1	+27:43:00	4.953±0.016	0.287±0.016	0.868 ± 0.023	+0.22	120.33 ±0.16	2
Gl 747	AB	19:07:42.9	+32:32:41	6.416±0.020	0.098±0.016	0.429 ± 0.026	-0.20	122.3 ±2.5	5
Gl 748	AB	19:12:14.5	+02:53:11	6.342±0.018 ^b	1.035±0.024	0.5382 ± 0.0071	-0.23	98.40 ±0.30	3
Gl 762.1	AB	19:31:08.5	+58:35:13	4.463±0.015	0.08 ± 0.12	1.469 ± 0.067	-0.17	58.37 ±0.54	2
Gl 765.2	AB	19:39:05.9	+76:25:18	5.898±0.016	0.371±0.037	1.330 ± 0.068	-0.35	33.67 ±0.53	2
GJ 1245	AC	19:53:54.4	+44:24:53	6.854±0.016	1.124±0.016	0.20321±0.00042	+0.01	214.528±0.082	12
Gl 791.2	AB	20:29:48.3	+09:41:20	7.307±0.024	1.565±0.018	0.298 ± 0.020	+0.05	113.40 ±0.20	3
Gl 804	AB	20:44:21.9	+19:44:59	6.553±0.016	1.083±0.016	1.00 ± 0.13	-0.09	47.4 ±2.1	2
Gl 831	AB	21:31:18.5	-09:47:26	6.379±0.020	1.221±0.016	0.4184 ± 0.0033	+0.20	125.30 ±0.30	3
Gl 844	AB	22:01:49.0	+16:28:02	6.180±0.021	0.108±0.016	0.872 ± 0.095	+0.21	61.8 ±2.2	2
HD 239960	AB	22:27:59.5	+57:41:45	4.777±0.029	0.994±0.017	0.460 ± 0.011	-0.11	249.9 ±1.9	2
GJ4287	AB	22:37:29.9	+39:22:51	5.872±0.027	0.913±0.016	1.187 ± 0.020	+0.03	47.61 ±0.20	12
Gl 893.4	AB	23:16:39.7	+19:37:17	7.303±0.017	0.052±0.016	0.85 ± 0.12	-0.17	32.5 ±1.5	1
Gl 900	BC	23:35:00.2	+01:36:19	7.571±0.050 ^e	0.758±0.018	0.610 ± 0.016	+0.03	48.17 ±0.31	11
Gl 913	AB	23:58:43.4	+46:43:44	5.831±0.020	1.327±0.018	0.89 ± 0.12	-0.12	68.0 ±3.0	7
Systems from Dupuy & Liu (2017)									
LHS1901	AB	07:11:11.4	+43:29:58	9.126±0.018	0.094±0.010	0.2029 ± 0.0090	-0.41	76.4 ±1.1	4
2M0746+20	AB	07:46:42.5	+20:00:32	10.468±0.022	0.357±0.025	0.1535 ± 0.0017	-0.18 ^d	81.24 ±0.25	4
2M1017+13	AB	10:17:07.5	+13:08:39	12.710±0.023	0.113±0.024	0.149 ± 0.016	-0.35 ^d	32.2 ±1.2	4
2M1047+40	AB	10:47:13.8	+40:26:49	11.254±0.018	0.289±0.049	0.171 ± 0.012	+0.17	39.02 ±0.90	4
LSJ1735+26	AB	17:35:12.9	+26:34:47	10.157±0.020	0.490±0.020	0.1779 ± 0.0078	+0.03	64.82 ±0.95	4
2M2140+16	AB	21:40:29.3	+16:25:18	11.826±0.031	0.743±0.075	0.190 ± 0.017	-0.10 ^c	29.52 ±0.88	4
2M2206-20	AB	22:06:22.8	-20:47:05	11.315±0.027	0.067±0.016	0.168 ± 0.016	-0.05 ^c	36.6 ±1.2	4

NOTE—Parallax references: 1 = This work (MEarth), 2 = van Leeuwen (2007), 3 = Benedict et al. (2016), 4 = Dupuy & Liu (2017), 5 = van Altena et al. (1995), 6 = Finch & Zacharias (2016), 7 = Goldin & Makarov (2006), 8 = Winters et al. (2015), 9 = Söderhjelm (1999), 10 = Bartlett et al. (2017), 11 = Gaia Collaboration et al. (2016), 12 = companion to star in Lindegren et al. (2018).

^aErrors on [Fe/H] are limited primarily by the calibration (Mann et al. 2013a, 2014), and are 0.08 dex for all targets unless otherwise noted.

^bSynthetic K_S magnitudes derived from spectra. All other K_S magnitudes are from 2MASS.

^cAbundance derived from lower-resolution IRTF spectrum, σ [Fe/H] estimated to be 0.12 dex.

^dL dwarfs are beyond the calibration range of Mann et al. (2014) ; [Fe/H] values should be used with caution.

^e K_S magnitude from 2MASS contains a third star, listed K_S magnitude has third star's flux removed.

Table 4. Orbital Parameters

Name	P (years)	a'' (mas)	i (degrees)	e	ω (degrees)	Ω (degrees)	T_0 MJD	a''/P arcsec ³ yr ⁻²	χ^2/dof
GJ 1005	4.55725 ^{+0.00077} _{-0.00077}	312.90 ^{+0.50} _{-0.50}	0.36123 ^{+0.00097} _{-0.00097}	143.89 ^{+0.25} _{-0.25}	345.21 ^{+0.63} _{-0.62}	61.20 ^{+0.41} _{-0.40}	58172.8 ^{+1.9} _{-1.9}	(1.4751 \pm 0.0073) $\times 10^3$	88.5/71
GJ 2005	17.280 ^{+0.010} _{-0.010}	463.34 ^{+0.54} _{-0.54}	0.03029 ^{+0.00090} _{-0.00087}	62.829 ^{+0.049} _{-0.049}	141.5 ^{+2.1} _{-2.0}	11.890 ^{+0.079} _{-0.079}	59124 ⁺³⁸ ₋₃₆	(3.331 \pm 0.015) $\times 10^4$	90.9/79
GJ 22	15.44377 ^{+0.0079} _{-0.0079}	509.69 ^{+0.90} _{-0.90}	0.1569 ^{+0.0018} _{-0.0018}	44.27 ^{+0.21} _{-0.21}	104.13 ^{+0.71} _{-0.72}	177.28 ^{+0.23} _{-0.23}	57443.0 ^{+7.5} _{-7.6}	(5.552 \pm 0.031) $\times 10^4$	42.9/43
GJ 54	1.14434 ^{+0.00021} _{-0.00021}	126.14 ^{+0.38} _{-0.38}	0.1712 ^{+0.0023} _{-0.0024}	125.38 ^{+0.35} _{-0.34}	47.06 ^{+0.90} _{-0.91}	91.99 ^{+0.39} _{-0.39}	58123.7 ^{+1.1} _{-1.1}	(1.533 \pm 0.014) $\times 10^3$	44.6/39
GJ 1038	5.63 ^{+1.42} _{-0.90}	135.8 ^{+18.7} _{-7.1}	0.59 ^{+0.16} _{-0.15}	72.1 ^{+2.6} _{-3.2}	180 ⁺¹⁹ ₋₂₂	104.9 ^{+2.6} _{-5.4}	58315 ⁺²⁶⁰⁹ ₋₈₄	(7.9 \pm 1.4) $\times 10^5$	0.8/7
GJ 65	26.368 ^{+0.021} _{-0.021}	2049.4 ^{+3.3} _{-3.3}	0.6204 ^{+0.0021} _{-0.0021}	128.13 ^{+0.15} _{-0.15}	283.350 ^{+0.97} _{-0.96}	146.30 ^{+0.15} _{-0.15}	60596.6 ^{+8.5} _{-8.4}	(1.2380 \pm 0.0060) $\times 10^2$	78.6/97
GJ 84	13.392 ^{+0.028} _{-0.027}	495.2 ^{+1.1} _{-1.1}	0.3863 ^{+0.0073} _{-0.0072}	91.797 ^{+0.058} _{-0.058}	245.30 ^{+0.44} _{-0.43}	102.991 ^{+0.023} _{-0.023}	56688.3 ^{+3.0} _{-2.9}	(6.769 \pm 0.056) $\times 10^4$	26.7/21
2M0213+36	6.441 ^{+0.070} _{-0.073}	161.6 ^{+1.3} _{-1.3}	0.4240 ^{+0.0040} _{-0.0041}	115.37 ^{+0.24} _{-0.24}	207.42 ^{+0.75} _{-0.74}	83.82 ^{+0.33} _{-0.33}	57603.5 ^{+3.0} _{-2.9}	(1.018 \pm 0.016) $\times 10^4$	22.4/11
GJ 98	25.126 ^{+0.030} _{-0.030}	558.01 ^{+0.75} _{-0.75}	0.2327 ^{+0.0013} _{-0.0013}	73.374 ^{+0.048} _{-0.048}	231.89 ^{+0.24} _{-0.24}	109.054 ^{+0.025} _{-0.025}	56423.1 ^{+5.0} _{-5.0}	(2.7523 \pm 0.0097) $\times 10^4$	75.5/87
GJ 99	24.023 ^{+0.089} _{-0.088}	360.54 ^{+0.74} _{-0.72}	0.2084 ^{+0.0028} _{-0.0026}	84.618 ^{+0.051} _{-0.051}	152.9 ^{+2.0} _{-2.0}	98.863 ^{+0.090} _{-0.091}	56345 ⁺⁴⁵ ₋₄₅	(8.121 \pm 0.027) $\times 10^5$	21.3/23
GJ 125	25.67 ^{+0.20} _{-0.19}	534.5 ^{+2.3} _{-2.3}	0.2271 ^{+0.0044} _{-0.0044}	97.186 ^{+0.026} _{-0.026}	181.38 ^{+0.35} _{-0.36}	13.732 ^{+0.082} _{-0.081}	64226 ⁺⁷⁴ ₋₇₃	(2.3173 \pm 0.0098) $\times 10^4$	14.1/23
GJ 190	0.96384 ^{+0.00025} _{-0.00025}	99.14 ^{+0.86} _{-0.86}	0.2439 ^{+0.0094} _{-0.0091}	92.97 ^{+0.25} _{-0.25}	186.5 ^{+5.8} _{-5.8}	40.42 ^{+0.17} _{-0.17}	58182.6 ^{+6.6} _{-6.6}	(1.049 \pm 0.027) $\times 10^3$	33.6/29
GJ 1081	11.622 ^{+0.033} _{-0.033}	279.0 ^{+7.4} _{-6.7}	0.8648 ^{+0.0066} _{-0.0064}	97.06 ^{+0.51} _{-0.50}	231.9 ^{+1.5} _{-1.5}	51.23 ^{+0.25} _{-0.25}	57236 ⁺¹⁷ ₋₁₇	(1.61 \pm 0.12) $\times 10^4$	14.8/19
GJ 234	16.5798 ^{+0.0027} _{-0.0027}	1086.28 ^{+0.26} _{-0.26}	0.38236 ^{+0.00013} _{-0.00013}	52.919 ^{+0.015} _{-0.015}	220.942 ^{+0.020} _{-0.020}	30.384 ^{+0.030} _{-0.030}	63398.76 ^{+0.93} _{-0.93}	(4.6629 \pm 0.0031) $\times 10^3$	114.4/109
GJ 3412	13.5946 ^{+0.0058} _{-0.0058}	440.1 ^{+1.4} _{-1.4}	0.4768 ^{+0.0022} _{-0.0022}	109.80 ^{+0.12} _{-0.12}	58.47 ^{+0.21} _{-0.21}	107.16 ^{+0.18} _{-0.18}	59670.5 ^{+2.8} _{-2.8}	(4.611 \pm 0.047) $\times 10^4$	40.9/51
GJ 3421	3.2857 ^{+0.0011} _{-0.0011}	156.39 ^{+0.25} _{-0.25}	0.2245 ^{+0.0035} _{-0.0034}	131.62 ^{+0.41} _{-0.41}	73.72 ^{+0.36} _{-0.36}	174.19 ^{+0.60} _{-0.62}	57333.4 ^{+3.1} _{-3.1}	(3.543 \pm 0.017) $\times 10^4$	29.3/35
GJ 263	3.6205 ^{+0.0021} _{-0.0021}	143.8 ^{+2.1} _{-2.0}	0.7158 ^{+0.0065} _{-0.0064}	103.28 ^{+0.36} _{-0.36}	287.52 ^{+0.51} _{-0.51}	81.04 ^{+0.24} _{-0.24}	57093.6 ^{+3.4} _{-3.3}	(2.268 \pm 0.099) $\times 10^4$	21.7/17
GJ 277	53.0 ^{+9.2} _{-7.2}	1058 ⁺¹³ ₋₈₄	0.48 ^{+0.14} _{-0.12}	93.53 ^{+0.48} _{-0.34}	22 ⁺³³² ₋₁₇	10.22 ^{+0.26} _{-0.44}	71033 ⁺¹²⁰³² ₋₃₃₉₇	(4.22 \pm 0.16) $\times 10^4$	18.4/13
GJ 3454	23.767 ^{+0.045} _{-0.045}	632.90 ^{+0.96} _{-0.95}	0.58648 ^{+0.00061} _{-0.00062}	11.7 ^{+1.1} _{-1.2}	66.8 ^{+5.8} _{-5.5}	77.3 ^{+5.2} _{-5.4}	57467.0 ^{+2.6} _{-2.6}	(4.487 \pm 0.019) $\times 10^4$	14.7/19
GJ 330	32.69 ^{+0.42} _{-0.40}	582 ⁺¹⁴ ₋₁₂	0.8301 ^{+0.0071} _{-0.0070}	105.78 ^{+0.51} _{-0.49}	167.4 ^{+1.1} _{-1.1}	142.0 ^{+1.1} _{-1.1}	73905 ⁺⁶⁷⁵ ₋₆₃₀	(1.737 \pm 0.049) $\times 10^4$	22.5/13
LHS 6167	5.0393 ^{+0.0034} _{-0.0035}	198.85 ^{+0.78} _{-0.77}	0.4810 ^{+0.0034} _{-0.0034}	115.70 ^{+0.19} _{-0.19}	92.67 ^{+0.23} _{-0.24}	112.75 ^{+0.32} _{-0.32}	56728.4 ^{+2.7} _{-2.7}	(3.096 \pm 0.033) $\times 10^4$	27.7/27
GJ 340	34.23 ^{+0.13} _{-0.13}	676.2 ^{+1.2} _{-1.3}	0.3100 ^{+0.0035} _{-0.0035}	77.02 ^{+0.30} _{-0.31}	312.05 ^{+0.79} _{-0.78}	25.23 ^{+0.25} _{-0.25}	69557 ⁺⁵⁴ ₋₅₃	(2.638 \pm 0.026) $\times 10^4$	77.1/67
GJ 352	18.480 ^{+0.026} _{-0.026}	633.7 ^{+2.6} _{-2.5}	0.3322 ^{+0.0026} _{-0.0026}	143.07 ^{+0.72} _{-0.70}	288.37 ^{+0.77} _{-0.75}	51.57 ^{+0.45} _{-0.46}	59094 ⁺²³ ₋₂₃	(7.45 \pm 0.11) $\times 10^4$	24.0/15
GJ 381	7.5711 ^{+0.0057} _{-0.0058}	294.4 ^{+3.9} _{-3.5}	0.7528 ^{+0.0069} _{-0.0069}	92.996 ^{+0.079} _{-0.082}	273.95 ^{+0.12} _{-0.13}	68.546 ^{+0.052} _{-0.051}	57698.9 ^{+4.3} _{-4.5}	(4.45 \pm 0.17) $\times 10^4$	33.8/33
GJ 416	7.2716 ^{+0.0077} _{-0.0078}	184.46 ^{+0.66} _{-0.59}	0.4571 ^{+0.0037} _{-0.0037}	87.25 ^{+0.24} _{-0.24}	154.3 ^{+1.1} _{-1.2}	89.08 ^{+0.11} _{-0.11}	58731 ⁺¹¹ ₋₁₁	(1.187 \pm 0.013) $\times 10^4$	34.4/23
GJ 469	11.5549 ^{+0.0051} _{-0.0051}	312.72 ^{+0.62} _{-0.62}	0.2992 ^{+0.0030} _{-0.0030}	108.19 ^{+0.064} _{-0.064}	268.62 ^{+0.12} _{-0.12}	9.82 ^{+0.12} _{-0.12}	58767.2 ^{+3.1} _{-3.1}	(2.291 \pm 0.013) $\times 10^4$	33.4/37

Table 4 *continued*

Table 4 (continued)

Name	P (years)	a'' (mas)	e	i (degrees)	ω (degrees)	Ω (degrees)	T_0 MJD	a''/P arcsec 3 yr $^{-2}$	χ^2/dof
4/37									
Gl 473	15.851 $^{+0.017}_{-0.017}$	919.9 $^{+1.1}_{-1.1}$	0.2976 $^{+0.0010}_{-0.0010}$	103.05 $^{+0.12}_{-0.12}$	349.88 $^{+0.65}_{-0.65}$	143.12 $^{+0.18}_{-0.18}$	60340 $^{+10}_{-10}$	(3.098 ± 0.012) $\times 10^3$	50.0/49
Gl 494	13.713 $^{+0.033}_{-0.033}$	428.09 $^{+0.40}_{-0.41}$	0.24260 $^{+0.00083}_{-0.00083}$	130.66 $^{+0.19}_{-0.19}$	158.70 $^{+0.57}_{-0.57}$	56.20 $^{+0.16}_{-0.16}$	59362 $^{+17}_{-17}$	(4.172 ± 0.028) $\times 10^4$	33.1/23
Gl 570	0.84567 $^{+0.00035}_{-0.00035}$	144.1 $^{+3.1}_{-2.7}$	0.752 $^{+0.015}_{-0.014}$	107.43 $^{+0.70}_{-0.69}$	310.5 $^{+1.8}_{-1.8}$	16.30 $^{+0.72}_{-0.74}$	58304.6 $^{+1.5}_{-1.6}$	(4.18 ± 0.25) $\times 10^3$	26.1/37
Gl 600	2.7808 $^{+0.0012}_{-0.0012}$	100.91 $^{+0.58}_{-0.57}$	0.3396 $^{+0.0040}_{-0.0039}$	34.49 $^{+0.83}_{-0.85}$	151.7 $^{+1.4}_{-1.4}$	115.8 $^{+1.3}_{-1.2}$	57927.9 $^{+2.8}_{-2.9}$	(1.329 ± 0.023) $\times 10^4$	18.2/27
Gl 623	3.7373 $^{+0.0019}_{-0.0019}$	237.85 $^{+0.46}_{-0.46}$	0.6259 $^{+0.0019}_{-0.0019}$	153.44 $^{+0.39}_{-0.39}$	247.98 $^{+0.64}_{-0.64}$	98.83 $^{+0.74}_{-0.74}$	58139.5 $^{+2.2}_{-2.2}$	(9.634 ± 0.049) $\times 10^4$	28.0/41
GJ 1210	14.298 $^{+0.015}_{-0.015}$	307.70 $^{+0.24}_{-0.23}$	0.48392 $^{+0.00032}_{-0.00032}$	112.351 $^{+0.046}_{-0.045}$	23.03 $^{+0.19}_{-0.19}$	60.598 $^{+0.070}_{-0.069}$	59161.7 $^{+5.8}_{-5.7}$	(1.4251 ± 0.0034) $\times 10^4$	12.0/19
Gl 660	34.537 $^{+0.082}_{-0.081}$	765.1 $^{+1.5}_{-1.4}$	0.1990 $^{+0.0054}_{-0.0054}$	18.82 $^{+0.69}_{-0.68}$	218.1 $^{+4.8}_{-5.1}$	144.1 $^{+6.0}_{-5.7}$	59796 $^{+50}_{-48}$	(3.755 ± 0.026) $\times 10^4$	9.6/9
Gl 661	12.9586 $^{+0.0058}_{-0.0059}$	776.6 $^{+2.2}_{-2.2}$	0.7508 $^{+0.0029}_{-0.0029}$	146.63 $^{+0.36}_{-0.36}$	98.3 $^{+1.0}_{-1.0}$	159.3 $^{+1.2}_{-1.2}$	57731.3 $^{+2.5}_{-2.5}$	(2.789 ± 0.025) $\times 10^3$	44.9/67
GJ 4024	20.26 $^{+0.34}_{-0.30}$	361.9 $^{+5.0}_{-4.8}$	0.533 $^{+0.013}_{-0.013}$	104.70 $^{+0.28}_{-0.27}$	232.9 $^{+1.5}_{-1.5}$	129.06 $^{+0.33}_{-0.32}$	61648 $^{+119}_{-107}$	(1.152 ± 0.026) $\times 10^4$	3.0/9
Gl 695	43.23 $^{+0.28}_{-0.27}$	1414 $^{+10}_{-10}$	0.1806 $^{+0.0039}_{-0.0038}$	66.08 $^{+0.20}_{-0.20}$	172.05 $^{+0.54}_{-0.52}$	60.93 $^{+0.84}_{-0.83}$	54586 $^{+15}_{-15}$	(1.513 ± 0.039) $\times 10^3$	4.5/21
Gl 747	5.75030 $^{+0.00079}_{-0.00079}$	296.11 $^{+0.68}_{-0.68}$	0.2573 $^{+0.0011}_{-0.0010}$	77.623 $^{+0.63}_{-0.63}$	330.30 $^{+0.72}_{-0.72}$	84.639 $^{+0.069}_{-0.068}$	58827.9 $^{+4.4}_{-4.4}$	(7.852 ± 0.054) $\times 10^4$	86.7/75
Gl 748	2.47626 $^{+0.00028}_{-0.00029}$	146.50 $^{+0.46}_{-0.46}$	0.4559 $^{+0.0017}_{-0.0017}$	131.05 $^{+0.38}_{-0.37}$	23.88 $^{+0.59}_{-0.60}$	176.71 $^{+0.36}_{-0.36}$	58172.0 $^{+3.1}_{-1.00}$	(5.128 ± 0.049) $\times 10^4$	86.8/71
Gl 762.1	1.35257 $^{+0.00046}_{-0.00046}$	81.14 $^{+0.98}_{-0.97}$	0.4037 $^{+0.0075}_{-0.0073}$	148.6 $^{+2.3}_{-2.1}$	2.5 $^{+3.3}_{-3.6}$	68.2 $^{+2.8}_{-3.1}$	58028.6 $^{+490.3}_{-3.3}$	(2.92 ± 0.11) $\times 10^4$	33.0/59
Gl 765.2	11.914 $^{+0.026}_{-0.026}$	193.2 $^{+1.1}_{-1.1}$	0.2419 $^{+0.0088}_{-0.0088}$	80.64 $^{+0.27}_{-0.27}$	70.33 $^{+0.75}_{-0.79}$	112.92 $^{+0.42}_{-0.42}$	57753 $^{+16}_{-15}$	(5.076 ± 0.095) $\times 10^5$	25.4/33
GJ 1245	16.888 $^{+0.010}_{-0.010}$	830.27 $^{+0.25}_{-0.24}$	0.34160 $^{+0.00063}_{-0.00064}$	135.44 $^{+0.12}_{-0.11}$	216.87 $^{+0.22}_{-0.22}$	80.48 $^{+0.15}_{-0.15}$	57695.5 $^{+1.2}_{-1.2}$	(2.0067 ± 0.0034) $\times 10^3$	73.1/67
Gl 791.2	1.47118 $^{+0.00039}_{-0.00042}$	97.2 $^{+3.2}_{-3.2}$	0.6302 $^{+0.0084}_{-0.0084}$	163.0 $^{+9.0}_{-11.1}$	87 $^{+136}_{-54}$	272 $^{+34}_{-153}$	57996 $^{+11}_{-528}$	(4.24 ± 0.33) $\times 10^4$	53.5/37
Gl 804	14.709 $^{+0.018}_{-0.018}$	284.1 $^{+2.3}_{-2.3}$	0.6012 $^{+0.0055}_{-0.0054}$	129.51 $^{+0.53}_{-0.55}$	246.76 $^{+0.28}_{-0.27}$	79.3 $^{+1.0}_{-1.0}$	58541.8 $^{+9.4}_{-9.3}$	(1.060 ± 0.026) $\times 10^4$	35.0/27
Gl 831	1.93195 $^{+0.00013}_{-0.00013}$	145.39 $^{+0.16}_{-0.16}$	0.38947 $^{+0.00090}_{-0.00090}$	49.61 $^{+0.15}_{-0.15}$	190.05 $^{+0.42}_{-0.42}$	144.28 $^{+0.21}_{-0.21}$	58217.33 $^{+0.64}_{-0.65}$	(8.234 ± 0.028) $\times 10^4$	81.9/79
Gl 844	11.812 $^{+0.045}_{-0.044}$	306.7 $^{+2.0}_{-2.0}$	0.4850 $^{+0.0052}_{-0.0052}$	38.10 $^{+0.78}_{-0.81}$	267.31 $^{+0.68}_{-0.77}$	151.53 $^{+0.76}_{-0.77}$	57031.7 $^{+8.0}_{-8.1}$	(2.067 ± 0.043) $\times 10^4$	4.5/3
HD 239960	45.35 $^{+0.29}_{-0.29}$	2453 $^{+10}_{-10}$	0.4147 $^{+0.0021}_{-0.0020}$	165.63 $^{+0.51}_{-0.51}$	209.2 $^{+2.4}_{-2.5}$	153.5 $^{+2.7}_{-2.9}$	56946.3 $^{+7.9}_{-7.9}$	(7.187 ± 0.031) $\times 10^3$	50.3/49
GJ 4287	17.237 $^{+0.018}_{-0.018}$	336.4 $^{+1.3}_{-1.3}$	0.2381 $^{+0.0033}_{-0.0033}$	55.37 $^{+0.29}_{-0.29}$	116.65 $^{+0.76}_{-0.75}$	69.59 $^{+0.20}_{-0.19}$	61003 $^{+22}_{-22}$	(1.281 ± 0.015) $\times 10^4$	12.2/37
Gl 893.4	19.165 $^{+0.018}_{-0.018}$	220.10 $^{+0.52}_{-0.52}$	0.4400 $^{+0.0034}_{-0.0034}$	116.63 $^{+0.18}_{-0.18}$	322.35 $^{+0.63}_{-0.62}$	28.97 $^{+0.23}_{-0.23}$	58451.5 $^{+9.1}_{-9.0}$	(2.903 ± 0.017) $\times 10^5$	38.8/23
Gl 900	36.0 $^{+1.5}_{-1.3}$	446.2 $^{+11.5}_{-9.7}$	0.130 $^{+0.023}_{-0.021}$	82.36 $^{+0.20}_{-0.20}$	112.5 $^{+6.9}_{-7.8}$	8.19 $^{+0.26}_{-0.27}$	54581 $^{+200}_{-220}$	(6.84 ± 0.12) $\times 10^5$	26.3/23
Gl 913	2.3912 $^{+0.0012}_{-0.0012}$	116.95 $^{+0.28}_{-0.27}$	0.5143 $^{+0.0020}_{-0.0020}$	114.19 $^{+0.20}_{-0.20}$	306.62 $^{+0.24}_{-0.24}$	112.29 $^{+0.23}_{-0.23}$	58412.86 $^{+0.94}_{-0.94}$	(2.798 ± 0.019) $\times 10^4$	3.6/5

APPENDIX

A. CONVERTING OBSERVED ΔK_X TO 2MASS ΔK_S FOR M DWARFS

To place all K -band magnitudes on the 2MASS system, we derived a relation between ΔK_X and ΔK_S as a function of ΔK_X , where X denotes the particular filter (e.g., K_{cont} , K') used for the AO observations. For photometry, we only used observations taken with a filter somewhere in the K -band (all wavelengths are used for astrometry), which included observations with the narrow Bracket-Gamma filter.

To derive a conversion between contrasts, we used the 183 absolutely-flux calibrated spectra of nearby single stars from Mann et al. (2015), which cover a similar range of T_{eff} and M_* as the sample considered here. These spectra are mostly empirical; models are only used to fill in gaps in the spectrum or regions of high telluric contamination, none of which land in the regions covered by the filters considered here.

First we randomly sampled two stars from the sample and scaled the absolute level of each spectrum by the star's distance (effectively placing both at 1 pc). We convolved each of the two stars with the relevant filter profiles for NIRC2⁸, KIR⁹, NIRI¹⁰, and NaCo¹¹, and integrate over the wavelength range of the filters to compute the flux (F) in a given band. We used a filter profile for 2MASS K_S from Cohen et al. (2003). The ΔK_X value for the given pair was then computed as $2.5 \log_{10}(F_1/F_2)$.

We repeated this process with 5000 unique combinations of the 183 stars for 12 different filter/instrument combinations. For each filter and instrument combination we computed a best-fit line to $\Delta K_S - \Delta K_X$ as a function of ΔK_X . We show four examples in Figure 17. For the majority of the filters considered, the trend is insignificant compared to errors in the underlying spectra and absolute calibration (1-2%). We did not apply a correction in these cases. Most of the scatter seen in Figure 17 is due to random errors in the input calibrated spectra and distance. K_{cont} , for example, shows a larger apparent scatter in Figure 17, primarily because the narrow band is more sensitive to random Poisson errors in the calibrated spectra, but the final precision on the calibration is smaller. The uncertainties on applied corrections were 0.01-0.02 mag for all filters, which was driven primarily by potential systematic errors in the underlying spectra.

We did not see a significant difference in any derived correction based on the metallicity of the component stars, as expected based on how [Fe/H] changes K -band flux levels (Figure 4). Thus we did not attempt to include [Fe/H] in these relations. We also found no significant effect as a function of the mass of the primary. However, this was difficult to test due to limitations of the input sample. The Mann et al. (2015) spectral sample covers K7 to M7, but is poorly populated on the extreme ends. While we can make a wide range of combinations of low-contrast systems (M0+M0 to M6+M6), we have limited options for high-contrast (where primary can only be \sim K7-M1) systems where temperature effects would be most clear.

⁸ NIRC2 Filters

⁹ KIR Filters

¹⁰ NIRI Filters

¹¹ NACO Filters

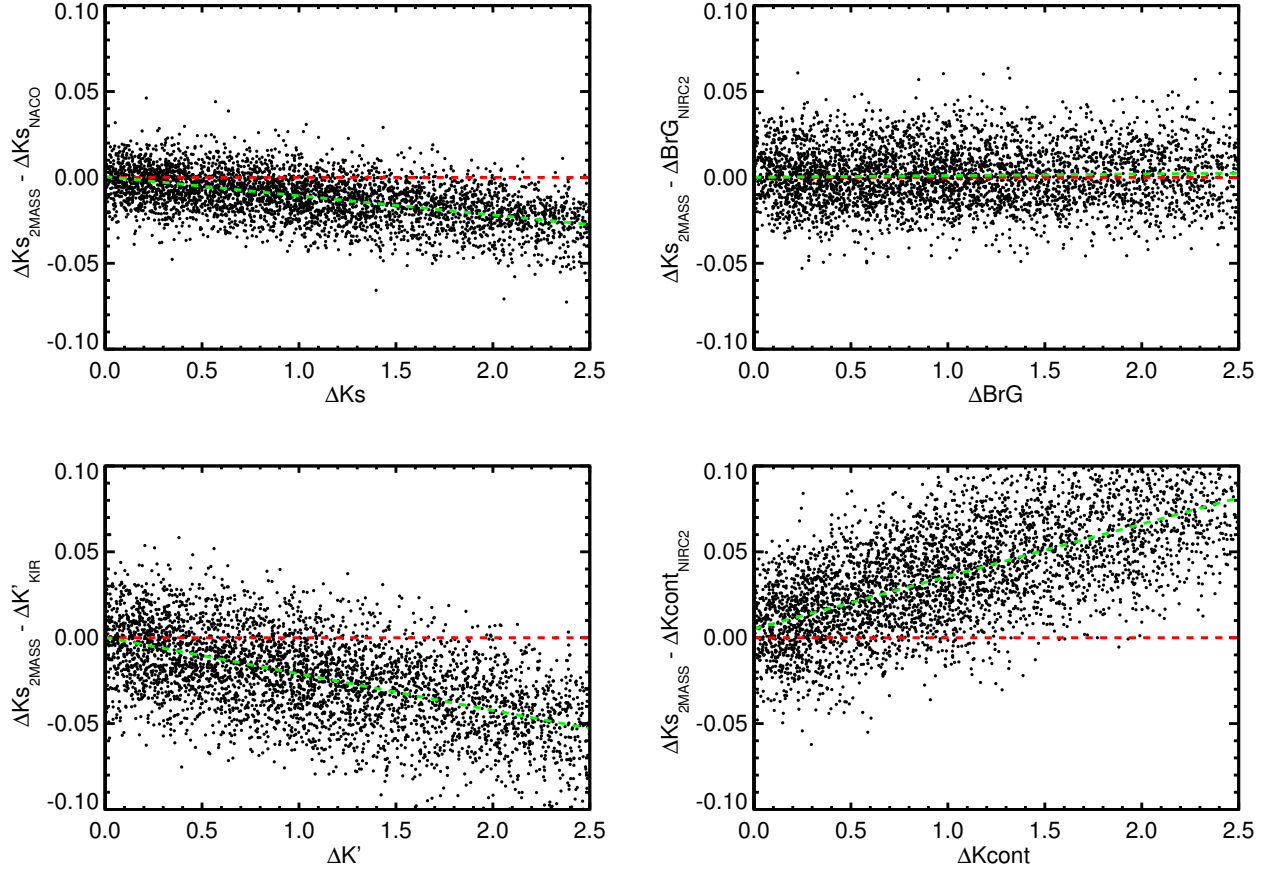


Figure 17. Difference between 2MASS ΔK_s and four example Δm values measured from our AO imaging, built from a grid of absolutely-calibrated spectra and the filter profiles provided for each filter. No corrections are applied for the NIRC2 Bracket-Gamma (BrG) and K_s (K-short) filter, as the trend is not significant compared to potential systematic issues in the calibration of the underlying spectra.

B. ORBITS OF BINARIES

Here we show diagnostic plots of each of the binaries in our sample. Details of the input points data can be found in Section 3.2 for data analyzed in this paper and in Section 4.1 for astrometry from the literature. The orbital fitting method is described in Section 5.

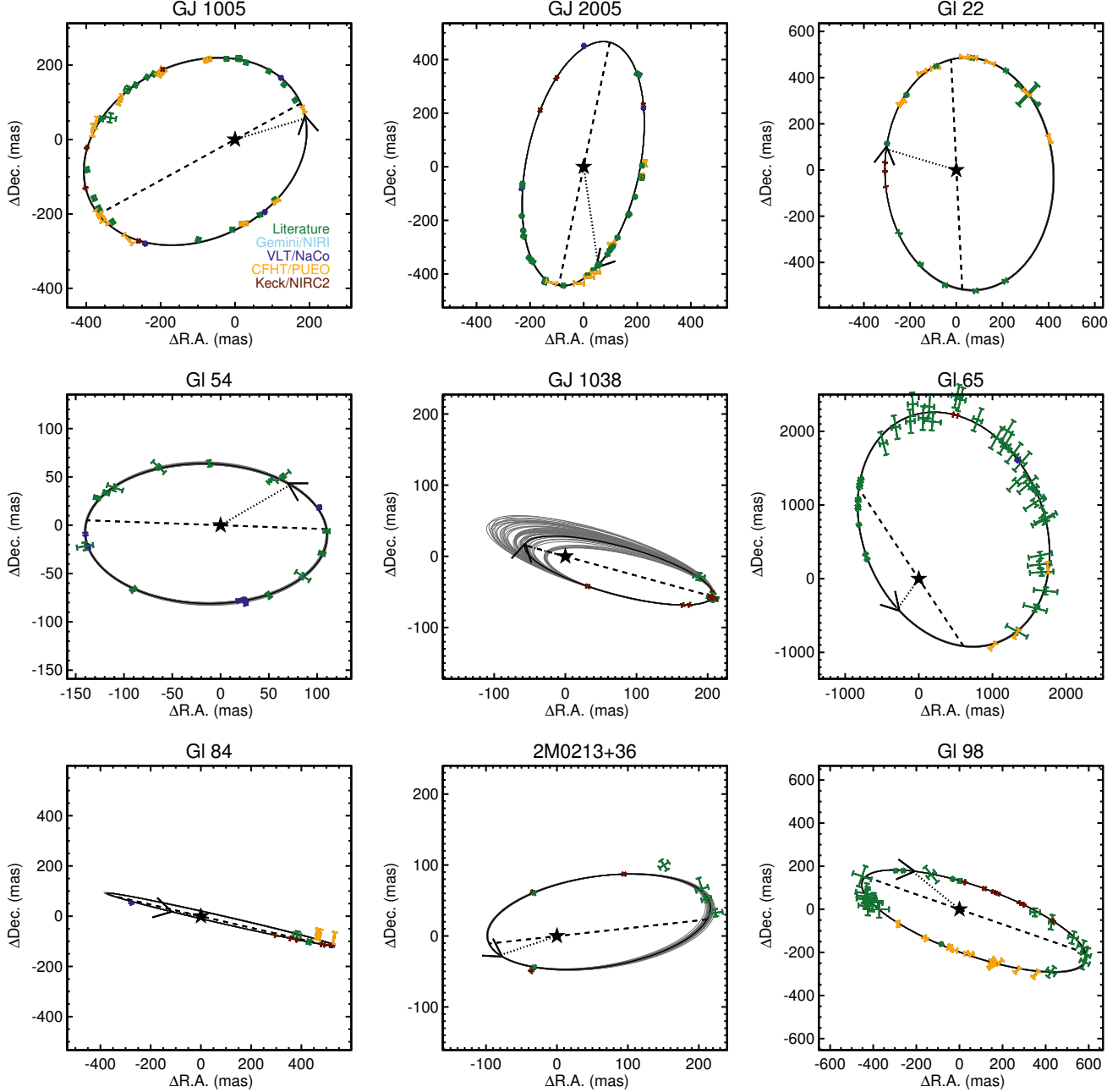


Figure 18. Orbital fit for each binary fit in this paper. The black star marks the primary (always at 0, 0). The best-fit (highest likelihood) is shown as a black line, with 50 randomly selected orbit fits from the MCMC shown in grey to provide an estimate of the uncertainties. In some fits, the range of orbital solutions is so small that the grey lines are not visible underneath the best-fit black line. Points are individual separation and position angle measurements with adopted uncertainties, color-coded by the data source (Gemini/NIRI in light blue, VLT/NaCo in blue, CFHT/PUEO in light red, Keck/NIRC2 in dark red, and literature data in green). The dashed line is the line of nodes, the dotted line indicates periastron passage, and the arrow marks the direction of motion.

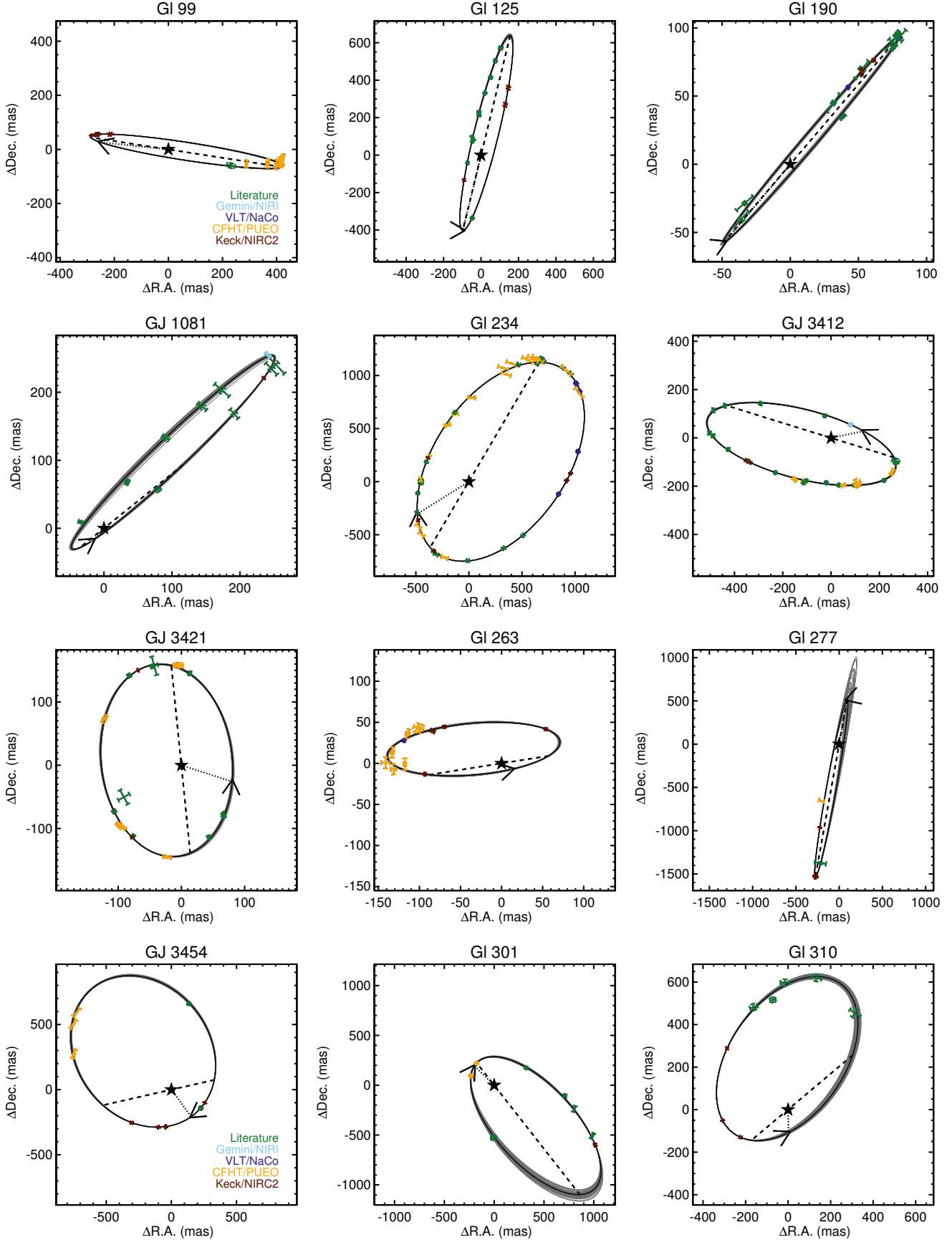


Figure 19. Figure 18 continued.

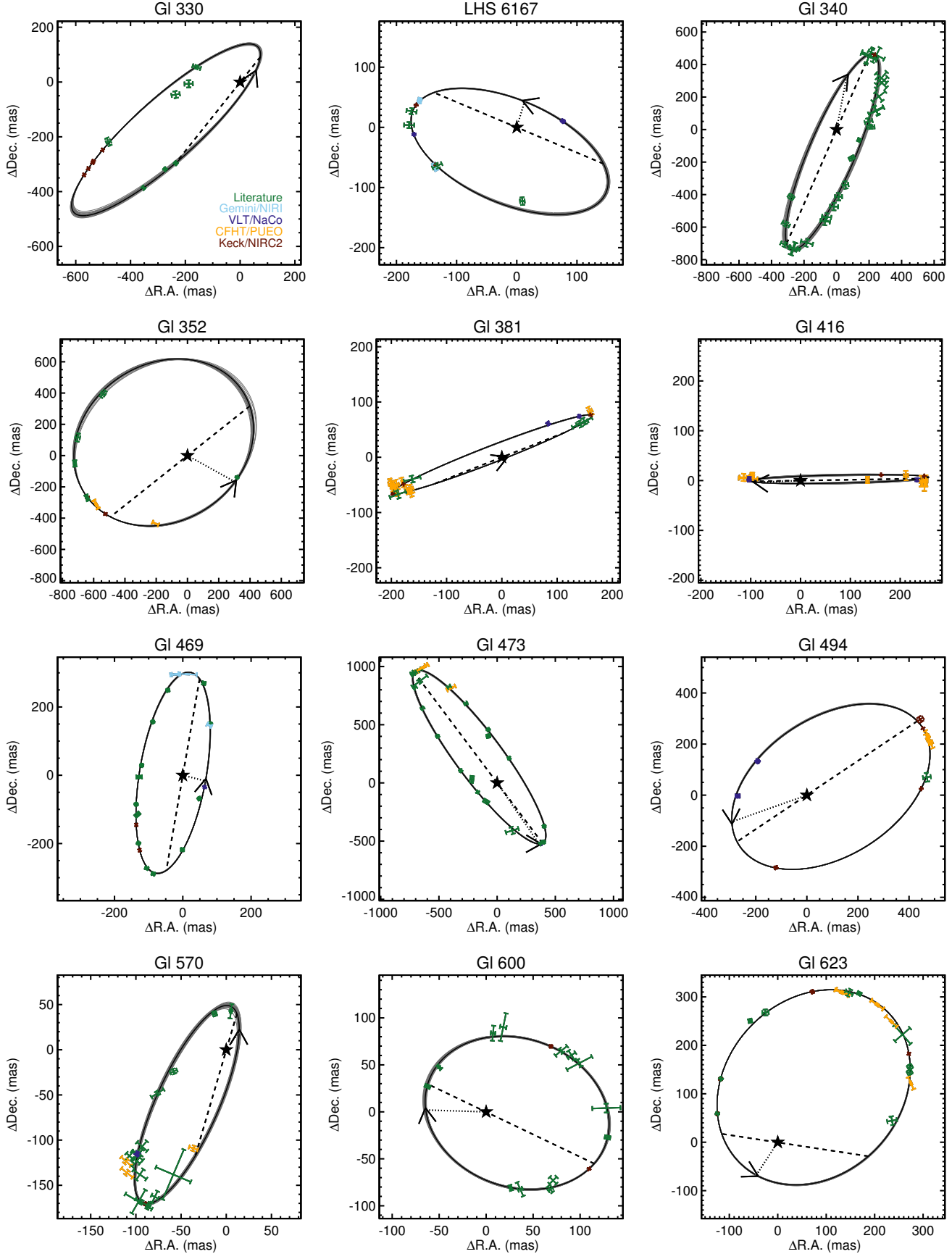


Figure 20. Figure 18 continued.

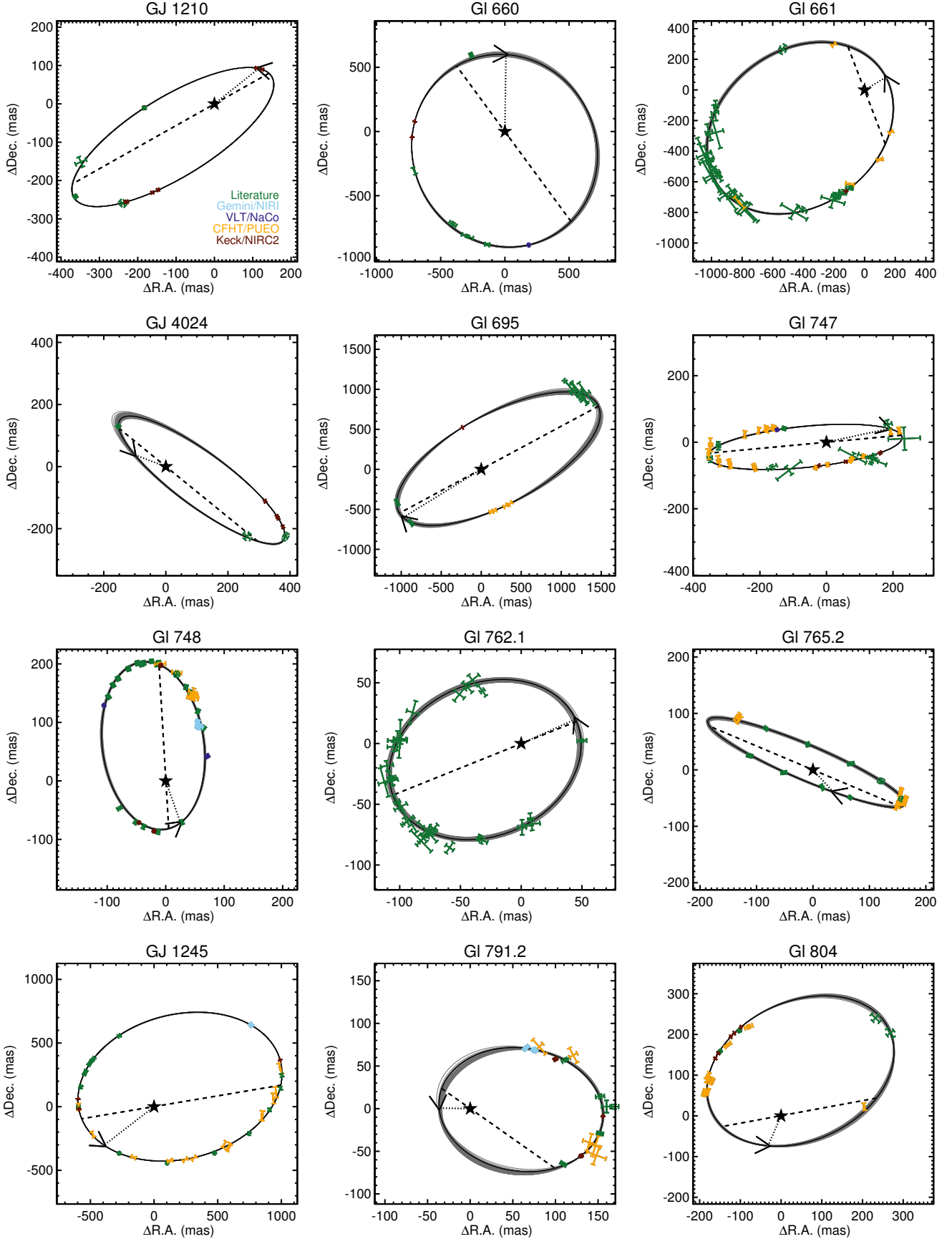


Figure 21. Figure 18 continued.

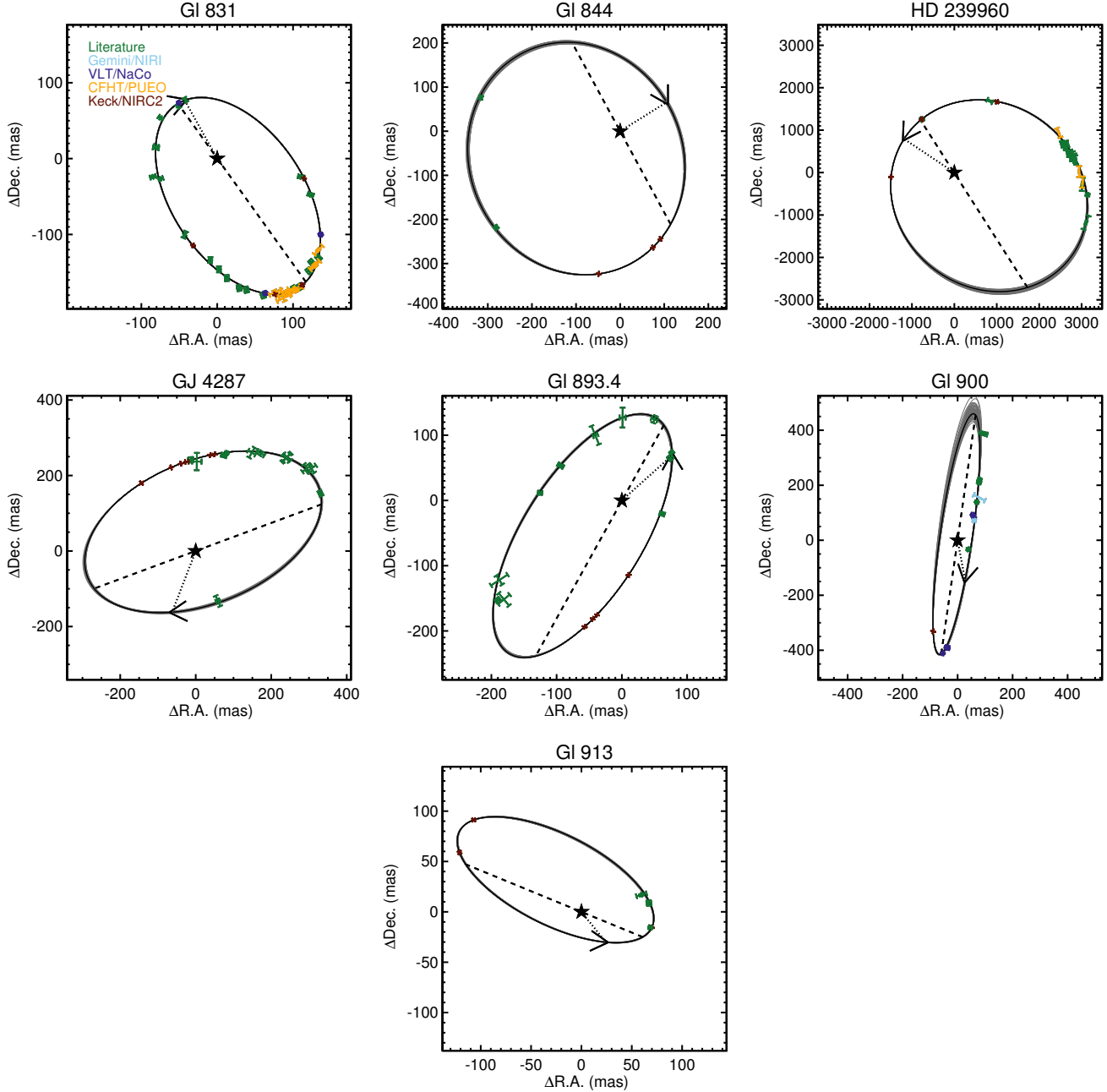


Figure 22. Figure 18 continued.

Table 5. Input Astrometry and Photometry

UT Date ^a (YYYY-MM-DD)	ρ (mas)	θ (degrees)	Filter	Δm ^b (mag)	Source ^c	PI ^d
Gl 84						
2002-07-23	390 ± 15	101.0 ± 2.1	Beuzit et al. (2004)	
2002-10-02	443.0 ± 6.5	103.4 ± 1.1	Dieterich et al. (2012)	
2003-12-09	536.1 ± 2.7	102.48 ± 0.42	FeII	3.633 ± 0.045	VLT/NaCo	Beuzit
2004-09-28	536.7 ± 1.7	99.3 ± 2.5	H2v=2-1	3.98 ± 0.10	CFHT/PUEO	Catala
2005-10-13	478.5 ± 4.3	98.9 ± 2.6	H2v=2-1	4.41 ± 0.17	CFHT/PUEO	CFHTTeam
2005-10-14	468.8 ± 4.9	98.6 ± 2.5	FeII	4.47 ± 0.34	CFHT/PUEO	CFHTTeam
2013-07-03	282.3 ± 1.2	280.78 ± 0.41	IB2.18	3.310 ± 0.031	VLT/NaCo	De Rosa
2015-06-23	306.06 ± 0.22	104.376 ± 0.046	K _{cont}	3.363 ± 0.012	Keck/NIRC2	Ireland
2015-10-01	366.89 ± 0.51	103.890 ± 0.043	K _{cont}	3.329 ± 0.028	Keck/NIRC2	Mann
2015-11-18	393.21 ± 0.21	103.779 ± 0.050	K _{cont}	3.343 ± 0.011	Keck/NIRC2	Gaidos
2016-08-02	492.48 ± 0.24	103.084 ± 0.028	K _{cont}	3.308 ± 0.011	Keck/NIRC2	Gaidos
2016-09-20	505.35 ± 0.30	102.984 ± 0.030	K _{cont}	3.372 ± 0.030	Keck/NIRC2	Mann
2017-01-25	528.70 ± 0.75	102.653 ± 0.092	K _{cont}	3.360 ± 0.094	Keck/NIRC2	Gaidos

NOTE—Table 5 is published in its entirety in the electronic edition of the Publications of the AAS. A portion is shown here for guidance regarding its form and content.

^aDates from literature points may be off by 1 day due to inconsistency in reporting UT versus local date.

^bErrors on Δm values are based on the scatter in individual images, and are likely underestimated.

^cAstrometry with source as Keck/NIRC2, CFHT/PUEO, VLT/NaCo, or Gemini/NIRI are from this paper. All other measurements list the paper reference.

^dPrincipal investigator for AO data analyzed in this paper (from our program or the archive) as it was listed in the image header.